NORTHWESTERN UNIVERSITY

Nuclear magnetic resonance studies of under-doped $HgBa_2CuO_{4+\delta}$ single crystals

A DISSERTATION

SUBMITTED TO THE GRADUATE SCHOOL

IN PARTIAL FULFILLMENT OF THE REQUIREMENTS

for the degree

DOCTOR OF PHILOSOPHY

Field of Physics

By

Ingrid Stolt

EVANSTON, ILLINOIS

December 2021

ABSTRACT

Nuclear magnetic resonance studies of under-doped $HgBa_2CuO_{4+\delta}$ single crystals

Ingrid Stolt

The cuprate superconductor $HgBa_2CuO_{4+\delta}$ (Hg1201) has one of the simplest physical structures of the cuprates making it an ideal candidate for nuclear magnetic resonance (NMR) measurements. Here we discuss our NMR experiments aimed at studying the mixed state of two under-doped single crystal Hg1201 samples at high magnetic fields.

Acknowledgements

I would like to begin by thanking the people who helped me the most directly in becoming a physicist. Firstly, I must thank my high school physics teacher, Mr. Nicholson[1] for introducing me to the subject as well as introducing me to the quirky personalities of physicists. I also extend my gratitude to my chemistry teacher, Mr. D'Amico for introducing me to non-biological science, showing me that organic chemistry is not as scary as its reputation makes it out to be and, perhaps most importantly, introducing me to NMR.

I feel very fortunate to have attended Bard college while Professor Matthew Deady was the chair of the physics department. Thank you, Matt, for encouraging me to begin pursuing physics even though I started later than most. I am also very lucky to have begun my journey as a physicist at the same time that Professor Paul Cadden-Zimansky started teaching in the Bard physics department. Thank you, Paul, for being tough but fair and showing me the most fun parts of physics in *Modern Physics*, *Math Methods I* and beyond. I am grateful to have overlapped with Professors Hal Haggard and Nick Lanzillo. Hal, your intense thermodynamics/statistical mechanics assignments made grad school a lot less of a shock for me than it seemed to be for my peers and when I asked you to help edit my undergrad thesis your read through all 149 pages of it with a fine-toothed comb. That was really above and beyond and I will forever be appreciative of that gesture

[1]Who's name I have probably misspelled.

alone, in addition to many others. Nick, you helped me put together an undergraduate thesis that I still boast about and introduced me to programming in your *Computational Physics* class. Thank you for saving me from thee embarrassment of never having coded on arriving at NU.

Thank you to the Bard chemistry department faculty, in particular Professor Emily McLaughlin, for being an amazing adviser and boss. Emily, you showed me that it is possible to be loved by everyone while giving tough assignments and expecting the most of your students. I also extend my thanks to Professor Chis LaFratta for encouraging me to pursue physics and for being an enthusiastic professor. Chris, I remember when you asked my P-Chem class what it means to say that two operators do not commute and when no one answered you said, "It means that, these operators... work from home." That still cracks me up. Don't let anyone tell you it's not hilarious. Lastly at Bard I would like to thank Professor David Shein for failing at convincing me to doubt the science I studied (and instead convincing me to double major in chemistry and physics) through his *Introduction to Philosophy of Science* course. I would also like to thank Professor Christian Bracher for his hilarious and informative instruction of my first undergraduate physics course. Christian, I will forever associate the right-hand-rule with making my right hand into an antenna and putting it on top of my head.

Upon coming to Northwestern in the summer of 2015 I was taken under the wing of, now Doctor, Sam Davis. Sam, thank you for sacrificing so many hours to teaching me about microwave electronics, helping me solder and showing me how too use the SEM and

wire-bonder, although I never really became proficient in either. Thank you to Professor Chandrasekhar for serving on my committee and for taking a chance on me as a graduate student by accepting me into the school (I assume, I don't really know the details of my acceptance) and allowing me to work in your lab. Continuing with this timeline, I am very grateful to have been able to take Professor Jim Sauls' graduate *Quantum Mechanics II* & *III* courses. Quantum mechanics has never made so much sense. Thank you to Professor Sauls for being a phenomenal instructor and for serving on my committee.

I extend my deep appreciation to the people who have helped me with the experimental side of my research. Yizhou Xin and Andrew Zimmerman, you both have been so patient with me and willing to come in to tech on Sunday afternoon when I call in a panic about a problem with the probe/ magnet. I wish you both the best of luck with your academic or non-academic careers. To Peter Lee, thank you for helping pass the torch of the Hg1201 project on to me and teaching me how to set up an NMR experiment as well as the ^{17}O exchange and annealing procedure. Thank you as well to Andy Mounce for all of your helpful email exchanges and clearly named data files.

Lastly at NU I thank Professor Bill Halperin. Bill, you have been an excellent adviser and I feel so lucky to have been your student. Thank you for serving on my committee, for helping me with my thesis and for all your help with mechanical work in the lab. On the non-academic side of things I greatly enjoyed our talks about cycling and I hope you get at least one day of riding with minimal wind before the temperature drops again.

On that note, I would also like to thank Liam and Heather for taking me to amazing places and helping me escape the stress of grad school for several hours a week.

Lastly, and perhaps most importantly, thank you to my family. Tack mamma och/og takk pappa for supporting me both financially and emotionally during the bulk of my education. I am so fortunate to have grown up with such mature, supportive, non-judgmental, relaxed, yet responsible role models. I also extend my thanks to my brother, Peter, without whom I would be an only child. Peter, thank you for being such a kindhearted person and for serving as an outlet for our parents' doting when I left for college. Thank you to my grandparents and extended family as well for all of your enthusiasm from across the Atlantic.

Finally, thank you to Sötnos and Sapphire for being extremely helpful kitties. I could never have done all this without the two of you lying on top of my textbooks and laptops and meowing for cuddles while I tried to study for the GREs, do homework, analyze data and write my thesis when I visited New York.

Table of Contents

List of Figures

List of Tables

CHAPTER 1

Introduction

Superconductivity was first discovered in 1911 by the Dutch physicist, Kamerlingh Onnes [16]. Onnes was testing the resistivity of elemental mercury at cryogenic temperatures and found that the resistivity consistently vanished below a certain temperature. This property of current flow with zero resistance is now known as the defining electronic characteristic of superconductivity. After Onnes' initial discovery many elemental metals were also found to exhibit this transition to a zero resistance state at low temperature, T ($T \sim 1$ K). The temperature at which the resistance disappeared became known as the *critical temperature*, T_c, which is the temperature below which a system is superconducting.

About 20 years after Onnes' discovery physicists Meissner and Ochsenfeld discovered a second characteristic property of superconducting materials, perfect diamagnetism [17]. The two found that, in addition to having zero electrical resistance superconductors (SCs) will also expel magnetic fields from their bulk such that the bulk magnetization is exactly opposite to the applied field. This causes the induction, B, in the bulk of the material go to zero. This is now commonly known as the *Meissner effect* or (less commonly) the *Meissner-Ochsenfeld effect*.

Early theories of superconductivity soon followed with the London brothers [18] developing a theory centred on minimizing an electromagnetic free energy of the superconducting charge carriers. Ginzburg and Landau [19] later produced a theory in which the superconducting transition was characterized by the appearance of a complex order parameter, ψ, which describes the superconducting current. Abrikosov [20, 21] used the Ginzburg-Landau (GL) theory to predict the existence of a second class of SCs that should exhibit only a partial Meissner state for certain applied fields. Specifically, this state would allow an external field to penetrate the bulk of the SC in fixed areas each carrying one quantum of magnetic flux. These regions of penetrating flux were called "vortices" and Abrikosov showed that at low enough temperatures the vortices would arrange in a periodically ordered structure known as the "vortex lattice."

Around the same time physicists Bardeen, Cooper and Schrieffer published their now-famous BCS theory which describes the mechanism of superconductivity in terms of a macroscopic ground state of superconducting carriers, so-called "Cooper pairs." These pairs consist of electrons of opposite spin forming a spin-singlet state which acts as a boson allowing multiple Cooper pairs to exist in the same ground state. This results in an opening of an energy gap at the Fermi surface between the Fermi energy, E_F, and the new, lower energy BCS ground state. The gap energy, Δ_{BCS}, is isotropic and can be observed experimentally, e.g. by a "coherence peak" in the nuclear relaxation rate below a certain temperature [22].

The BCS theory was remarkably successful in explaining superconductivity in elemental metals. However, a new class of superconductors was later discovered whose behaviors could not be described by the BCS theory. This new class of materials became known as the *cuprates* and they were the first known examples of *high-temperature* or *high-T_c* superconductors, so called because their recorded T_c's were very large compared to the elemental SCs. The first cuprate superconductor, $La_{2-x}Ba_xCuO_{4-y}$ (LBCO), was discovered in 1986 [23] with a reported T_c of 35 K, the highest critical tempereature to be reported at the time. Several months later, Cava *et al.* [24] discovered that the same compound could be superconducting if the Ba was replaced with Sr. The resulting compound, $La_{2-x}Sr_xCuO_4$ (LSCO), was reported to have a T_c of 36 K. It was not long after that Wu *et al.* [25] reported superconductivity in the now ubiquitous $YBa_2Cu_3O_7$ (YBCO) at a record high T_c of 93 K. In the few years following the initial discovery, researchers quickly began synthesizing and realizing superconductivity at comparably high T_c's in compounds like $Bi_2Sr_2Ca_{n-1}Cu_nO_{2n+4+x}$ (BSCCO) [26], $Tl_mBa2Ca_{n-1}Cu_nO_{2n+m+2}$ (TBCCO) [27] and $HgBa_2Ca_{n-1}Cu_nO_{2n+2+\delta}$ (HBCCO) [28].

Researchers quickly realized that this new class of materials could not be adequately described by the BCS theory that worked so well for metallic SCs. The cuprates exhibited high anisotropy due to their layered structures as well as prominent thermal fluctuation effects and smaller pair correlation lengths, ξ, associated with their high T_c's. Moreover, although the mechanism of electron pair formation remained valid, there was a growing body of experimental evidence to suggest that the superconducting energy gap contained nodes that could not be attributed to sample defects [29]. Additionally, the cuprates

exhibited the magnetic phase predicted by Abrikosov in 1957 in which the Meissner state could be penetrated by quantized regions of magnetic flux without destroying the superconductivity. All of these factors led researchers to create modified GL and BCS theories, such as anisotropic GL theory. These theories provided good models to describe the properties of the high-T_c systems listed above. However, there are many other features of the cuprates which cannot be explained by simple modifications to the GL and BCS theories, as we shall see in Chapter 4.

Two popular experimental methods of studying superconductivity and high-T_c superconductivity are nuclear magnetic resonance (NMR) and nuclear quadrupole resonance (NQR). An NMR experiment makes use of strong magnetic fields to measure the magnetic response of a system of spinful nuclei in the high-field limit where the Zeeman effect is dominant. On the other hand, NQR measurements are performed at zero or near-zero field where quadrupole interactions are dominant. The former method is our experimental probe of choice here. In particular we aim to study the nuclear magnetic response of a cuprate when the system is in the magnetic mixed state described by Abrikosov.

The purpose of this project is not only to study the Abrikosov vortex lattice with NMR, but to test the limits of the NMR probe in studying this mixed state in a cuprate system. We consider how much information we can reliably extract from an NMR spectrum and how much information we would need to obtain using alternative probes. This is particularly relevant to the study of vortex lattice geometry as we touch on in Chapter 6.

Our main focus is the vortex lattice, which should form at low temperatures in the mixed state. We have measured the NMR spectrum of an under-doped $HgBa_2CuO_{4+\delta}$ (Hg1201) sample and found no evidence for the formation of a vortex lattice even down to the lowest temperatures for fields between 14 T and 30 T and temperatures as low as 5 K. Our findings indicate that this phase of the mixed state does not exist in the under-doped Hg1201 system at these high fields and temperatures. These findings are described and discussed in the last few chapters.

1.1. Organization of this thesis

This dissertation is organized as follows. Chapters 2 and 3 present a review of the nuclear magnetic resonance (NMR) method as an experimental probe. In Chapter 2 we focus on the theoretical aspects of NMR in the semi-classical (vector) and quantum picture. In Chapter 3 we present experimental details such as how we produce magnetic fields, record measurements and analyze data. In Chapter 4 we review the characteristic features of cuprate SCs such as their general crystal structure and phase diagram. This chapter is also where we present our sample characterization for our single-crystal Hg1201 samples and discuss our isotope exchange and annealing procedure.

The majority of our data is presented in Chapters 5-7. In Chapter 5 we review some of the physics of the superconducting copper-oxide plane using the Mila-Rice-Shastry Hamiltonian as a way of understanding the influence of the nuclei on one another. We also present our ^{63}Cu and ^{17}O NMR relaxation results and discuss how they might be interpreted. We put the ^{17}O spin-spin relaxation results in the context of other similar

NMR results for YBCO samples.

Chapter 6 presents a review of the mixed state of type II SCs and the so-called *vortex lattice* that should occur in these systems at low temperatures. In this chapter we also present the details of how we can calculate the local field of a type II SC in an applied magnetic field using GL theory. We will discuss previous NMR studies of this vortex state on two other cuprates and how these results have been interpreted.

We present our own low-temperature data in the mixed state in Chapter 7. Here we also review some non-NMR data on this cuprate to compare these results to our own. Our particular focus is on a SANS study as well as magnetization creep measurements, both of which show evidence for a lack of long-range ordering in the vortex lattice across the layers of Hg1201 single crystals. In the final chapter, Chapter 8, we summarize our results and discuss what measurements are needed to draw stronger conclusions.

CHAPTER 2

Background: NMR Theory

Nuclear magnetic resonance (NMR) experiments allow us to probe a material's local electromagnetic environment through its interaction with the surrounding nuclear spins. Nuclear magnetic resonance measurements began in 1938 when Isidor Rabi *et al.*[30] measured the intensity of a beam of LiCl molecules after sending it through a series of magnetic fields. The experiment was similar to a Stern-Gerlach apparatus; the beam of neutral LiCl molecules was initially brought out of focus by an inhomogeneous field and subsequently refocused onto a detector by a small region of homogeneous field in which a hairpin loop also produced an oscillating field perpendicular to the homogeneous field. When the frequency of the oscillating field approached a certain characteristic frequency of either the Li or Cl the beam would no longer be refocused by the homogeneous field and the intensity observed at the detector dropped. This characteristic frequency will later be defined as the *Larmor frequency*.

The methods of modern NMR experiments were later developed independently by groups led by Bloch[31, 32] and Purcell [33] in 1946. These two groups implemented an inductive radio-frequency (rf) cavity in a homogeneous magnetic field to detect the resonant absorption of rf energy by the protons in a sample of liquid water (Bloch) and solid paraffin (Purcell). These methods were refined over the years to develop the NMR that

we use today.

The general set-up of a solid-state NMR experiment is as follows; a (in this case solid) sample containing a nuclear species with nuclear spin $I \neq 0$ is placed in a uniform magnetic field, $\boldsymbol{H}_o$. Once the system magnetization has reached equilibrium in this external field we apply a rf field, $\boldsymbol{H}_1$, which is perpendicular to $\boldsymbol{H}_o$. This rf field knocks the nuclear spin system out of equilibrium and creates a decaying magnetization in the perependicular plane which leads to an induced emf in the probe circuit (see 3.1.2) which produces a signal in the NMR spectrum. In this chapter we will discuss the information contained in such a signal. Specifically, we are interested in the relative frequency of the signal and how rapidly the signal decays. Here we present a brief overview of the NMR theory that is relevant to understanding the experimental results that we show in later chapters. We will discuss measurement equipment and experimental procedures in Chapter 3. For a more in-depth overview of NMR theory see references [34, 35, 22, 36].

2.1. Vector picture

In the classical picture an NMR signal arises from the alternating current produced in a coil that surrounds the system of nuclear spins which collectively precess about an axis at a frequency that we will denote by ω_L. In this picture the magnetic moment, $\boldsymbol{\mu}$, of a nucleus with spin, I, is a vector with magnitude, $\mu = \hbar\gamma I$, where γ is the nuclear gyromagnetic ratio, the ratio of the nuclear magentic moment to it's angular momentum, and $\hbar$ is the reduced Planck's constant. In a sample with N nuclei, each with magnetic moment, $\boldsymbol{\mu}_i$, where $i = 1, 2, \ldots, N$, the total magnetization, $\boldsymbol{M}$, is the average of all

magnetic moments,

$$\boldsymbol{M} = \frac{\sum_{i=1}^{N} \boldsymbol{\mu}_i}{N} = \langle \boldsymbol{\mu} \rangle.$$

In an NMR experiment we place the system of spins with magnetization $\boldsymbol{M}$ in a constant magnetic field, $\boldsymbol{H}_o = H_o \hat{\boldsymbol{z}}$, where $\hat{\boldsymbol{z}}$ is the unit vector along the z axis. The field will produce a torque $\boldsymbol{\tau}$ on the net magnetization given by,

$$\boldsymbol{\tau} = \boldsymbol{M} \times \boldsymbol{H}_o. \tag{2.1}$$

Recall that by definition γ is the ratio of the nuclear magnetic moment to its angular momentum. This means that the total angular momentum, $\boldsymbol{J}$, of the system with magnetization $\boldsymbol{M}$ is given by $\boldsymbol{J} = \boldsymbol{M}/\gamma$. Noting that the torque is the rate of change of the angular momentum we can re-write Eq. (2.1) as,

$$\frac{d\boldsymbol{M}}{dt} = \boldsymbol{M} \times \gamma \boldsymbol{H}_o. \tag{2.2}$$

We now move to a reference frame that rotates with frequency $\boldsymbol{\omega}$. In this frame the equation of motion, Eq. (2.2), becomes,

$$\begin{aligned} \frac{d\boldsymbol{M}}{dt} &= \boldsymbol{M} \times \gamma \boldsymbol{H}_o + \boldsymbol{M} \times \boldsymbol{\omega} \\ &= \boldsymbol{M} \times (\gamma \boldsymbol{H}_o + \boldsymbol{\omega}). \end{aligned} \tag{2.3}$$

If the frame rotates with angular velocity, $\omega = -\gamma H_o$, the angular momentum becomes stationary in the rotating frame. In this case the only torque on the system of nuclei must come from additional magnetic disturbances. This rotation frequency, known as the

Larmor frequency, is defined as $\omega_L \equiv \gamma H_o$.

In order to study properties of the nuclear magnetization we must exert an additional torque on $\boldsymbol{M}$ using a pulsed field $\boldsymbol{H}_1$ which we apply for a time t. We choose $\boldsymbol{H}_1$ to be along the x axis of the rotating frame such that Eq. (2.3) with $\omega = -\omega_L$ becomes,

$$\frac{d\boldsymbol{M}}{dt} = \boldsymbol{M} \times (\gamma H_1 \hat{x}), \tag{2.4}$$

to which solutions for $\boldsymbol{M}$ are sinusoidal functions of $\gamma H_1 t = \omega_1 t$ and the torque is in the y direction of the rotating frame. If the $\boldsymbol{H}_1$ pulse is applied for a time $t = t_{\pi/2}$, such that $\omega_1 t_{\pi/2} = \pi/2$, the magnetization will be flipped into the plane perpendicular to $\boldsymbol{H}_o$. When the rf field is turned off the nuclear magnetization will precess about the perpendicular axis indefinitely unless it is allowed to dissipate energy and return to its equilibrium state. This process is known as *spin-lattice relaxation* and we will discuss it in detail in 2.4.1.

2.2. The quantum mechanical picture

The vector model of NMR does a reasonable job of describing systems with nuclear spin $I = 1/2$ and cubic structural symmetry. However, for non-cubic solid state systems and systems with $I > 1/2$ there will also be a nuclear quadrupole moment which couples to the electric field gradient (EFG) produced by a system of atoms with non-cubic symmetry. In this case the quantum mechanical description becomes necessary to fully understand the mechanisms responsible for an NMR signal.

The Hamiltonian, $\hat{\mathcal{H}}_{\mathrm{NMR}}$, that describes a system of nuclei in an NMR experiment can generally be written as the sum of a Zeeman contribution, $\hat{\mathcal{H}}_Z$, and a quadrupole contribution, $\hat{\mathcal{H}}_Q$,

$$\hat{\mathcal{H}}_{\mathrm{NMR}} = \hat{\mathcal{H}}_Z + \hat{\mathcal{H}}_Q + \hat{\mathcal{H}}_{\mathrm{add}}(t).$$

Here $\hat{\mathcal{H}}_{\mathrm{add}}(t)$ represents additional contributions to the NMR Hamiltonian arising from fluctuation fields, hyperfine coupling, dipolar coupling, etc. Below we discuss the contributions from the Zeeman and quadrupole terms as well of a few examples of the additional contributions which are most relevant to the systems of interest in this dissertation.

2.2.1. The Zeeman Hamiltonian

When a nuclear magnetic moment, $\boldsymbol{\mu}$, is placed in the constant field, $\boldsymbol{H}_o$, the energy levels of the system are described by the Zeeman Hamiltonian, $\hat{\mathcal{H}}_Z$, where,

$$\hat{\mathcal{H}}_Z = -\hbar\gamma \hat{\boldsymbol{I}} \cdot \boldsymbol{H}_o. \tag{2.5}$$

This splits the nuclear energy levels into $(2I+1)$ equally spaced energies, E_m, where m is the quantum number that indexes the eigenvalues of $\hat{I}_z$, the component of the nuclear spin parallel to $\boldsymbol{H}_o$. The Zeeman energy levels are given by,

$$E_m = -\gamma\hbar H_o m, \tag{2.6}$$

where $m = -I, (-I+1), \cdots, (I-1), I$. Clearly, the energy difference betwen adjacent Zeeman levels, i.e. the energy needed to transition from a level with quantum number m

to one with quantum number $m \pm 1$ is,

$$\Delta E_{m,m\pm1} = \hbar\gamma H_o = \hbar\omega_L, \tag{2.7}$$

where ω_L is the Larmor frequency defined in Section 2.1.

The Zeeman Hamiltonian as written in Eq. (2.5) applies to a bare nuclear spin in a magnetic field. In a solid state system the nuclei are surrounded by other nuclei in various configurations. This creates, among other things, charge distributions and hyperfine fields that will couple to the nuclear spin and thereby alter the energy of transition. This will cause the NMR signal in the frequency domain (the precession frequency of $\boldsymbol{M}$ in the vector picture) to differ from the Larmor frequency. This shift is taken into account by the so-called *Knight Shift*, $\hat{K}$, which is a seecond-rank tensor [37]. The Zeeman contribution to the NMR Hamiltonian becomes,

$$\hat{\mathcal{H}}_Z = -\hbar\gamma\hat{\boldsymbol{I}} \cdot (\hat{1} + \hat{K}) \cdot \boldsymbol{H}_o. \tag{2.8}$$

The NMR signal (still considering only Zeeman contributions) will then appear at a frequency that is shifted from ω_L by some amount. The total Knight shift – or "NMR shift" – is measured with respect to the frequency, ω_{ref}, of the nucleus in a paramagnetic salt [34]. The total shift is then given as the following percentage,

$$K = \frac{\omega - \omega_{\text{ref}}}{\omega_{\text{ref}}} \times 100\%. \tag{2.9}$$

The shift value, K, is generally anisotropic and has many components, as we discuss in Section 2.3. We now turn to the other static (assuming the nuclei are stationary) contribution to $\hat{\mathcal{H}}_{NMR}$, the quadrupole interaction.

2.2.2. The Quadrupole Hamiltonian

When a solid-state system, e.g. a crystal, has a non-cubic symmetry the charge distribution of this arrangement of atoms will create a electric field gradient (EFG). The EFG at the nuclear sites is a tensor with elements given by, $V_{\mu\nu} = \frac{\partial^2 V}{\partial\mu\partial\nu}$, where V is the electric potential and μ and ν index the principal axes, $\mu, \nu = X, Y, Z$, of the EFG tensor[1]. The principal EFG components are defined such that, $|V_{ZZ}| \geq |V_{YY}| \geq |V_{XX}|$ and $V_{XX} + V_{YY} + V_{ZZ} = 0$ according to Laplace's equation. The latter condition also entails that the EFG tensor is traceless.

If the nuclei of interest have spins $I > 1/2$ the system will have a nuclear quadrupole moment which couples to the EFG. This coupling cuases the Zeeman eigenstates to split such that the levels are no longer equally separated by the $\Delta E_{m,m\pm1}$ in (2.7). The quadrupole moment coupling to the EFG is described by the quadrupole Hamiltonian, $\hat{\mathcal{H}}_Q$, which is given by[2],

$$\hat{\mathcal{H}}_Q = \frac{e^2 Q}{2I(I+1)} \sum_{\alpha} V_{\alpha\alpha} \hat{I}_{\alpha}^2, \tag{2.10}$$

[1]Note that we denote the principal EFG axes with capital X, Y, Z to avoid confusion with the laboratory frame where z is the direction of the uniform field, $\boldsymbol{H}_o$.
[2]Using the convention of reference [22].

where Q is the magnitude of the nuclear quadrupole moment, e is the electron charge and $\alpha = X, Y, Z$. This form of Eq. (2.10) assumes that $\boldsymbol{H}_o$ is parallel to one of the principal EFG axes. If we take the field to be parallel to V_{ZZ} the Hamiltonian becomes,

$$\hat{\mathcal{H}}_Q = \frac{eqQ}{4I(2I-1)}\left[3\hat{I}_z^2 - \hat{I}(\hat{I}+1) + \frac{\eta}{2}(\hat{I}_+^2 + \hat{I}_-^2)\right], \tag{2.11}$$

where $q = eV_{ZZ}$, $\eta = (V_{XX} - V_{YY})/V_{ZZ}$ is the asymmetry parameter and $\hat{I}_\pm = \hat{I}_x \pm i\hat{I}_y$ are nuclear spin ladder operators.

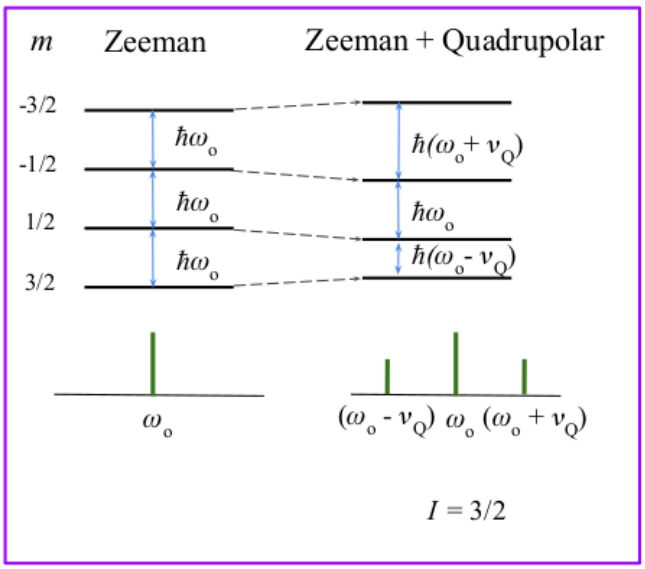

Figure 2.1. A cartoon energy diagram of the splitting (to first order) of the NMR spectrum of a $I = 3/2$ nucleus coupled to an external field $\boldsymbol{H}_o$ and an EFG. The quadrupole frequency is defined as $\nu_Q = 3eqQ/[h2I(2I-1)]$.

In NMR we work with fields that are strong enough that m is considered a good quantum number and the quadrupolar splitting can be taken into account by considering $\hat{\mathcal{H}}_Q$ to be a perturbation to $\hat{\mathcal{H}}_Z$. The new energy eigenstates can then be found using

perturbation theory. Figure 2.1 depicts the energy levels of a nuclear species with spin $I = 3/2$. The ground state energy level of the nucleus is split by the coupling between the nuclear spin and the field, $\boldsymbol{H}_o$, into $(2I + 1) = 4$ equally spaced energy levels. The presence of an EFG coupled to Q further splits the energy levels such that the transitions between the $(\pm 3/2 \leftrightarrow \pm 1/2)$ levels are shifted by a factor of ν_Q, the quadrupole frequency. The bottom half of the cartoon shows a sketch of the NMR spectrum in the frequency domain that one would expect for such a system. Note that this model takes only the Zeeman Hamiltonian and first order quadrupolar corrections into account.

2.3. Knight shift

We return now to the Knight shift, the shift in the NMR frequency from ω_L. The Knight shift is a consequence of the hyperfine (HF) coupling betwen the nuclear spin and the electronic spin system. It can be described by its own Hamiltonian, $\hat{\mathcal{H}}_{HF}$. We will define $\hat{\mathcal{H}}_{HF}$ as the component of Eq. (2.8) containing $\hat{K}$,

$$\hat{\mathcal{H}}_{HF} = -\hbar\gamma \hat{\boldsymbol{I}} \cdot \hat{K}(T) \cdot \boldsymbol{H}_o, \tag{2.12}$$

where T is the temperature. Here we will discuss only some of the common contributions to $\hat{\mathcal{H}}_{HF}$ that cause a shift in the NMR spectrum. A more detailed discussion of additional contributions to $\hat{K}$ can be found in references [2, 3] as well as the NMR literature mentioned at the start of this chapter.

2.3.0.1. Orbital shifts. The total Knight shift consists of a temperature-dependent component and a temperature-independent component. The temperature-independent

component arises from the coupling betwen the nuclear spin and the orbital angular momentum of the electronic system surrounding the nuclei. This term is known as the *orbital shift*, K_o. It's contribution to the hyperfine Hamiltonian is given by,

$$\hat{\mathcal{H}}_{HF}^{(o)} = -\hbar^2 \gamma_e \gamma_n \left(\frac{\hat{\boldsymbol{I}} \cdot \hat{\boldsymbol{L}}}{r^3} \right), \tag{2.13}$$

where $\hat{\boldsymbol{L}}$ is the orbital angular momentum operator for an electron at a distance r from the nucleus and γ_n, γ_e are the gyromagnetic ratios of the nuclear spin and the electron spin, respectively. The orbital shift is present down to the lowest temperatures and can usually be extracted by cooling the system down to near absolute zero. In a superconducting system K_o will be the only significant contribution to K at these temperatures as we explain below.

2.3.0.2. Hyperfine shifts. One of the most important temperature-dependent contributions to the total Knight shift in the study of superconductors is due to the electronic spin coupling to the nuclear spin. This is known as the *spin shift*, K_s. Although K_s is sometimes referred to as the Knight shift we will refer to it here as the spin shift to avoid confusion with the total shift.

The Hamiltonian describing this spin-spin interaction is also known as the magnetic hyperfine Hamiltonian because it arises from the coupling betwen the nuclear magnetic moment to the electron spin magnetic moment when both the nuclear spin, $\boldsymbol{I}$, and electron

spin, $\boldsymbol{S}$, are coupled to the external magnetic field $\boldsymbol{H}_o$. This Hamiltonian is given by,

$$\hat{\mathcal{H}}_{HF}^{mag} = -\hbar^2\gamma_n\gamma_e\hat{\boldsymbol{I}}\cdot\left[\frac{\hat{\boldsymbol{S}} - 3\hat{r}\cdot(\hat{\boldsymbol{S}}\cdot\hat{r})}{r^3} - \frac{8\pi}{3}\delta(\boldsymbol{r})\hat{\boldsymbol{S}}\right], \tag{2.14}$$

where $\delta(\boldsymbol{r})$ is a delta function. The last term in (2.14) is the hyperfine contact interaction which is relevant when the position of the electron is at the nucleus, i.e. the interaction with the electron spin s-orbital.

The spin shift is one of the most important parameters in NMR because it is directly related to the spin susceptibility, χ_s, of the electronic system surrounding the nuclear spins. In general, the spin shift is related to the electronic susceptibility by the hyperfine field, A, as follows,

$$K_s = A\chi_s. \tag{2.15}$$

This relation to χ_s is what makes K_s such an important parameter in the study of superconductivity where the spin susceptibility is a measure of the number of electronic spins coupled to the nuclear spin. At temperatures below the superconducting critical temperature, T_c, the conduction electrons begin to form spin-singlet pairs which have $S = 0$ and therefore no longer couple to I via the hyperfine interaction. The behavior of K_s at $T < T_c$ can give insight into the pairing symmetry of an electronic system (e.g. s-wave or d-wave). In fact, the d-wave interpretation of NMR shift and relaxation data of ^{63}Cu and ^{89}Y in YBCO [38, 39] played a large role in the acceptance of d-wave pairing theory in cuprates [22].

One of the simplest yet most illustrative examples of the significance of K_s is that of simple metals. In pure metals in which free electrons can be described by Bloch wavefunctions, $\psi_{\boldsymbol{k}}(\boldsymbol{r}) = u_{\boldsymbol{k}}(\boldsymbol{r})e^{i\boldsymbol{k}\cdot\boldsymbol{r}}$, the contact hyperfine term in (2.14) is the only contributing term [22]. In this case, $A = \frac{8\pi}{3}\langle|u_{\boldsymbol{k}}(0)|^2\rangle$, where the brakets denote an average over the Fermi surface, and the susceptibility, $\chi_s = \frac{1}{2}\gamma_e^2 n(E_F)$, is the spin susceptibility of the metallic *sp*-band. Here $n(E_F)$ is the density of states at the Fermi eneergy, E_F. This was the shift originally reported by W. D. Knight [37] in copper metal. Note that this shift is temperature-independent. This is a characteristic feature of metals which we will discuss further in Section 2.4.1.1.

2.3.0.3. Core polarization. High-T_c superconductors and *d*-band metals will have significant *d*-spin hyperfine coupling contributions to K_s through the first two terms of (2.14). However, electrons in these *d*-bands (as well as *p*- and *f*- bands) can also contribute to the hyperfine contact term through a process known as *core polarization*. This mechanism is a result of the Pauli exclusion principle which causes *s*-electrons of a certain spin band to have a higher energy than that of the opposite spin [22]. This results in a change in the hyperfine contact terms despite the fact that non-*s*-band electrons are not localized at the nucleus and thereby do not directly contribute.

2.3.0.4. Diagmagnetic shifts. In Section 2.3.0.1 we briefly discussed orbital shifts as arising from the coupling betwen the nuclear spin and the electron angular momentum. This shift will contain both paramagnetic and diamagnetic contributions. In superconductors, the diamagnetic contribution to K becomes appreciable at $T < T_c$ from the onset

of diamagnetic surface currents. This is known as the diamagnetic shift, K_{dia}. In practice this contribution to K can be calculated using the demagnetization factor, D, which is dependent on sample geometry[3]. The diamagnetic contribution to K is often very weak in high-T_c superconductors, such as the cuprates.

2.3.0.5. Nuclear dipole-dipole shift. All the interactions that we have discussed so far have been betwen the electronic system and the nuclear spin of one species. However, the nuclear spins will also interact with their neighboring nuclear spins. The Hamiltonian describing the interaction betwen a nuclear spin of species a and one of species b is [2],

$$\hat{\mathcal{H}}_{dip-dip} = -{}^{a}\gamma_n^{b}\gamma_n\hbar^2\left[\frac{\hat{\boldsymbol{I}}(\boldsymbol{r}_i)\cdot\hat{\boldsymbol{I}}(\boldsymbol{r}_j)}{|\boldsymbol{r}_i-\boldsymbol{r}_j|^3} - 3\frac{(\boldsymbol{r}_i\cdot\hat{\boldsymbol{I}}(\boldsymbol{r}_i))(\boldsymbol{r}_j\cdot\hat{\boldsymbol{I}}(\boldsymbol{r}_j))}{|\boldsymbol{r}_i-\boldsymbol{r}_j|^5}\right], \tag{2.16}$$

where $\boldsymbol{r}_{i,j}$ are the positions of nucleus i, j and ${}^{a,b}\gamma_n$ is the gyromagnetic ratio of nuclear species a, b. The nuclear dipole-dipole interaction will affect not only the shift of the NMR spectrum, but also the width of the frequency band of the transition. We will discuss this further in 2.4.2.

The interactions described above will lead to additional terms in the total NMR Hamiltonian. We have just seen how these additional contributions manifest in the frequency shift of an NMR spectrum. The other important measurement type in our experiments are measurements of the nuclear spin *relaxation rates*. We now turn to a brief overview of the theory of nuclear relaxation.

[3]Reference [40] provides calculations of D in rectangular prisms which can be used to extract K_{dia}.

2.4. Nuclear Relaxation

If an isolated nuclear spin in a uniform field $\boldsymbol{H}_o$ is brought out of equilibrium by an oscillating perpendicular field $\boldsymbol{H}_1(t)$ the spin will remain in the new unstable state after the rf field is turned off unless the system is allowed to dissipate the additional energy to return to equilibrium. In the classical picture this can be thought of as the magnetization vector returning to the $\boldsymbol{H}_o$ axis after being knocked into the plane perpendicular to $\hat{\boldsymbol{z}}$ by the field $\boldsymbol{H}_1$. In the quantum mechanical picture, where the equilibrium state is one in which the population of states is described by the Boltzmann distribution, this process can be described as a non-equilibrium distribution of spins exchanging energy with a reservoir to return to its equilibrium population distribution. The time scale on which the process just described occurs is known as the *spin-lattice relaxation time*, T_1. This is one of two relaxation mechanisms of great interest in NMR. In this section we will describe the relaxation processes of interest in NMR and what information they give us about our sample.

2.4.1. Spin-lattice relaxation

As previously described, the spin-lattice relaxation time, also known as the longitudinal relaxation time, T_1, is the time scale over which the population of the energy levels of a spin system return to a equilibrium distribution where the population is proportional to $\exp[-E_m/k_BT]$, where k_B is Boltzmann's constant, T is the system temperature and the E_m are the eigenvalues of $\hat{\mathcal{H}}_Z$. As we previously noted, in order for this relaxation to occur the nuclear spins must dissipate the energy that was added by the rf field by exchanging energy with some reservoir. This reservoir is the so-called "lattice" of the

surrounding nuclear and electronic spins. It is because of this interaction between the nuclear spin and its surroundings that T_1 is such an important parameter; it gives us information about the local electromagnetic environment of the sample on a length scale of the rf penetration depth below the sample's surface.

We can get a general idea of T_1 relaxation processes using a simplified model of a nuclear spin system with $I = 1/2$. In this case the system is a simple two-level system where the nuclear spin state can be either spin-up ($m = +1/2$) or spin-down ($m = -1/2$). Each individual spin in the system is taken to be in contact with a thermal reservoir of spins (the lattice) so that level transitions should be possible even in the absence of an external force (e.g. an rf field) driving transitions [34][4].

If the total number of spins in the system is N the populations of each state can then be denoted as N_+ and N_- and we can write a differential equation for the change in the population of the spin levels,

$$\frac{dN_\pm}{dt} = \pm(N_- W_\downarrow - N_+ W_\uparrow), \tag{2.17}$$

where $W_\uparrow$ is the rate of a transition from the $m = +1/2$ level to the $m = -1/2$ level[5] and vice versa for $W_\downarrow$. We can find the relationship betwen the two rates by noting that at

[4]The following derivation of the simplified expression for T_1 in a spin-1/2 system was adapted from [34] Chapter 1.

[5]Recall that the spin-down state will have a higher energy than the spin-up state.

equilibrium the rate of population change is zero. This gives,

$$\frac{W_\downarrow}{W_\uparrow} = \frac{N_+^0}{N_-^0}, \tag{2.18}$$
$$= e^{-\beta\Delta E},$$

where $\Delta E = E_+ - E_-$ is the difference betwen the two energy levels, $\beta \equiv 1/(k_B T)$ and the superscript 0 denotes the equilibrium state in which the level population is given by the Bolzmann distribution. If the spin system is split by the uniform field $\boldsymbol{H}_o$ then ΔE is the Zeeman energy, $-\hbar\gamma_n H_o$. This means that the rate of down transitions in terms of the rate of up transitions is,

$$W\downarrow = W_\uparrow e^{\beta\hbar\gamma_n H_o}. \tag{2.19}$$

In keeping with the tradition of statistical mechanics problem solving we then write the population differences in terms of $n = (N_+ - N_-)$ and $N = (N_+ + N_-)$ as,

$$N_+ = \frac{1}{2}(N + n), \tag{2.20}$$

$$N_- = \frac{1}{2}(N - n), \tag{2.21}$$

and write the transition rates, $dN_+/dt, dN_-/dt$ in terms of n and N. This gives,

$$\frac{dn}{dt} = N(W_\downarrow - W_\uparrow) - n(W_\downarrow + W_\uparrow). \tag{2.22}$$

If we then define $T_1^{-1} \equiv W_\uparrow(e^{\beta\hbar\gamma_n H_o} + 1) = W_\uparrow + W_\downarrow$, as the relaxation rate of n, the population difference betwen the two spin levels. We get the following relations for the

rates,

$$W_{\uparrow} = \frac{T_1^{-1}}{(e^{\beta\hbar\gamma_n H_o} + 1)}, \tag{2.23}$$

$$W_{\downarrow} = \frac{(T_1^{-1})e^{\beta\hbar\gamma_n H_o}}{(e^{\beta\hbar\gamma_n H_o} + 1)}. \tag{2.24}$$

The rate of population change is now,

$$\begin{aligned} \frac{dn}{dt} &= -\frac{1}{T_1}\left[n - N\frac{(e^{\beta\hbar\gamma_n H_o} - 1)}{(e^{\beta\hbar\gamma_n H_o} + 1)}\right] \\ &= -\frac{(n - n_0)}{T_1}, \end{aligned} \tag{2.25}$$

where n_0 is the equilibrium population difference which can be found by rearranging (2.18) and using (2.20) and (2.21) substituting $n = n_0$.

In deriving (2.25) we considered only the effects of a system in a static magnetic field, i.e. a system undergoing magnetization due to a constant field. The solution of (2.25) is,

$$n(t) = n_0(1 - e^{-t/T_1}). \tag{2.26}$$

Clearly, in this case of a spin-1/2 system in a constant field, T_1 is the time constant that describes the time it takes for a sample to become magnetized, or for n to change from its equilibrium value.

The above example can be expanded to describe the case of a nuclear spin system with $I > 1/2$ as well. To do this we return to (2.22) and add the index j to indicate

the transition. Here we work with difference variables $n_j = N_m - N_{(m+1)}$ [35]. We can approximate the level population as only being affected by the adjacent ($\Delta m = \pm 1$) energy levels. The difference equation describing the population difference, n_j is,

$$\frac{d(n_j)}{dt} = W_{(m+1)\to m} n_{(j+1)} - 2W_{m\to(m-1)} n_j + W_{(m-1)\to m} n_{(j-1)}. \tag{2.27}$$

In writing (2.27) we have assumed that both transitions out of the m state are equal, which is true in the high-temperature limit in which $\beta \ll \Delta E$, which is usually the case in an NMR experiment. A more illustrative form of (2.27) is as the matrix equation,

$$\frac{d\boldsymbol{n}}{dt} = \hat{\mathcal{D}}\boldsymbol{n}, \tag{2.28}$$

where $\hat{\mathcal{D}}$ is a matrix of relaxation rates and the components of $\boldsymbol{n}$ are the n_j defined above. The eigenvalues of $\hat{\mathcal{D}}$ are λ_i and the eigenvectors are $\boldsymbol{E}_i$ [2]. If we form a matrix $\hat{E}$ out of these eigenvectors such that $(\hat{E}^{-1}\hat{\mathcal{D}}\hat{E})_{ij} = \delta_{ij}\lambda_j$ then,

$$\begin{aligned} \frac{d\boldsymbol{n}}{dt} &= \hat{E}(\hat{E}^{-1}\hat{\mathcal{D}}\hat{E})\hat{E}^{-1}\boldsymbol{n}, \\ &= \hat{E}\lambda\hat{E}^{-1}\boldsymbol{n}. \end{aligned} \tag{2.29}$$

The above equation has solutions,

$$\boldsymbol{n}(t) = \hat{E}\hat{\Lambda}\hat{E}^{-1}\boldsymbol{n}(0), \tag{2.30}$$

where $\hat{\Lambda}$ is a diagonal matrix with elements given by exponentials, $\hat{\Lambda}_{ii} = e^{\lambda_i t}$ and $\boldsymbol{n}(0)$ are the initial population differences. The elements of $\boldsymbol{n}(t)$ are then composed of a sum of exponentials. The magnetization profile for the j^{th} transition is proportional to the

corresponding $n_j(t)$. Therefore, for a nucleus of spin I in a spin system the matrix $\hat{\mathcal{D}}$ will give a functional form of $M_j(t) \propto -n_j(t)$. In an NMR experiment we extract T_1 by measuring $M_j(t)$ over a certain range of time. Therefore, we can use the form of $M_j(t)$ for a specific I to extract T_1 from our experimental data. We will discuss how we perform these measurements in the next chapter.

We have just described a simplified picture that allows us to find T_1 in a system of nuclear spins with $I > 1/2$. A more complete description of the effect of spin-lattice interaction can be found by using the density matrix formulation. In this case the nuclear spin ensemble is represented by the density matrix, $\hat{\rho}(t)$, and T_1 can be found by using time-dependent perturbation theory to calculate the rate of transition between two spin levels, m and $m \pm 1$, in the presence of a perturbation $\hat{\mathcal{H}}_1(t)$. This rate is given by the average expectation value of the rate of change of the density matrix. This rate of change is (to second order)[34],

$$\frac{d\hat{\rho}^*(t)}{dt} = \frac{i}{\hbar}\left[\hat{\rho}^*(0), \hat{\mathcal{H}}_1^*(t)\right] - \frac{1}{\hbar^2}\int_0^t dt' \left[\left[\hat{\rho}^*(0), \hat{\mathcal{H}}_1^*(t')\right], \hat{\mathcal{H}}_1^*(t)\right], \tag{2.31}$$

where the * indicates that the operators are in the interaction representation, $\hat{\rho}^*(t) = e^{(i/\hbar)\hat{\mathcal{H}}_{NMR}t}\hat{\rho}(t)e^{-(i/\hbar)\hat{\mathcal{H}}_{NMR}t}$; here $\hat{\mathcal{H}}_{NMR}$ is the Zeeman Hamiltonian and all other stationary contributions to the NMR system. Another advantage of the density matrix formulation is that, assuming we keep the off-diagonal elements of $\hat{\rho}$, it can also be used to calculate the spin-spin relaxation time, which we will discuss in 2.4.2. For a detailed derivation and example of the use of the density matrix formulation see Appendix B or

Chapter 5 of [34].

Note that if $\hat{\mathcal{H}}_1$ is constant in time T_1 can be calculated using Fermi's golden rule for the transition rate between two states which differ by $\Delta m = \pm 1$. An example of such a case is that of a simple metal.

2.4.1.1. The Korringa relation. In Section 2.3.0.2 we saw that the spin shift of a *sp*-band metal was independent of temperature and given by,

$$K_s = \frac{4\pi}{3}\hbar^2\langle|u_k(0)|^2\rangle\gamma_e^2 n(E_F). \tag{2.32}$$

We can now use the results of the previous section to find the corresponding T_1 for such a metallic system. Here, $\hat{\mathcal{H}}_1(t) = \hat{\mathcal{H}}_{HF}^{mag}$ from (2.14). We consider only the contact interaction because in the system we are considering (a metal with cubic symmetry) the higher order orbital couplings are negligible [22]. The golden rule for the rate of transition betwen a state 1 and state 2 is,

$$W_{2,1} = \frac{2\pi}{\hbar}\left|\langle 2|\hat{\mathcal{H}}_1|1\rangle\right|^2\delta(E_1 - E_2), \tag{2.33}$$

where $E_{1,2}$ is the energy of state 1 and 2, respectively. Here $\hat{\mathcal{H}}_1 = (8\pi/3)\hbar^2\gamma_n\gamma_e\delta(r)\hat{\boldsymbol{I}}\cdot\hat{\boldsymbol{S}}$ and we want to find the rate for the transition from a state indexed by nuclear spin quantum number m and electron wavefunction $\psi_{\boldsymbol{k}} = u_{\boldsymbol{k}}e^{i\boldsymbol{k}\cdot\boldsymbol{r}}$ to a state indexed by $m{+}1$ and electronic wavefuntion $\psi_{\boldsymbol{k}'} = u_{\boldsymbol{k}'}e^{i\boldsymbol{k}'\cdot\boldsymbol{r}}$. Additionally, because $\hat{\boldsymbol{I}}\cdot\hat{\boldsymbol{S}} = \hat{I}_z\hat{S}_z + \frac{1}{2}(\hat{I}_+\hat{S}_- + \hat{I}_-\hat{S}_+)$ any $\Delta m = +1$ transition must also be accompanied by a transition from the electronic spin-down state to the spin-up state. Therefore, our initial electron state must be the

spin-down and the final state will be spin-up. Our golden rule expression is then,

$$W_{(\boldsymbol{k}_\downarrow m)\to(\boldsymbol{k}'_\uparrow m+1)} = \frac{2\pi}{\hbar}\left(\frac{4\pi\hbar^2\gamma_n\gamma_e}{3}\right)^2 \left|\langle \boldsymbol{k}'_\uparrow(m+1)|\delta(r)\hat{I}_+\hat{S}_-|\boldsymbol{k}_\downarrow m\rangle\right|^2 \delta(E_k - E_{k'}). \tag{2.34}$$

The delta function will pull out the $r = 0$ terms of the electron wavefunctions -the components of the wavefunctions at the nucleus- only and the $\hat{I}_+\hat{S}_-$ products will give us a factor of $(I-m)(I+m+1)$. The spin-lattice relaxation rate will be given by the coefficient of the $(I-m)(I+m+1)$ term [22]. The sum over $\boldsymbol{k}, \boldsymbol{k}'$ can be replaced by energy integrals using the density of states, $n(E)$, and the Fermi function, $f(E)$. This final relaxation rate is,

$$\begin{aligned} \frac{1}{T_1} &= \frac{4\pi k_B T}{\hbar}\left[\frac{4\pi}{3}\gamma_n\gamma_e\hbar^2\langle|u_{\boldsymbol{k}}(0)|^2\rangle n(E_F)\right]^2 \\ &= \frac{4\pi k_B T\gamma_n^2}{\hbar\gamma_e^2}K_s^2. \end{aligned} \tag{2.35}$$

This leads to the famous *Korringa relation*,

$$\frac{1}{T_1 T} = \left(\frac{4\pi k_B\gamma_n^2}{\hbar\gamma_e^2}\right)K_s^2, \tag{2.36}$$

which is independent of temperature. This calculation by Korringa [41] agrees remarkably well with the relaxation behavior of simple metals with cubic crystal structures. Even in more complex structures there are often ranges of temperature over which $1/(T_1T)$ is constant. This behavior is referred to as "Korringa-like." A notable example of Korringa-like $(T_1T)^{-1}$ behavior is that of ^{89}Y in the high-T_c cuprate superconductor $YBa_2Cu_3O_7$ at high temperatures ($T > T_c$) [42].

We have seen that T_1 is an important time scale, reflecting the energetics of the magnetization relaxation which allows us to probe physical properties through NMR. However, there is a second crucial time scale in NMR that we have yet to address fully which is the time over which a system of precessing nuclear spins can be considered as a single coherent magnetization. While T_1 gives us information about energy transfer and population differences it does not give us information about fluctuating longitudinal fields which will affect our ability to measure an NMR spectrum in the first place. In order to get the full picture we need a second relaxation time, T_2, which we describe below.

2.4.2. Spin-spin relaxation

The other key timescale in an NMR experiment is the so-called *spin-spin relaxation time*, T_2. In the vector model this is the timescale over which the perturbed magnetization vector "spreads out" (see Fig. 2.2) in the perpendicular plane due to the individual spin vectors precessing at different rates. In the quantum picture T_2 is also known as the "de-coherence time" because it is the timescale over which the individual nuclear spin states lose coherence after an $\boldsymbol{H}_1$ pulse. Unlike the spin-lattice relaxation process, the

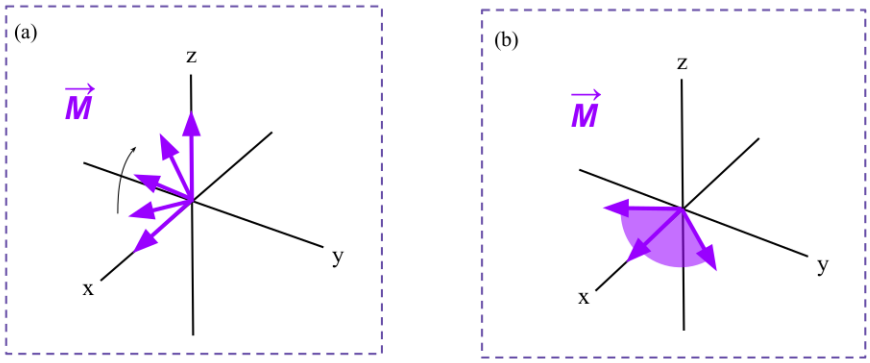

Figure 2.2. A cartoon visualization of (a) the spin-lattice relaxation time, T_1, and (b) the spin-spin relaxation time, T_2, in the classical picture.

spin-spin relaxation mechanism does not involve any actual transfer of energy because it is only the phase of the individual spin states that is changing, not their energies. The length of T_2 will be influenced by the variation in the z- component of the field, H_z, across all nuclear spins. This effect can by amplified by inhomogeneity in in the applied field which will increase the spread of H_z. Additionally, if a nucleus changes position by a mechanism such as diffusion the magnetic moment will gain an additional phase due to this translation. The accumulated phase of nuclei at various positions in the sample leads to a shorter observed T_2.

2.4.2.1. The rigid-lattice limit. If the nuclei in a sample are completely stationary one can calculate the effect of nuclear dipole-dipole interactions (see 2.3.0.2) on the observed T_2 using the method of moments[6] to compute the broadening of the Zeeman states due to this interaction. We will refer only to the so-called "second moment," $\langle \Delta\omega^2 \rangle$, which is on the order of the square of the measured linewidth (the width of the frequency of a transition). The second moment describing the local field in a system of N nuclear spins is,

$$\langle \Delta\omega^2 \rangle = \frac{3}{4}\gamma^4\hbar^2 I(I+1)\frac{1}{N}\sum_{j,k}\frac{(1-3\cos^2\theta_{jk})^2}{r_{jk}^6}, \tag{2.37}$$

where γ is the nuclear gyromagnetic ratio, θ_{jk} is the angle betwen the vector connecting nucleus j and k and the field $\boldsymbol{H}_o$ and r_{jk} is the distance betwen nucleus j and nucleus k. Eq. (2.37) describes the seecond moment for the spin-spin coupling between nuclei of the same species. If we are observing the resonance of spin species 1 which couples to spin

[6]Reference [34] Chapter 3.

species 2 the second moment is given by,

$$\langle \Delta\omega^2 \rangle_{1,2} = \frac{1}{3}\gamma_1^2\gamma_2^2\hbar^2 I_2(I_2+1)\frac{1}{N}\sum_{j,k}\frac{(1-3\cos^2\theta_{jk})^2}{r_{jk}^6}. \tag{2.38}$$

The T_2 corresponding to the second moment in the rigid latice limit is the inverse square of $\langle \Delta\omega^2 \rangle$,

$$T_2^{-1} = \langle \Delta\omega^2 \rangle^{1/2}.$$

The rigid lattice T_2 calculation is useful for determining the source of spin-spin relaxation in a solid sample e.g. a single crystal. This can be useful, for example, if one wishes to isolate the contributions to T_2 that are not caused by internuclear dipole coupling[7].

2.5. Conclusions

In this chapter we reviewed the basic concepts of NMR in both classical and quantum mechanical pictures. We saw that the Hamiltonian that describes the NMR spectrum is the Zeeman Hamiltonian for an ensemble of nuclear spins in a field $\boldsymbol{H}_o$. We have seen that additional contributions from quadrupole coupling, nuclear dipole coupling, as well as hyperfine coupling will shift the frequency of the NMR signal as well as alter the characteristic magnetization time, T_1. Additionally, we have seen the example of how the spin shift and T_1 behave in a simple metal. In the following chapter we will see how one measures the relaxation rates in practice as well as how we set up an NMR measurement in the laboratory.

[7]See, for example, Recchia *et al.* [43].

CHAPTER 3

Experimental NMR

In the previous chapter we briefly touched on the setup of an NMR experiment. In order to perform a measurement of nuclear magnetization one requires a sample, a uniform magnetic field H_o, an inductive cavity and a signal detection system. In this chapter we will discuss the technical details of the NMR experiments reported herein beginning with our equipment and the signal processing software and hardware that allows us to run our pulse sequences, which we will describe in detail in the later sections.

3.1. Hardware

In order to generate a H_o that is suitable for an NMR experiment we need a strong magnet with reasonable (less than 10 ppm at the center field) field homogeneity as well as an inductive coil to provide our rf field, H_1. The coil also serves as a detector in that it is the change of inductance of the coil due to a decaying sample magnetization which produces the induced emf in the NMR circuit which leads to a signal in our measured spectrum [36]. Additionally, we require a spectrometer and computer to send and receive rf signals, convert analog signal to digital information and store the data for analysis.

The majority of the experiments reported herein were performed at Northwestern University in an Oxford 600/51 warm-bore superconducting magnet with a near constant field of 14 T. The center field of the magnet is about 14.103 T when fully energized and

Figure 3.1. The sample stage and coil used in our high-field experiments at NHMFL. The direction of the H_1 field is indicated by the arrow and the label. The H_o field is perpendicular to H_1 and runs parallel to the axis of the of the probe.

has a field drift of approximately 0.2 ppm per day [44]. The majority of our coils were made using copper wire[1] with a diameter of 28 AWG for ^{63}Cu and ^{199}Hg NMR and 32 AWG for ^{17}O NMR. The inductance of the coil must allow for the resonant frequency of the probe circuit (see 3.1.2) to be tuned to the desired frequency and impedance matched to 50 Ω at that frequency. The ^{63}Cu in the coil can also be used as a benchmark nucleus to characterize the exact field strength prior to an NMR measurement.

[1]For ^{63}Cu NMR we make our coils with Ag wire to avoid contaminating the sample signal with that of pure metallic Cu.

Our Hg1201 single crystal samples are very fragile and must be kept in an external sample holder to avoid excessive handling and exposure to impact. We make the majority of our sample holders using borosilicate glass NMR tubes which we cut to a length of about 1 cm with a diamond blade and mold using a torch and a pair of pliers to fit closely to our sample dimensions. The sample holder and coil should be as close to the sample size as possible in order to maximize the filling fraction, i.e. the fraction of the space inside the coil that is filled by the sample.

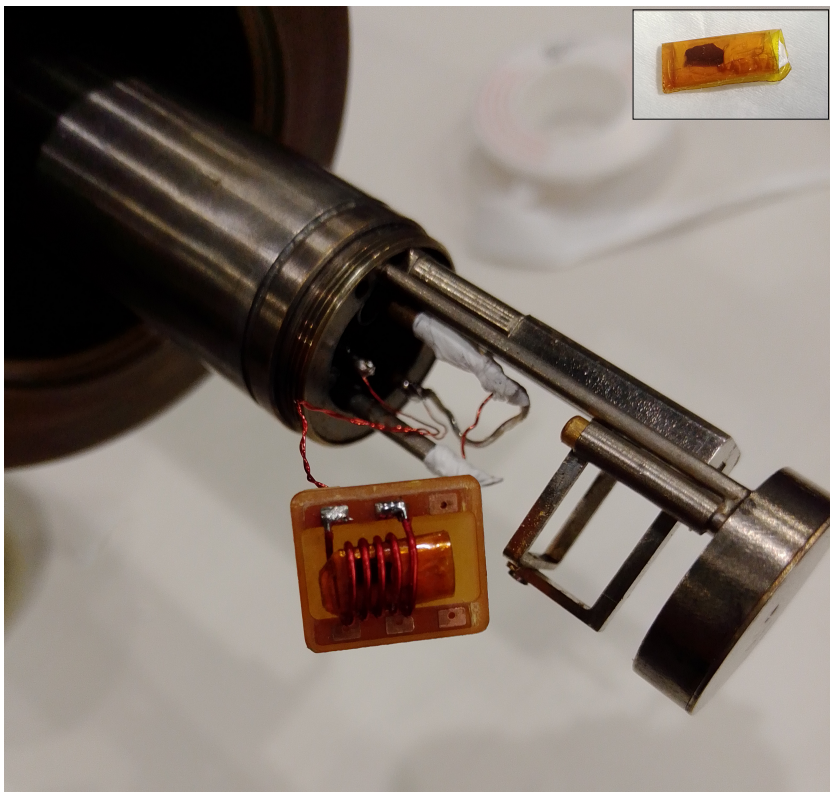

Figure 3.2. The picture shows a Cu coil encasing the sample holder used for high-field measurements. The inset shows an image of the sample inside the sample holder. The crystal c-axis of the sample is perpendicular to the surface shown.

Our high-field ($H_o > 14$ T) and low-temperature ($T < 20$ K) NMR experiments were performed at the National High Magnetic Field Laboratory (NHMFL) in Tallahassee, Florida. These measurements utilized an all-superconducting cold-bore magnet with a maximum field of 32 T [45]. Temperature control was achieved using a variable temperature insert (VTI) with a range from 1.4 - 300 K. The sample holder used in these experiments consists of several layers of 0.0025 inch thick Kapton polyimide masking tape (see the inset of Fig. 3.2) and a few pieces of Teflon tape to restrict the motion of the sample.

3.1.1. Spectrometer

All of our measurements, including those at the NHMFL, are performed with a MAGRes2000 spectrometer designed by A. P. Reyes. For more details on the spectrometer hardware and software, a technical user's manual can be found in reference [1]. The spectrometer hardware consists of a pulse programmer, which controls digital input/output (I/O) operation through an external PC timing card; an analog-to-digital converter (ADC), which is also a PC card; and a home-built rf-module which transmits and receives pulses to and from the NMR probe, respectively.

The experiments performed at Northwestern University in a 14 T field utilize a GT50-DIO PC I/O card from GeoTest® Inc. to control the timing of the pulses in the NMR experiment. The timing card also interfaces with a PTS500 frequency synthesizer for remote pulse programming and phase control. The phase sensitivity of the PTS500 allows us to perform all experiments with quadrature detection, which we discuss below. The

ADC card used for signal acquisition is a GaGe® Compuscope CS1250 PCI card with 12-bit digitization and 4 MB of memory.

3.1.1.1. Quadrature detection. All of our NMR experiments are performed with a quadrature detection sequence, meaning that the phase of the transmitted signal as well as the receiver phase, is rotated through multiples of four permutations of relative phases in order to average out any spurious signal contributions that can accumulate if the signal detection-acquisition is performed at only one phase. Quadrature detection is also a way of avoiding accumulating errors in the measured signal due to electronic drift [36]. The table below shows the 16 phase combinations in our standard Hahn echo (see 3.2.2) measurements where the phase of the first ($\pi/2$) and second (π) pulses as well as the receiver are denoted by the symbols $\pm x$ (0° and 180°) and $\pm y$ (90° and 270°).

$\pi/2$	y	$-x$	$-y$	x	y	$-x$	$-y$	x	y	$-x$	$-y$	x	y	$-x$	$-y$	x
π	x	x	x	x	y	y	y	y	$-x$	$-x$	$-x$	$-x$	$-y$	$-y$	$-y$	$-y$
receiver	$-y$	$-x$	y	x	y	x	$-y$	$-x$	$-y$	$-x$	y	x	y	x	$-y$	$-x$

3.1.1.2. RF module. The rf module consists of an integrated signal transmitter and receiver unit. The transmitter generates quadrature gated rf signals by passing the signal generated by the PTS500 frequency synthesizer through an equal power splitter and using this split signal as the reference for both transmitter and receiver section. On the transmitter side the reference is sent to a gated phase shifter which sets the correct phase of the signal before it enters a series of attenuators (the attenuation can be set by the user) followed by an rf power amplifier and finally the NMR probe circuit. The receiver

section consists of an additional variable attenuator and two wideband, double-balanced rf mixers, which multiply the output signal from the probe circuit with the reference signal from the PTS500 and sends the resulting intermediate frequency (IF) signal to the computer for digitization and analysis. Fig 3.3 shows a block diagram of the rf module.

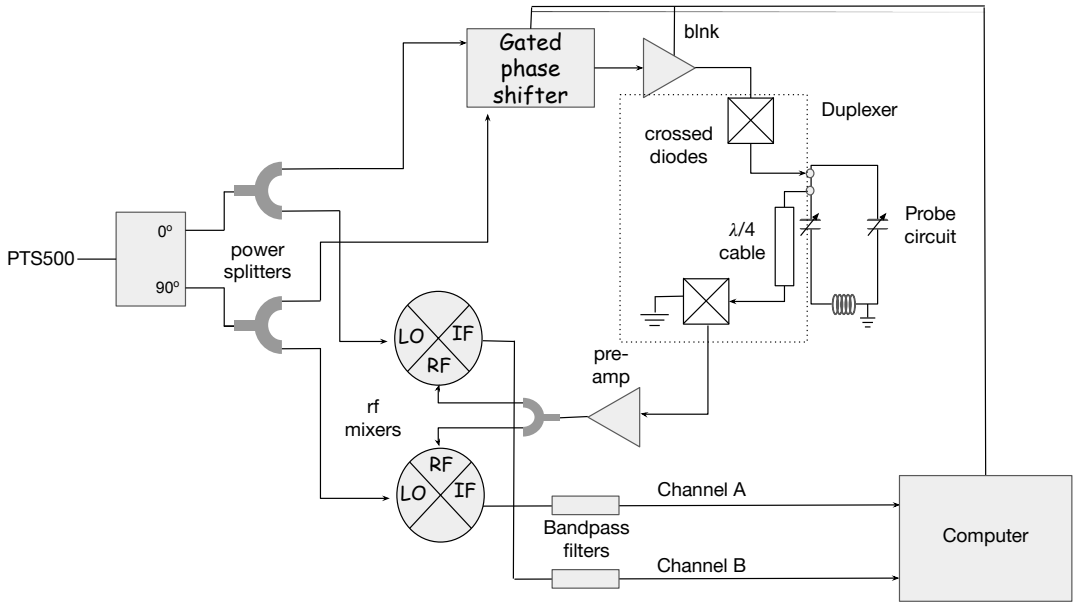

Figure 3.3. A block diagram of the MagRes rf module adapted from references [1, 2, 3, 4].

The transmitted and received signals also pass through a duplexer section upon entering and leaving the probe circuit. The duplexer section isolates the high-power rf input signal from the transmitter circuit and the low-power output signal from the induced emf of the NMR circuit. In this sense the duplexer can be thought of as the border between the transmitter and the receiver section of the rf module; it divides the two sections and prevents the signals from one contaminating the other. For our experiments at NU this

signal isolation is accomplished using crossed diodes and a so-called "$\lambda/4$ cable." On the transmitter side a pair of crossed diodes prevents the low-power rf signal from re-entering the transmitter section by providing a high impedance in this direction. Similarly, the $\lambda/4$ cable and shunted crossed diodes on the receiver side reflect high-power rf signals and prevent them from entering the pre-amplifier.

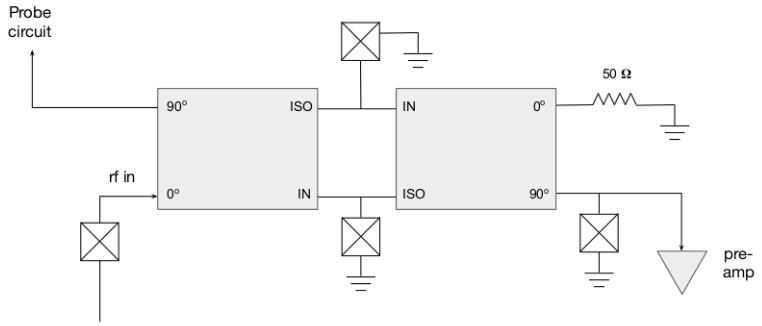

Figure 3.4. A block representation of the quadrature hybrid duplexer circuit used at the NHMFL. The quadrature hybrid coupler ports are labeled assuming the input signal enters from the port labeled "IN."

The duplexer used for our high-field experiments at the NHMFL utilizes a pair of quadrature hybrid couplers rather than a $\lambda/4$ cable. These hybrid couplers are Anaren four-port, 3 dB directional couplers with a 90° phase difference between the two output ports and an isolation rating of 21 dB. The quadrature hybrid circuit is shown in Fig. 3.4. Note that the port labels in the circuit diagram assume only an input signal from one port. In general, if a signal enters one port that port becomes the "IN" port from which the signal is split with equal power to the two output ports on opposite sides of the coupler with a relative phase shift of 90° between each output port [46]. The couplers isolate the rf port from the pre-amplifier by ensuring that the phase shifts of the recombining signals from

this port cancel at the port connected to the receiver. The same is true for the receiver and rf input section. The quadrature hybrid duplexer has a wider frequency bandwidth than the $\lambda/4$ cable but has more loss on the transmission side of the rf module [2].

3.1.2. Probe circuit

The NMR probe circuit consists of two variable capacitors and an inductive coil with inductance L. The capacitors are placed in series and parallel with the inductor such that one capacitor, C_{M}, is used to match the impedance of the probe circuit and the other, C_{T}, is used to tune the resonance frequency of the circuit. The two ways to arrange the capacitors and inductor are known as PTSM (Parallel-Tuned Series-Matched) and STPM (Series-Tuned Parallel-Matched); the experiments reported in later chapters were performed using the latter. Most of the data reported in this thesis was measured using a

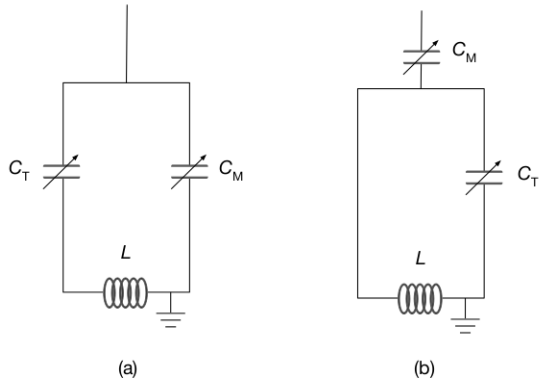

Figure 3.5. A circuit diagram depiction of the (a) STPM and (b) PTSM probe circuits.

high-field probe designed by Reyes *et al.* as detailed in reference [47]. We used a home-built continuous flow cryostat designed and build by Lee with inspiration from reference [48] to achieve temperatures between 285 K and 20 K.

3.2. Pulse sequences

We now move on to discuss how we program our transmitted signals to measure certain nuclear relaxation properties. These sequences are set using the MAGRes pulse programming module described in detail in [1].

3.2.1. FID

The most basic NMR pulse sequence is the so-called "Free Induction Decay" (FID). In an FID the $\boldsymbol{H}_1$ field is turned on for a time, $t = t_{\pi/2}$, such that $\gamma H_1 t_{\pi/2} = \pi/2$. In the semi-classical picture this "$\pi/2$ pulse" rotates the nuclear magnetization vector, $\boldsymbol{M}$, into the plane perpendicular to $\boldsymbol{H}_o$ such that the magnetization induced in the coil is maximized at a time $t = \tau$ and subsequently decays to zero. This pulse sequence is often repeated many times at a repetition time, $T_R > 5T_1$, in order to allow the system to reach its equilibrium spin population distribution before each repetition. The signals from each repetition are added together to increase the signal-to-noise (S-N) ratio of the NMR spectrum.

There are several problems that arise with the FID measurements in practice. Since the magnet used to produce the external field will have some inhomogeneity, ΔH_o, the individual nuclear spins that make up the net magnetization will precess at diferent rates in different regions of the sample. In quantum mehanical terms, the nuclear spins will lose coherence on a time scale faster than T_2. This decoherence time due to field inhomogeneity is known as T_2^* where $T_2^* \leq T_2$ [36]. In many cases this additional decoherence due to field inhomogeneity causes the FID signal to decay so rapidly that the spectrometer cannot

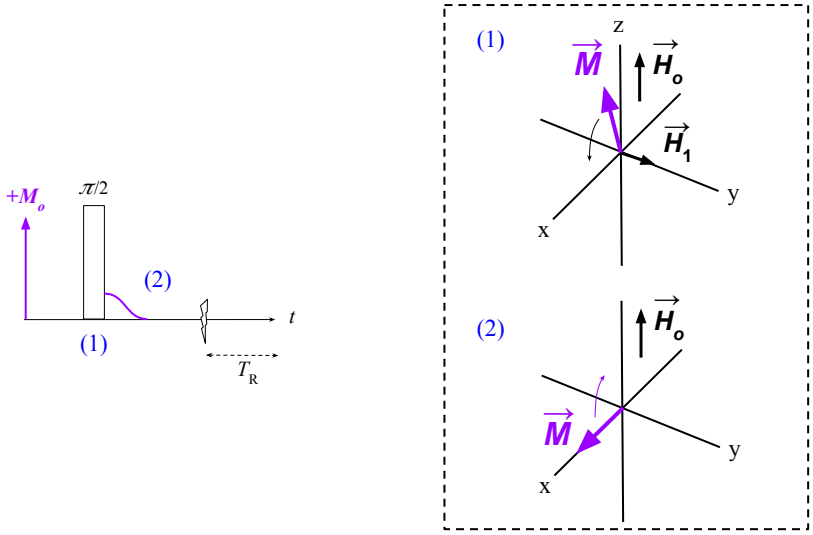

Figure 3.6. A cartoon of the free-induction-decay (FID) process in terms of the magnetization vector (right) and the pulse timing diagram (left). The first step (1) involves applying a field H_1 for a time $t_{\pi/2}$ such that the magnetization is knocked into the plane perpendicular to H_o; step (2) is to record the magnetization induced in the coil while the nuclear magnetization relaxes back to equilibrium. In the timing diagram the horizontal axis depicts the elapsed time in an experiment and the vertical axis depicts the sample magnetization (purple) as well as the H_1 pulse (rectangle) which is applied for a time such that $\gamma H_1 t = \pi/2$.

record the full signal and valuable information is lost. Experimentalists can mitigate this loss of coherence by using the Hahn echo technique.

3.2.2. Hahn Echo

In 1950 E. L. Hahn published his work [49] detailing a revolutionary pulse sequence, the so-called "Hahn Echo." This pulse sequence removes the effect of field inhomogeneity by applying a second "re-focusing" pulse at a time $t = \tau$ after the initial $\pi/2$ pulse. The refocusing pulse is applied for a length of time such that $\gamma H_1 t = \pi$ (a "π-pulse"). The effect of this refocusing pulse is to rotate the individual nuclear spins in the perpendicular

plane such that the magnetization refocuses along one axis at a time $t = 2\tau$, creating a maximum magnetization signal at this time.

As with the FID, this sequence is often repeated and the signal averaged until the desired

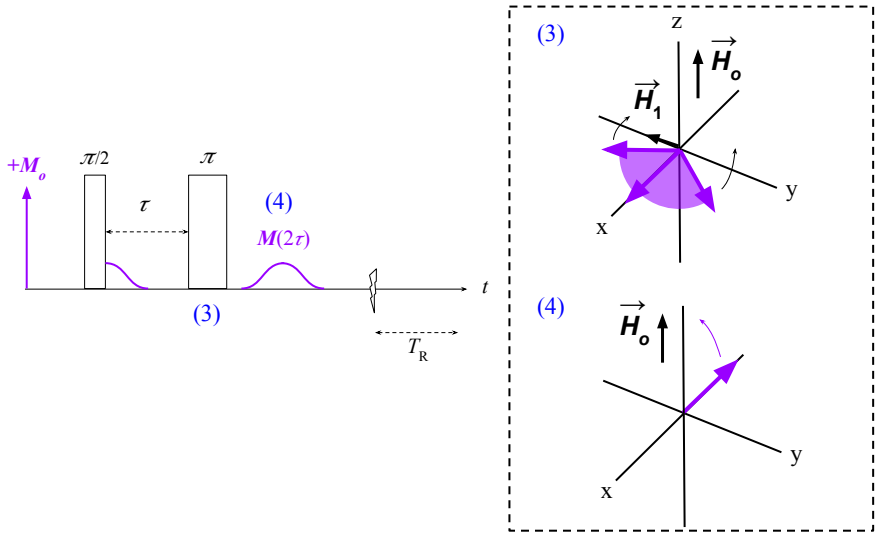

Figure 3.7. The Hahn echo sequence begins as an FID (see Fig. 3.6 for steps (1) and (2)) but at time $t = \tau$ after the $\pi/2$ pulse we apply a second rephasing pulse (3) such that we see a maximum signal at time $t = 2\tau$ (4).

S-N ratio is achieved.

3.2.3. CPMG

The Hahn echo method is very useful for measuring NMR spectra and variations of it can be used to measure relaxation rates, as we will describe later in this section. However, when a nuclear spin system has a very long relaxation time the repetition time needed[2] between each Hahn echo to obtain a spectrum with an acceptable S-N ratio can be prohibitively expensive. One way to improve the S-N in less time is to use the Carr-Purcell-Meiboom-Gill (CPMG) method.

[2]Recall that T_R should be set to at least $5T_1$ in an NMR measurement.

A CPMG experiment begins the same way as a Hahn echo, with a $\pi/2$ pulse to saturate

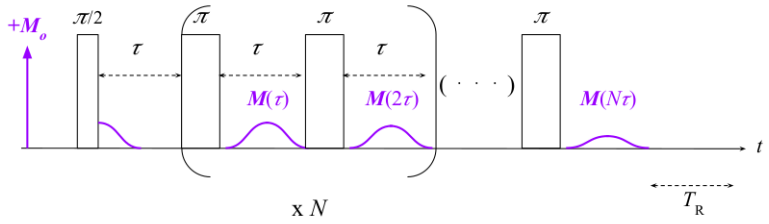

Figure 3.8. A cartoon depiction of the Carr-Purcell-Meiboom-Gill (CPMG) method. The sequence begins with a $\pi/2$ pulse followed by a train of N π pulses which gives N echoes. The magnitude of the echoes decay over time such that their decay rate can be used to measure T_2. The N echoes can also be summed to improve the S-N of a measurement in less time than it takes to run N Hahn echo sequences.

the spin levels and a subsequent π pulse at time $t = \tau$ to refocus the magnetization. However, instead of waiting for a time T_R for the magnetization to return to equilibrium before repeating the sequence one will apply another π pulse at $t = 2\tau$ which will refocus the magnetization again in the perpendicular plane. This process continues with a train of π pulses being applied in time intervals of $\Delta t = \tau$ with spin echoes appearing after each π pulse. One can improve the S-N by summing all the echoes in a CPMG spectrum similar to how one would add spectra together in standard signal averaging.

The FID and Hahn echo are the most basic NMR pulse sequences used to obtain a spectrum. However, if one wants to measure T_1 or T_2 one will need to measure the spectrum multiple times with different pulse conditions in order to see the effect on the magnetization. Below we discuss some common methods of measuring the spin-lattice and spin-spin relaxation rates.

3.2.4. Measuring T_2

The two most common sequences used to measure T_2 are the Hahn echo and CPMG.

3.2.4.1. CPMG for T_2 measurements. As we just saw, a CPMG spectrum that uses N π pulses will contain N spin echoes each separated by time intervals of $\Delta t = \tau$. The amplitude of these echoes should decay with a time constant of T_2. Thereby, one can extract the T_2 from a CPMG spectrum by fitting the signal decay as a function of time to an exponential function.

The sequence described in section 3.2.3 is actually referred to as the Carr-Purcell (CP) sequence and was developed by Carr and Purcell in 1954 [50]. This was later modified by Meiboom and Gill in 1958 [51] to correct for errors due to the π pulses not being perfectly 180° and the effects of $\boldsymbol{H}_1$ inhomogeneity [36] which resulted in measured T_2's that were too small. The modified sequence, the CPMG sequence, improved the accuracy of the T_2 measurement by alternating the phase of the π pulse to be phase shifted by 90° with respect to the initial $\pi/2$ pulse. This is to avoid accumulating errors due to these imperfect experimental conditions.

3.2.4.2. Hahn echo T_2 measurement. We previously described the Hahn echo experimental setup as a pulse sequence of $\pi/2 - \tau - \pi -$ acquire; however, if we want to measure T_2 we need to change the time, τ, at which we apply the π pulse and acquire the signal and subsequently observe the effect on the magnitude of the magnetization. In a Hahn echo T_2 measurement one repeats the Hahn echo sequence at increasing τ values until the signal is no longer detectable. One can extract T_2 by fitting the decaying magnetization

amplitude, $M(t)$, as a function of $t = 2\tau$ to the following expression,

$$M(2\tau) = M_o \exp\left[-\frac{2\tau}{T_{2e}} - \left(\frac{2\tau}{T_{2g}}\right)^2\right], \tag{3.1}$$

where T_{2e} is the Lorentzian (exponential) decay contribution and T_{2g} is the Gaussian contribution. Often times the decay profile of $M(2\tau)$ will be dominated by either the Gaussian or the Lorentzian component and can be modelled as a single function rather as a product of two functions. Other systems, such as a cuprate superconductor in the so-called "mixed state" (see chapter 6), will have both an exponential and a Gaussian contribution present in $M(2\tau)$.

3.2.5. Measuring T_1

The methods of measuring the spin-lattice relaxation time, T_1, fall into two categories, full recovery pulse sequences and progressive saturation techniques. We will begin with the former.

3.2.5.1. Full-recovery T_1 measurements. There are two main pulse sequences that fall into the full-recovery measurement category, the *inversion recovery* and the *saturation recovery*. Both the inversion recovery and the saturation recovery make use of the same key idea; one begins with a preparation pulse, either a π pulse or a $\pi/2$ pulse, and at a time $t = \tau_1$ later perform a measurement pulse sequence, either a Hahn echo with pulse spacing τ or an FID[3]. In these experiments the value of τ_1 is varied while τ remains fixed and the magnetization amplitude is recorded as a function of τ_1. Figure 3.9 shows a visual representation of these two pulse sequences as a function of elapsed time.

[3]These are not the only options for measurement pulse sequences but they are the only two which we have used for the experiments which we discuss in this dissertation.

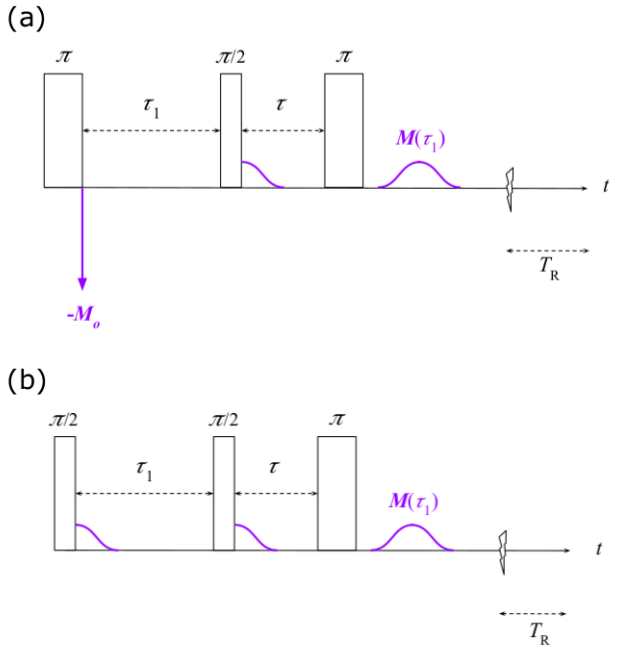

Figure 3.9. A cartoon representation of the full recovery sequences. The inversion recovery is shown in the top figure (a) and the saturation recovery sequence is shown in the bottom figure (b). Each sequence is repeated with a repitition time of $t = T_R$ between each to allow the magnetization to return to equilibrium between each measurement.

In an inversion recovery experiment the above process is conducted with a π preparation pulse that rotates the initial magnetization by 180° such that the initial condition for the magnetization becomes (assuming the magnitude of $\boldsymbol{M}$ is M_o when aligned with $\boldsymbol{H}_o$) $M(t = 0) = -M_o$. As we increase τ_1 the magnetization will go through zero and at sufficiently long τ_1 the signal amplitude will be identical to that of a regular Hahn echo. One advantage of the inversion recovery sequence is that it has a range of magnetization that is $2M_o$ as opposed to M_o.

The saturation recovery begins with a preparatory $\pi/2$ pulse such that at the shortest τ_1 there will be no detectable signal because the initial condition (the magnetization at the time of the initial $\pi/2$ measurement pulse) is $M(t = 0) = 0$. One of the benefits of using the saturation recovery rather than the inversion recovery is that the preparation pulse in a saturation recovery is half as long which means that the frequency range in the power spectrum, the range of frequencies that can be excited by the pulse, is twice as wide [36]. Additionally, the repetition time needed for a saturation recovery is much shorter than that needed for an inversion recovery because the time needed for the system to reach its equilibrium spin population following a measurement sequence will be shorter if the preparation pulse is half as long.

As we alluded to in 2.4.1, when we perform a T_1 measurement we are measuring the magnetization recovery, $M_j(t = \tau_1)$, corresponding to the transition j which we excite with our rf pulse. To extract T_1 we fit our recovery profiles to a sum of exponentials. For a full recovery experiment we fit the magnetization data to the following,

$$M_j(\tau_1) = C_1\big[1 - C_2\big(n_j(\tau_1)/n_o\big)\big], \tag{3.2}$$

where C_1 and C_2 are constants that reflect the spin population and the tip angle of the rf pulse, respectively. Our full recovery profiles -the $n_j(t)$ in (3.2)- can be found in Appendix A of Reference [2] along with the saturation recovery profiles, which will have a different form due to the fact that their initial conditions, and hence the $\boldsymbol{n}(0)$ in (2.30), will differ as we discuss below. We include these recovery profiles in Appendix A for easy reference.

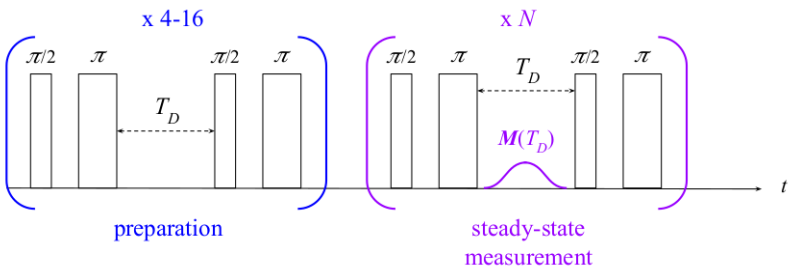

Figure 3.10. A cartoon representation of the PST pulse sequence. In this case, the preparation pulse and measurement pulse sequences are Hahn echoes; however, one could use other sequences such as the FID or a $\pi/2 - \tau - \pi/2$ pulse as well.

3.2.5.2. Progressive Saturation T_1 measurements. In a full-recovery measurement one waits for the spin populations to reach equilibrium before repeating the preparation and measurement sequences. This requires waiting for repetition times, $T_R \gg T_1$, between each sequence. When T_1 is less than 1 second the full recovery method is the best way to get an accurate measurement of the relaxation time; however, when T_1 is longer than 1 s, as is often the case in superconducting systems at low temperatures, the full recovery measurements can become impractically time consuming. Therefore, for sufficiently long T_1 it can be preferable to use a so-called *progressive saturation technique* (PST) to measure spin-lattice relaxation.

The key difference between the full recovery method and PST is that in a PST experiment the initial conditions of the spin system are non-equilibrium and generally not known. The initial preparation sequence in PST is a train of 4-16 Hahn echoes or FIDs separated by a delay time, T_D. This preparation sequence will prepare the system in a non-equilibrium steady state which is then measured by a sequence of N Hahn echoes or FIDs also separated by T_D (see Fig. 3.10). The signal after each measurement sequence

is recorded and averaged with the others such that each T_D value produces one signal (unlike in a CPMG where the measurement appears as a train of echoes). This process is repeated for many T_D values. The longest delay time should be set to no more than 0.5-0.7 T_1 to avoid the experiment becoming too time-consuming. For a detailed overview of PST and its uses for $I > 1/2$ systems see Chapter 4 of reference [2].

The relaxation data that we present in later chapters were measured using the Hahn echo method for T_2 in all nuclei. Our T_1 measurements on the ^{63}Cu nuclei are performed using inversion or satuarion recovery at all temperatures because the relaxation at this site occurs very rapidly even at low temperatures ($T_1 \sim 1$ ms at $T = 20$ K). The ^{17}O T_1 measurements, on the other hand, are preformed using a full recovery sequence at temperatures above the superconducting transition and PST at the lowest temperatures where $T_1 > 1$ s. The fit function for a PST experiment is,

$$M_j(T_D) = C_1\left[1 + 2\sqrt{A(1-A)}\left(n_j(T_D)/n_o\right)\right], \tag{3.3}$$

where C_1 and A are constants which we leave as fit parameters.

Although all the pulse sequences we have presented above show the signal in the time domain, all of our analysis is carried out in the frequency domain. We use either MATLAB or MAGRes to transform our time-domain data into frequency data using a discrete Fourier transform (FT). When fitting the magnetization decay to find T_1 or T_2 we use the area under the appropriate peak in the frequency domain to represent $M_j(t)$, which

is given by (3.1) for T_2 and by (3.2) and (3.3) for full-recovery and PST, respectively, for T_1.

3.3. Conclusions

In this chapter we presented an overview of the equipment used in the NMR experiments of interest to us here. We have also seen how one can program a NMR spectrometer to measure the nuclear relaxation times T_1 and T_2. This overview will help the reader understand the results we present in later chapters. In the next chapter we begin discussing the materials of interest and how our samples are fabricated and characterized.

CHAPTER 4

Samples and characterization

As we mentioned in the introduction, the cuprate high-temperature superconductors (HTSCs) were initially discovered in the mid 1980s in La-[23, 24] and Y-[25] based samples. This initial breakthrough quickly led researchers to discover high-T_c superconductivity in similar ceramic materials such as $Bi_2Sr_2Ca_{n-1}Cu_nO_{2n+4+x}$ (BSCCO) [26], $Tl_mBa2Ca_{n-1}Cu_nO_{2n+m+2}$ (TBCCO) [27] and $HgBa_2Ca_{n-1}Cu_nO_{2n+2+\delta}$ (HBCCO) [28]. Despite the fact that certain cuprate samples have been readily obtained and investigated for nearly four decades the scientific community has not yet found a theory that accurately describes the many unusual electronic and magnetic properties of these materials with the success that the BCS theory had with conventional superconductors (SCs). Nonetheless, decades of experimentation has left us with an abundance of phenomenological properties that arise in these highly anisotropic layered compounds.

In this chapter we will look at some of the phenomenological properties that make the cuprates so elusive. In the later sections we will present the reader with the characterization of our underdoped, single-crystal cuprate samples. We also discuss our isotope exchange and annealing procedure which is essential for performing ^{17}O NMR.

4.1. Cuprates

The materials we refer to as "cuprates" are ceramic structures with non-stoichiometric components (e.g. excess oxygen or strontium atoms). The parent compounds of these systems are antiferromagnetically ordered Mott insulators, materials with partially filled conduction bands that do not conduct due to on-site Coulomb repulsion between electrons [52, 53]. In order to discuss how the physical properties of the cuprates can be altered from this Mott insulating ground state we will first look at the structural features that define this class of materials.

4.1.1. Structures and phases

The unit cell of a cuprate contains one or more planar, or near planar CuO_2, layers separated by planes of non-conducting atoms. These CuO_2 layers are the defining structural feature of the cuprates and host the wide selection of electronic phases discussed here. Some of the non-conducting layers provide the CuO_2 plane with charge carriers [54] which aid in conductivity, however, in order for the parent compounds to become conducting and superconducting one must provide additional charge carriers to the CuO_2 plane via hole or electron doping. As the dopant concentration, and consequenty the carrier density, increases the charge carriers in the CuO_2 plane become itinerant which leads to conductivity and superconductivity in the CuO_2 layer. The fact that superconductivity occurs in just one plane makes these systems highly anisotropic and gives them properties that closely resemble those of two-dimensional SCs [29]. The cuprates discussed herein are hole-doped with oxygen being the dopant. We denote the oxygen dopant concentration as δ, which is approximately equivalent to the hole concentration in our systems. Fig. 4.1

shows the unit cell of the ubiquitous YBCO (Y123) and the less studied Hg1201.

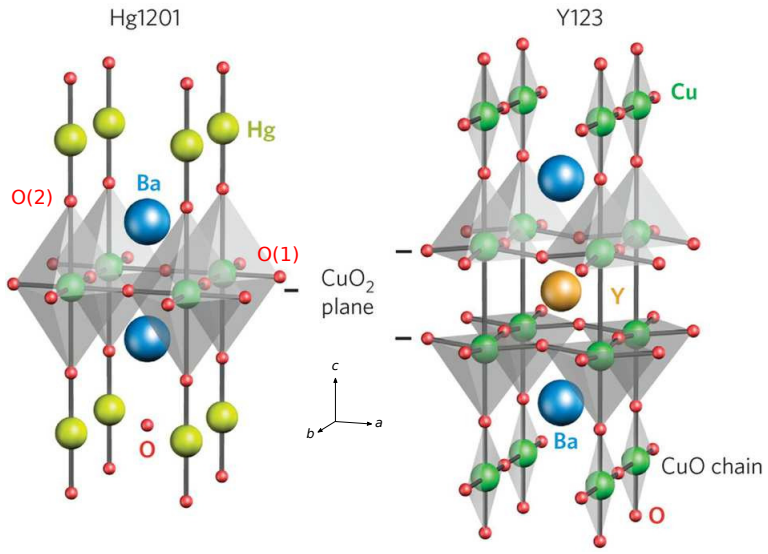

Figure 4.1. The above figure, taken from reference [5], shows the crystal structure of $HgBa_2CuO_{4+\delta}$ (Hg1201, left) and $YBa_2Cu_3O_7$ (YBCO, right). The two stoichiometric oxygen sites in Hg1201 are the planar, O(1), and apical, O(2), sites which are labeled accordingly. The dopant oxygen atom (labeled as O) in Hg1201 lies in the midpoint of the Hg plane. The crystal a, b and c axes and CuO_2 plane are also indicated.

In addition to superconductivity, the cuprates have a plethora of electronic phases which can be tuned with doping as can be seen in the temperature vs. hole doping (T-δ) phase diagram. The phase diagram for the cuprate $HgBa_2CuO_{4+\delta}$ is shown in Fig. 4.2. Although each material will have slightly different temperature boundaries for the various phases, the general form of this phase diagram is common to all hole-doped cuprates. At low δ the cuprates remain in the anti-ferromagnetic (AFM) Mott insulating phase. Upon further addition of holes the system begins to form a superconducting "dome" bounded by T_c. This dome has its maximum at a so-called "optimal" doping

concentration, δ_{op}, where the system has the highest T_c. Our research has focused mainly on the superconducting region of the phase diagram, but we describe the other phases briefly below for completeness.

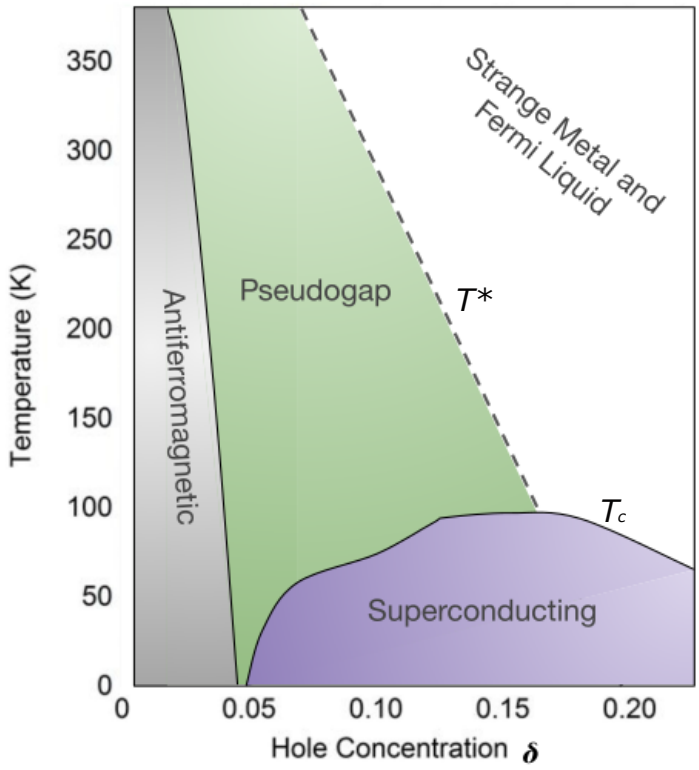

Figure 4.2. The T vs. δ phase diagram for Hg1201 adapted from reference [6]. The pseudogap temperature, T^*, is shown as a dashed line and the superconducting dome lies below the transition temperature, T_c.

For $\delta \leq \delta_{op}$ and $T > T_c$ the system exibits the so-called *pseudogap* (PG) phase. This is characterized by the opening of an energy gap below a temperature, T^*, where $T^* > T_c$. In NMR the PG manifests as a drop in the Knight shift as well as in $(T_1T)^{-1}$, both of which are also manifestations of the opening of the superconducting energy gap. The PG

phase was initially discovered through NQR and NMR measurements of ^{63,65}Cu and ^{89}Y, respectively, in underdoped $YBa_2Cu_3O_{7-\delta}$ samples [55, 56]. The existence of a PG has also been confirmed by other experimental methods, e.g. angle-resolved photoemission spectroscopy (ARPES) [57]. Although the PG phase has been thoroughly experimentally verified its origin and relation to superconductivity remains an open question.

At higher temperatures and doping the cuprates exhibit various conducting phases including a so-called "strange metal" phase and Fermi-liquid behavior. These phases are not relevant to the research presented in this dissertation and therefore we will not discuss them in depth here. The interested reader can see reference [6] and the literature cited therein for details on studies of the Fermi-liquid behavior of $YBa_2Cu_3O_{7-\delta}$ and $HgBa_2CuO_{4+\delta}$ over a wide range of doping.

4.2. $HgBa_2CuO_{4+\delta}$

The compound $HgBa_2CuO_{4+\delta}$ (Hg1201) has the simplest structure of any of the cuprates. Its unit cell contains one CuO_2 plane and has a simple tetragonal crystal structure free from buckling and distortion. At optimal doping Hg1201 has the highest T_c ($\approx$ 97 K) of any of the single-layer cuprates [6]. The Hg1201 unit cell contains two inequivalent stoichiometric oxygen sites, the planar oxygen, O(1), and the apical oxygen, O(2), which are labeled in Fig 4.1. The non-stoichiometric dopant oxygen, O_δ, lies in the middle of the four Hg atoms. This is relatively far from the superconducting CuO_2 plane

meaning that in underdoped samples the O_δ site does not provide a high density of pinning centers for vortices in the mixed state [58].

The simple structure of Hg1201 makes it an ideal candidate for NMR because it yields a relatively simple NMR spectrum. The NMR active nuclei which we study are ^{199}Hg ($^{199}I = 1/2$), ^{63,65}Cu ($^{63,65}I = 3/2$) and ^{17}O ($^{17}I = 5/2$). When the external field is parallel to the crystal c-axis (see Fig. 4.1 for axis labels) the system contains only two inequivalent oxygen sites and only one copper and one mercury site. This in contrast to, e.g. YBCO which has four inequivalent oxygen sites and two copper sites each of which must be distinguished in order to perform reliable measurements. The greater the number of inequivalent stoichiometric sites of a particular nucleus, the more likely it is that there will be overlap in the NMR spectrum. When overlap occurs it can be difficult to separate the contributions between the two sites which results in greater margins of error when extracting physical properties such as Knight shift an relaxation rates.

In Hg1201 the ^{17}O frequency spectrum is well separated with the exception of the central $m = (\pm 1/2 \leftrightarrow \mp 1/2)$ transtion, which begins to overlap at low temperatures due to the difference in the temperature dependence of $K(T)$ between the two sites. Namely, the O(1) shifts to lower frequencies while the O(2) peak does not have an appreciable frequency shift above T_c. Each ^{17}O site has $2I = 5$ transitions because ^{17}O is a spin-5/2 nucleus and the EFG is non-zero. The O(2) site in particular is attractive for studying local fields because it's coupling to the hyperfine field of the CuO_2 plane is negligible, as has been shown by hyperfine field analysis using the Knight shift [4]. This negligible

hyperfine coupling is the reason for the negligible frequency shift of the O(2) central transition with temperature. Even at $T < T_c$ the O(2) central transition does not shift appreciably in frequency because the main contribution to it's Knight shift, $K^{O(2)}$, is the diamagnetic component, which is small compared to the hyperfine contributions.

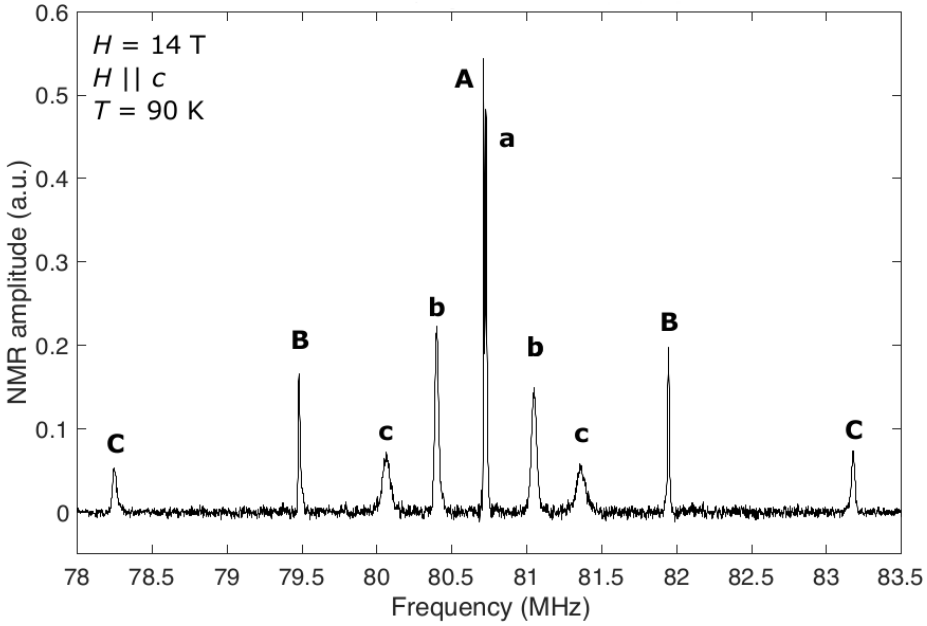

Figure 4.3. A NMR frequency-domain spectrum of a single crystal Hg1201 sample in $H_o = 14$ T with $\boldsymbol{H}_o \parallel \boldsymbol{c}$ at $T = 90$ K. The upercase labels indicate the peaks corresponding to the O(2) sites and the lowercase labels correspond to the O(1). The corresponding transitions are $(-1/2 \leftrightarrow +1/2)$ for $\mathbf{A}/\mathbf{a}$, $(\pm 3/2 \leftrightarrow \pm 1/2)$ for $\mathbf{B}/\mathbf{b}$ and $(\pm 5/2 \leftrightarrow \pm 3/2)$ for $\mathbf{C}/\mathbf{c}$.

Figure 4.3 shows the Hg1201 ^{17}O spectrum at a temperature of 90 K, which is above this sample's critical temperature of 81 K. The letters above each peak denote whether the peak corresponds to the O(2) (uppercase) or the O(1) (lowercase) site. Notice that, while the O(1) and O(2) peaks overlap at the central transition the quadrupolar satellites are well isolated in frequency. This allows us to accurately measure $M_j(t)$, where j indexes

the transition, as discussed in the previous two chapters. This results in reliable T_1 and T_2 values which will be the topic of discussion in the following two chapters.

We also use NMR for characterization. Specifically, we use ^{199}Hg NMR to characterize the sample dopant concentration. This method agrees well with the results of iodometric titration [59] for underdoped samples, which is appropriate for the materials we have studied. Below we describe our sample preparation and characterization procedures in detail.

4.2.1. Sample characterization and isotope exchange

Our single-crystal Hg1201 samples were synthesized by M. Chan at Los Alamos National Laboratory and by M. Greven *et al.* at the University of Minnesota by methods previously described in reference [60]. The doping concentration, δ, of the as-grown samples was initially characterized through ^{199}Hg NMR with $\boldsymbol{H}_o$ parallel to the crystal c-axis. The superconducting transition temperature, T_c, was identified through a magnetization, M, versus temperature, T, measurement performed with a SQUID magnetometer at Northwestern University (NU). The crystal c-axis was identified using Laue x-ray diffraction (XRD). We will explain each characterization step and results in detail in the later subsections. A table of the three samples which we present data on in this work is shown below in table 4.2.1.

In order to perform NMR at the oxygen sites we must use an isotope exchange method to replace some of the spin-zero ^{16}O in the as-grown samples with the spin-5/2 ^{17}O isotope.

Sample	T_c (K)	ΔT_c (K)	**Source**	**Ref.**	**mass** (mg)
UD81	81	4	Stolt	This work	20
UD79	79	1.5	Lee	[4, 58]	13.6
UD74	74	4.5	Mounce	[3]	20

Table 4.1. A table of the samples references in this work.

This process is described in the next subsection as well as in Chapter 4 of References [3, 4] and in Reference [7]. The characterization steps mentioned in the previous paragraph were repeated following each isotope exchange.

4.2.1.1. Oxygen isotope exchange and annealing procedure. The ^{17}O isotope has a natural abundance of less than 0.04 % [61]. Therefore, in order to obtain a reasonable signal-to-noise ratio in our ^{17}O NMR experiments we must anneal the as-grown Hg1201 samples in a ^{17}O rich environment for several days to several weeks in order to increase the concentration of O_δ of this isotope and distribute the dopant uniformly. Fig. 4.4 is a block diagram depicting the setup of the oxygen isotope exchange system used at NU.

The general procedure for performing our isotope exchange and annealing is as follows. The first step is to place the Hg1201 sample in a quartz crucible, which has the shape of a boat with a bottom curvature that matches that of the quartz tube that houses the sample during the process. Once the sample(s) is inside the quartz tube the crucible is locked in by two quartz filler tubes to minimize the dead space. This area is illustrated in Fig. 4.4 as the region labeled "sample space." The quartz tube sits inside a furnace and is sealed at both ends. We use a turbomolecular pump to evacuate the sample space until the pressure is $\leq 10^{-5}$ mbar and the leak rate of the entire system shown in Fig. 4.4

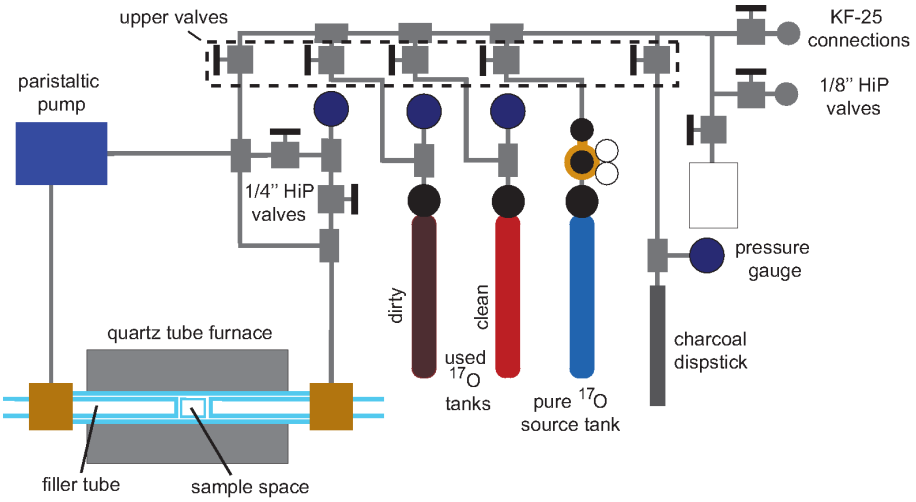

Figure 4.4. Block diagram depicting the gas exchange system used for isotope exchange. The figure was adapted from [3] in reference [7] to account for changes made to the setup. The pumping station used to evacuate the system in the initial step is connected to the upper KF-25 connection at the top right. The blank box in the top right corner can be used for a high-pressure extension which is described in [7].

is $\leq 10^{-9}$ Torr·L/sec.

Once the system has been thoroughly pumped out to avoid contamination by other gas molecules the gas exchange procedure can begin. The flow of gas into and out of the quartz tube is regulated using a charcoal dipstick. Additionally, all components are isolated from the others via high pressure valves and 1/4 inch stainless steel (ss) piping with swagelock connections from High Pressure Eqiupment Co. (HiP) [7].

To begin the isotope exchange we close off the pumping port and close the valves connecting the pump to the quartz tube section. We then open one of the gas cylinders (often the one labeled "pure ^{17}O source tank") until the gauge at this valve displays our

desired pressure. Once the desired pressure is reached we close the source tank[1]. In order to absorb the pure ^{17}O gas into the dipstick we place the dipstick in a vat of liquid nitrogen to decrease the dipstick pressure; once the pressure had stabilized we open the valve connecting the gas from the source tank (which is now closed) to the dipstick. Once the pressure at the dipstick is stable we close the valves between the source tank and the dipstick. In order to release the ^{17}O gas into the sample space we remove the vat of nitrogen and heat up the dipstick with a heat gun allowing the gas to fill the ss capillary tube that connects to all the system components. Once the dipstick pressure is stable or once the desired pressure is reached we close the dipstick valve and open the upper ss tube to the sample space until the sample space pressure equilibrates. If the pressure in the sample space is lower than desired we close the sample space valve and repeat the process of transferring ^{17}O gas from the source tank to the sample space until the desired pressure (< 1 bar) is reached.

One the system is at the correct pressure we close off the sample space and turn the furnace on to begin annealing the sample in the ^{17}O rich environment. During the annealing process we use a peristaltic pump to circulate the oxygen gas inside the quartz tube. The annealing temperatures range from 350°C to 550°C and typical annealing times range from 12-24 hours to several (up to three) weeks. The two samples which we have studied are both underdoped single crystals of Hg1202 with T_c values of about 81 K and 79 K; the latter sample has been thoroughly studied in Refs. [4, 58] by Lee *et al.* whereas the former has not previously been studied. We refer to these samples as UD81 (20 mg) and

[1]Never open the source tank directly to the dipstick or any other component of the system.

UD79 (13.1 mg), respectively, according to their doping levels and T_c. The UD81 sample was annealed twice for three weeks at a time in a quartz tube at a partial pressure of $\approx$ 0.5 atm ^{17}O gas at a temperature of 400° C. The UD79 sample was annealed for exactly one week at a ^{17}O partial pressure of 0.7 atm at a temperature of 550° C. For a table of annealing temperatures and times and resulting T_c and ΔT_c values see the tables in Chapter 4 of [3] (Bi2212) and [4] (Hg1201).

The final step of the exchange/annealing process is to quench cool the sample space and to store the gas mixture in the quartz tube in the cylinder labeled "dirty" in Fig. 4.4 for future use. The quench cooling step involves abruptly removing the sample space from the heat of the furnace by opening the furnace (the quartz tube is still sealed off from the atmosphere) and blasting the tube with room temperature air. Once the sample space is sufficiently cool we use the dipstick to absorb the gas mixture in the quartz tube and transfer it to the brown cylinder before opening the sample space to atmosphere and removing the sample.

4.2.1.2. Magnetization vs Temperature. Upon receiving the single crystals our first step is to determine the as-grown sample T_c using a M vs. T measurement. This is performed in a SQUID magnetometer. The T_c is characterized by the onset of diamagnetism by fitting the linear portion of the $M-T$ slope at the transition and extrapolating this slope to meet the flat, $M \approx 0$ portion of the curve. This measurement is also done following any annealing step, as the annealing may change the dopant distribution and

concentration and therefore T_c.

All $M-T$ measurements are performed with a field of $H = 10$ - 20 Oe with $H \parallel c$. The measurements reported here are performed with zero field cooling (ZFC), which means that no field is applied to the sample as it is cooled to the lowest temperature (5 K). The field, H, is then turned on and the sample is slowly heated in temperature steps of 0.5 - 2 K/min (with higher resolution in the 70 K $\leq T \leq$ 100 K where we expect to see T_c) as the magnetization is recorded until the system reaches 300 K.

The ZFC method produces a larger magnetization signal than the field cooled (FC) method, where the sample is initially cooled in the presence of an applied field and subsequently warmed to room temperature as M is recorded. In type II SCs (e.g. the cuprates) the FC method leads to flux pinning which reduces the magnetization signal by trapping magnetic flux that opposes the diamagnetism [62].

The normalized magnetization of the Hg1201 samples is shown in Fig. 4.5. The width of the transitions, ΔT_c, is relatively narrow, around 4 K (UD81) and $\leq$ 2 K (UD79). A narrow transition indicates that the dopant oxygen is spread uniformly through the Hg plane creating a relatively homogeneous local field distribution. Additionally, the constant near-zero slope at $T > T_c$ is a good indicator that the sample does not contain any magnetic impurities that might complicate the interpretation of our NMR spectra.

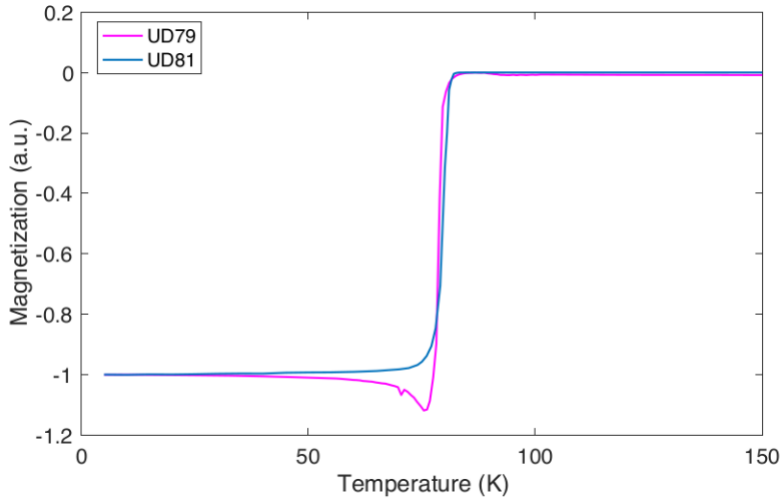

Figure 4.5. Magnetization (normalized) of our under-doped Hg1201 crystals. Measurements were taken with the field parallel to the crystal c-axis. The applied field strength is 10 Oe. The majority of our measurements reported herein were on the UD81 sample.

4.2.1.3. Hg NMR. The presence and location of the dopant oxygen in the Hg plane has been confirmed by neutron scattering experiments [63, 64]; this oxygen, O_δ, alters the electromagnetic environment at the adjacent Hg sites. Therefore, the ^{199}Hg spectrum of a Hg1201 sample will have multiple distinct peaks at different frequencies corresponding to the distinct electromagnetic environments that exist at the various Hg sites. The different peak frequencies correspond to Hg sites with a certain number of nearest neighbor O_δ atoms.

The magnitude of the area under each peak in the ^{199}Hg NMR spectrum corresponds to the number of Hg atoms with n nearest neighbor O_δ atoms. If one considers each peak to be a Gaussian and normalizes the sum of the areas of all peaks, each area can be thought of as the probability of any Hg site in the sample having n nearest neighbor O_δ

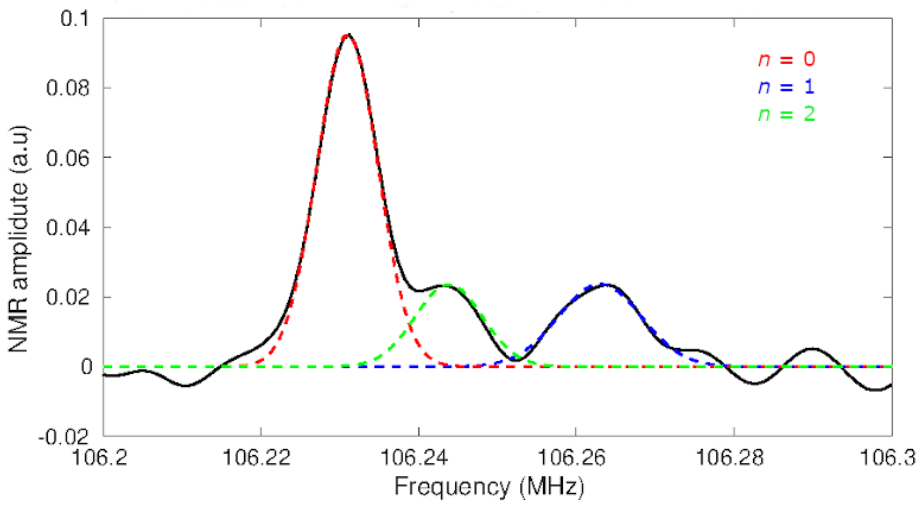

Figure 4.6. ^{199}Hg NMR spectrum for UD81 at 285 K (black line) the red, blue, and green dashed lines are Gaussian fits corresponding to the $n = 0, 1$ and 2 nearest neighbor O_δ atoms, respectively.

atoms. In Reference [7] we report that the spectral weights of the ^{199}Hg NMR spectra of many different single crystal samples of Hg1201 can be modeled as a binomial distribution in the dopant concentration, δ, as follows,

$$P_{n,k=4}(\delta) = \frac{4!}{n!(4-n)!}\delta^n(1-\delta)^{4-n}. \tag{4.1}$$

Here, $P_{n,k}(\delta)$ is the spectral weight under each peak normalized by the sum such that $\sum_{n=1}^{n=4} P_{n,k}(\delta) = 1$, n is the number of near neighbor O_δ atoms and $k = 4$ is the largest possible n value corresponding to a ^{199}Hg surrounded by four O_δ atoms. Fig. 3 from reference [7] (included below) shows the fit results for several Hg1201 samples (measured at NU) as well as fits to data on powder samples of Hg1223 from Stern *et al.* [8]. The fit appears to be the best for under-doped samples and deviates more from the binomial

model as δ increases.

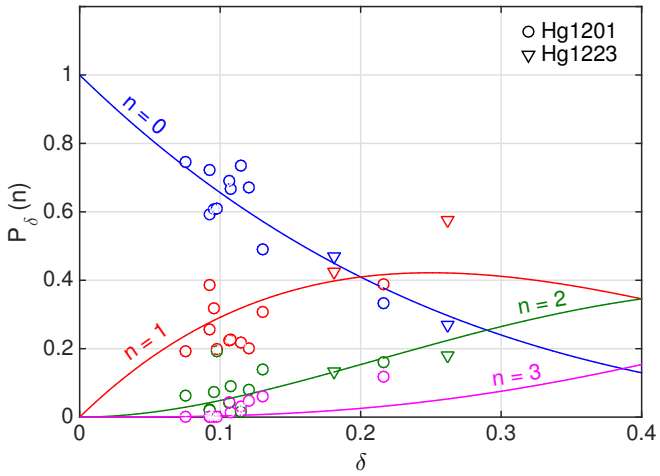

Figure 4.7. Fig. 3 from reference [7] shows the spectral weights of each peak in a collection of ^{199}Hg spectra (open circles) plotted as a function of doping. The peaks are matched with corresponding probability distributions of different Hg environments calculated from Eq. (4.1) (solid lines). Results from a similar analysis on powder samples of Hg1223 (inverted triangles) from Stern *et al.* [8] are also included.

From the ^{199}Hg NMR spectrum (Figure 4.6) we can conclude that the UD81 sample is under-doped from the large spectral weight of the lowest frequency peak, which corresponds to $n = 0$ nearest neighbor O_δ atoms. Additionally, we can use the transition temperature of ≈ 81 K found in our magnetization measurements (Figure 4.5) to check that our binomial fit agrees with the phase diagram. If we draw a horizontal line on the Hg1201 phase diagram (Figure 4.2) from $T = 81$ K we see that the line meets the superconducting dome on the under-doped side at a point corresponding to hole concentration, $\delta \approx 0.11$. This is in good agreement with the δ value of 0.112 found using the binomial

distribution model.

4.2.1.4. Laue XRD. In order to align the sample c-axis with the external field we must be sure of the crystal c-axis location. To do this we use Laue x-ray diffraction (XRD) with a diffractometer at the J. B. Cohen x-ray facility at NU. Fig. 4.8 shows the XRD

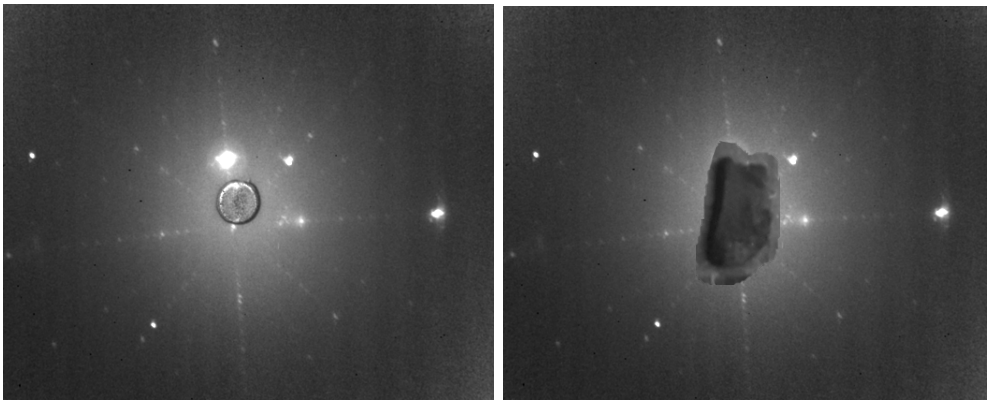

Figure 4.8. A Laue XRD image of the UD81 sample (left) and the same diffraction pattern with the corresponding image of the sample superposed on top of it (right).

image of the [001] surface of the UD81 sample with an image of the sample overlayed to show the correspondence to real-space. This shows that the crystal c-axis can easily be identified because it is perpendicular to the relatively large flat sample surface. The diffracted image was measured using an incident beam acceleration potential of 25 kV and a 10 mA current. The exposure time was 15 minutes.

4.3. Conclusions

The cuprates are a class of high-T_c SCs with an abundance of unique electronic phases which can be tuned by varying the doping concentration. The Hg-based cuprate Hg1201 is a promising candidate for NMR experiments due to its simple structure which yields

a straightforward NMR spectrum. We have characterized two under-doped samples of Hg1201. The flat magnetization at high temperatures as well as the narrow ΔT_c indicate that these samples do not contain appreciable defects and that the distribution of dopant oxygens in the Hg-plane is reasonably homogeneous. Additionally, we have seen how ^{199}Hg NMR can be used to characterize the dopant concentration in Hg1201 single crystals by comparing the distribution of spectral weights the binomial distribution model.

CHAPTER 5

NMR in the CuO_2 plane in Hg1201

We previously noted that superconductivity in the cuprates occurs in the CuO_2 plane. It is therefore not surprising that we are interested in the NMR spectra of the planar Cu and O sites. Here we discuss some of the history of ^{17}O and $^{63,65}Cu$ NMR/NQR in other cuprates and the theories arising from it before presenting our own measurements. Although our compounds of interest are Hg1201 single crystals, we will frequently compare our results to those of YBCO because the NMR data on Hg1201 is still scarce due to lack of sample availability. Since we will be discussing YBCO NMR/NQR results and theories we will begin this chapter with a brief overview of this compound and its notable magnetic properties. We will then describe the often quoted Mila-Rice-Shastry (MRS) model to illustrate the coupling between nuclei in the spin system through the Cu^{2+} spin susceptibility.

5.1. NMR studies of YBCO

One of most ubiquitous cuprates in the study of solid-state NMR is $YBa_2Cu_3O_{7-\delta}$ (YBCO). The predominance of this compound stems from the fact that it was one of the first cuprates to be identified and structurally refined [25] following the initial discovery of HTSCs. High quality YBCO samples could be synthesized and characterized relatively easily making them readily available for NMR studies early on and to this day.

The ease of synthesis along with a rapid development of alignment methods for improved signal acquisition led experimenters to quickly produce large quantities of data for YBCO which required theoretical explanation. Specifically, once they were able to measure NMR/NQR spectra with the field along a specific axis, researchers were able to observe an anisotropy in the Cu relaxation rate, $^{63}T_1^{-1}$, for the planar Cu site, Cu(2), at temperatures above T_c. Additionally, the Knight shift, $^{63}K_c$, measured at Cu(2) along the c-axis showed negligible temperature (T) dependence even at $T < T_c$. On the other hand, the shift, $^{63}K_{ab}$, measured with the field along the ab plane, behaved as expected with Korringa-like behavior above T_c and decaying to zero below T_c. This available data on optimally-doped YBCO raised many questions and inspired many of the early theories for cuprate superconductivity. One of the most famous of these theories is that of Mila Rice and Shastry.

5.2. The Mila-Rice-Shastry Hamiltonian

The NMR/NQR results described above were initially interpreted [65] following the assumption that all hyperfine coupling of the Cu^{2+} spin to mobile dopant holes was localized at the Cu(2) site. However, this theory failed to account for the observed anisotropy in the relaxation rate, $^{63}T_1^{-1}$. Also, the lack of temperature dependence of $^{63}K_c$ indicated that this component of K was an orbital shift rather than a spin shift, meaning that it could not be involved in the formation of electronic spin pairs [22].

In order to resolve these experimental results Mila and Rice used a quantum chemistry interpretation to posit that the total hyperfine spin Hamiltonian for YBCO must contain

at least two hyperfine field terms. In addition to the local, anisotropic hyperfine field, A_α, due to nuclear spin coupling to the Cu^{2+} $3d$ hole spin, Mila and Rice proposed an isotropic transferred hyperfine field, B, which originated from hybridization of the Cu $3d_{x^2-y^2}$ orbitals with unfilled $4s$ orbitals from neighboring Cu atoms. The pair suggested that this hybridization would occur through the $2p$ orbitals on the O sites between each set of nearest neighbor Cu atoms [66].

The Mila-Rice Hamiltonian was later extended by Alloul *et al.* [67] to include the Y^{3+} ions and famously by Shastry [68] to include transferred hyperfine coupling to the planar O sites. The final Hamiltonian, known as the Mila-Rice-Shastry (MRS) Hamiltonian is given by (for YBCO),

$$\hat{\mathcal{H}}_{HF} = \sum_{i,\alpha} \hat{I}^{(1)}_{i\alpha} \left(A^{(1)}_\alpha \hat{S}_{i\alpha} + B^{(1)} \sum_{j(nn)} \hat{S}_{j\alpha} \right) + \sum_{i,\alpha} \hat{I}^{(2)}_{i\alpha} \left(A^{(2)}_\alpha \hat{S}_{i\alpha} + B^{(2)} \sum_{j(nn)} \hat{S}_{j\alpha} \right) + \sum_{i,\alpha} {}^{17}\hat{I}_{i\alpha} \sum_{j(nn)} C_\alpha \hat{S}_{j\alpha} + \sum_{i,\alpha} {}^{89}\hat{I}_{i\alpha} \sum_{j(nn)} D_\alpha \hat{S}_{j\alpha}. \tag{5.1}$$

Here the $A^{(1,2)}_\alpha$ are the local hyperfine fields at the Cu(1)[1] and Cu(2) sites and the $B^{(1,2)}$ are the isotropic transferred hyperfine fields from coupling to the Cu $4s$ orbital at the Cu(1) and Cu(2) site, respectively. Similarly the C_α and D_α are the transferred hyperfine fields that arise from Cu $3d$-orbital hybridization with the $2p$-orbitals of the O neighbors and with the Y^{3+} $4d$ orbitals, respectively. The sum index nn refers to the nearest neighbor Cu(2) atoms, meaning that there are eight terms in the ^{89}Y nn sum, two terms in

[1]The Cu(1) site corresponds to the CuO chain, which is labeled in Fig. 4.1.

the O sum, and four in each Cu sum.

The MRS Hamiltonian was developed for YBCO, which has two inequivalent Cu sites and four inequivalent oxygen sites. The Hamiltonian for Hg1201 is significantly more simple [3],

$$\hat{\mathcal{H}}_{HF} = \sum_{i,\alpha} \hat{I}^{\mathrm{Cu}}_{i\alpha} \left(A^{\mathrm{Cu}}_{\alpha} \hat{S}_{i\alpha} + B \sum_{j(nn)} \hat{S}_{j\alpha} \right) + \sum_{i,\alpha} \sum_{j(nn)} \left({}^{17}\hat{I}^{(1)}_{i\alpha} C^{(1)}_{\alpha} + {}^{17}\hat{I}^{(2)}_{i\alpha} C^{(2)}_{\alpha} \right) \hat{S}_{j\alpha} + \sum_{i,\alpha} {}^{199}\hat{I}_{i\alpha} \sum_{j(nn)} D_{\alpha} \hat{S}_{j\alpha}. \tag{5.2}$$

Here A_α is still the on-site hyperfine field at the Cu site and B is the isotropic transferred hyperfine field as in the YBCO case. The $C^{(1,2)}_\alpha$ and D_α are transferred hyperfine fields at the O(1), O(2) and Hg sites, respectively.

The MRS Hamiltonian is one of the most famous theoretical development in the field of high-T_c superconductivity to come out of NMR/NQR data. One key property of the MRS Hamiltonian is that it treats the entire system of nuclei as if the only susceptibility involved in hyperfine coupling is that of the Cu^{2+} hole spins, whose spin operators are denoted $\hat{S}_{k\alpha}$ $(k = i, j)$ in (5.1) and (5.2). This *one-susceptibility model* has its roots in the Zhang-Rice singlet picture [69] in which all superconducting properties arise from mobile holes forming singlet complexes with the itinerant holes introduced by doping. This assumes that the Cu^{2+} susceptibility accounts for all normal state hyperfine coupling and pair formation in the superconducting state. Other arguments have been made for the

necessity of an additional susceptibility originating from a so-called "oxygen-hole band," as we address below.

5.2.1. The two-susceptibility model

The MRS Hamiltonian marks a substantial breakthrough in the development of the theory of cuprate superconductivity. However, the model has several flaws including the fact that the hyperfine Hamiltonian does not account for changes in the Knight shift that occur upon changing the hole doping concentration [22]. Monien, Pines and Slichter [39] proposed that the Cu NQR data should be accounted for with an additional hyperfine coupling to a susceptibility from the planar oxygen sites. This picture accounts for the doping dependence of the Knight shift and has been utilized for analysis of NMR experiments on Hg1201 [70]. Mila and Rice have argued [71] that (in their quantum chemistry framework) a oxygen hole band would couple more strongly to the Y^{3+} $4d$ orbitals than experimental observations indicate.

Both Mounce [62] and Lee [4] have performed Knight shift analyses for several under-doped single crystal Hg1201 samples in which the groups plotted the spin shift of one nuclear spin to another and found the one-susceptibility model agreed well with their data for all isotope-exchanged samples. This result contradicts those of Haase *et al.* [70] in which the group found the two-component susceptibility necessary for describing the Knight shift in their optimally-doped and under-doped Hg1201 single crystal samples. It is interesting to note that the group led by Lee was able to reproduce Haase *et al.*'s

results, which indicate a need for a second susceptibility component, in their non-isotope-exchanged, optimally-doped single crystal sample. Lee suggested that the discrepancy could indicate the presence of an isotope effect.

Although the MRS picture of cuprate superconductivity has provided theorists and experimenters with excellent starting points for data analysis, the origin of $^{63}T_1^{-1}$ in particular remains an open question [22]. In their original paper, Mila and Rice [66] showed that their model could account for the observed anisotropy in the Cu ${T_1}^{-1}$ by taking the MRS Hamiltonian corresponding to the Cu site of interest to be the perturbation, $\hat{\mathcal{H}}_1(t)$, in (2.31) and showing that the resulting ratio of $^{63}T_{1c}/^{63}T_{1a}$ agreed reasonably well with existing experimental data. However, the MRS Hamiltonian cannot be used to accurately predict absolute values of these relaxation rates.

Other theoretical methods based on the MRS model have been proposed, e.g. by Uldry and Meier [72], to analyze Cu relaxation data more precisely. However, despite decades of theoretical scrutiny and development, the temperature dependence of $^{63}T_1^{-1}$ is still mainly phenomenological. In the next section we show the high-field relaxation data for ^{63}Cu and transverse relaxation data for the in-plane ^{17}O in our two Hg1201 single crystal samples. We will discuss what we can conclude from these measurements and what measurements should be performed in the future to get a more complete picture of the superconducting system.

5.3. ^{63}Cu shift and relaxation

Here we present our ^{63}Cu relaxation data on UD81 as well as that of Lee *et al.* on UD79. All of our measurements were performed at the central ^{63}Cu transition in a field of $H_o = 14$ T with $H_o \parallel c$. Spin-spin relaxation rate measurements were performed using the Hahn echo method with a $\pi/2$ pulse length of around 4 - 5 μs. Spin-lattice relaxation was measured using the saturation recovery method with a Hahn echo detection sequence. A Ag coil was used to avoid contamination from the metallic Cu resonance, however, due

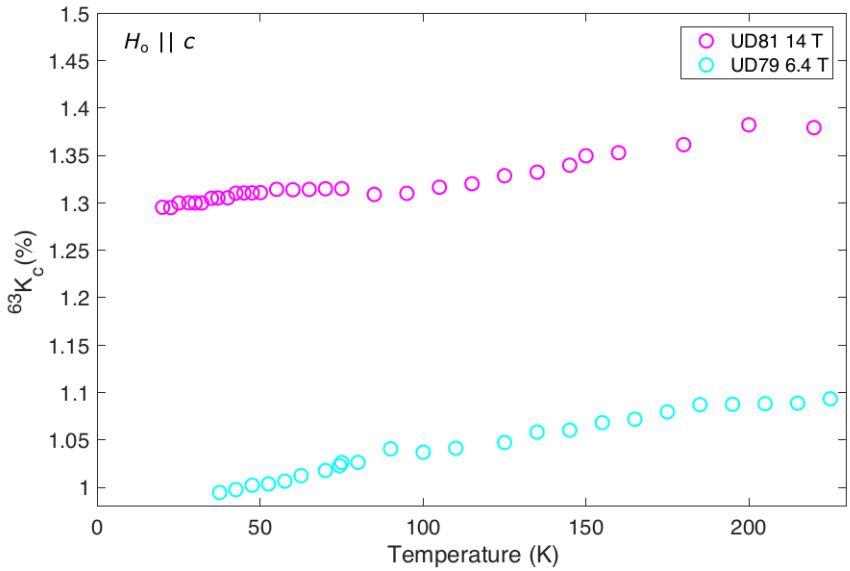

Figure 5.1. The total NMR shift of ^{63}Cu in our UD81 sample at 14 T and in the UD79 sample at 6.4 T with $H_o \parallel c$. The UD79 data was measured by Lee [4]. Note that the shift of metallic Cu is 0.2394 % at room temperature which is over 1 MHz from our peak in the frequency spectrum at a field of 14 T.

to the large shift (1-2 %, see Fig. 5.1) of ^{63}Cu in Hg1201, the resonance from the sample Cu sites were sufficiently far away from metallic Cu ($K_{\mathrm{Cu}} \approx 0.24\%$) in frequency that a

Cu coil could also have been used without added difficulty.

The full NMR shift for $H_o \parallel c$ ($^{63}K_c$) of our two under-doped samples is shown in Fig. 5.1. Note that the shifts were measured at different fields. Both plots show a decrease of K_c with temperature with a change in slope around T_c. This decrease arises from a combination of the orbital diamagnetism shift, K_{dia}, and the spin shift, K_s, as discussed in Chapter 2. The remaining contribution to K_c is the constant orbital shift, K_o, which is large in ^{63}Cu. This is why the $^{63}K_c$ in Fig. 5.1 appear to be decaying towards 1-1.3% rather than to zero at the lowest temperatures.

5.3.1. ^{63}Cu $T_1{}^{-1}$

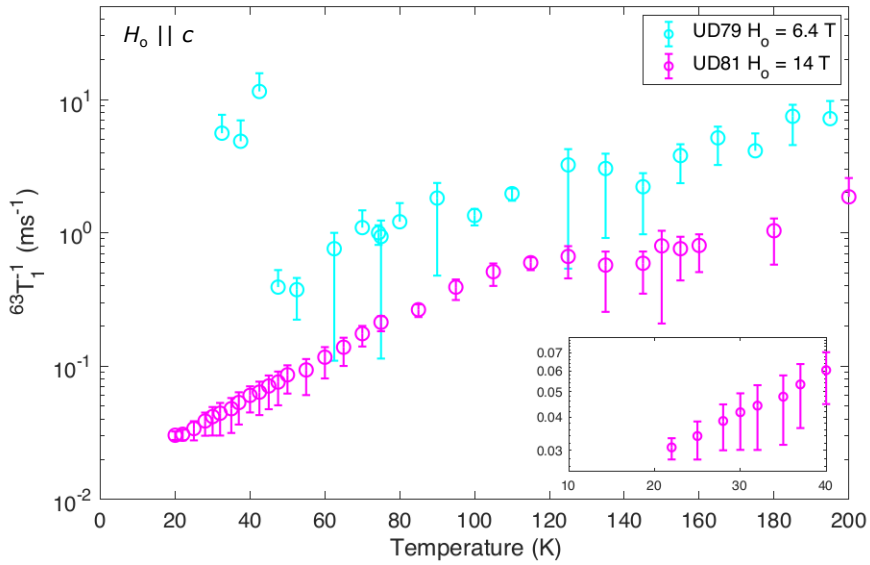

Figure 5.2. The temperature dependence of the $^{63}T_1^{-1}$ for the UD81 and UD79 samples at $H_o = 14$ T and 6.4 T, respectively. The inset shows the low temperature dependence of $^{63}T_1^{-1}$ with the data point at 20 K excluded for reasons discussed in the text.

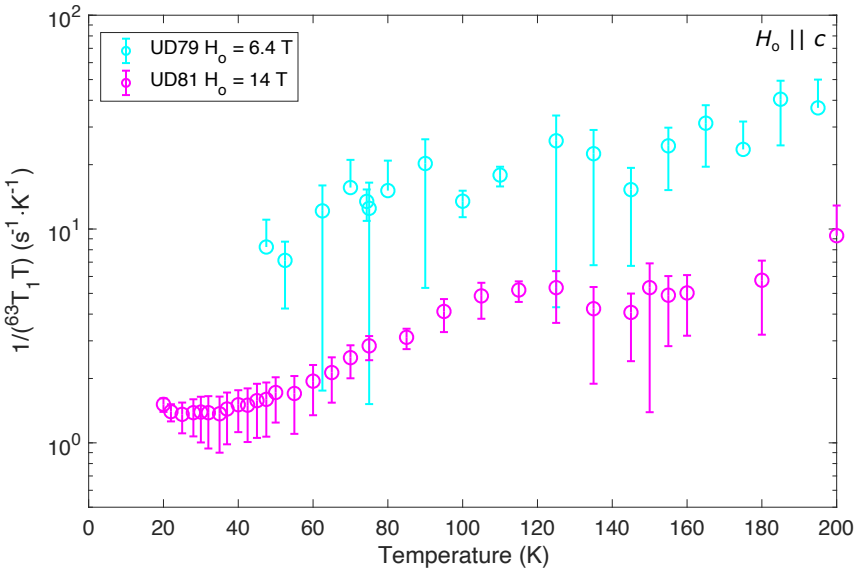

Figure 5.3. The temperature dependence of the UD81 sample $1/(^{63}T_1T)$ at $H_o = 14$ T as well as that of the UD79 sample at 6.4 T. Again, both measurements were performed with H_o parallel to the crystal c-axis. The large error bars at higher temperatures reflect a poor signal-to-noise at temperatures above ≈ 100 K.

Our $^{63}T_1^{-1}$ measurements are shown in Fig. 5.2. The UD79 data was measured by Lee *et al.* and re-analyzed for this dissertation. The inset shows the linear T-dependence of the low temperature $^{63}T_1^{-1}$ in UD81. The 20 K data point is excluded from the inset because this point was measured at a temperature which fluctuates by > 1 K about 20 K due to technical difficulties with the cryostat at $T < 22$ K. The 20 K data point is included in the main plot. An exponential T-dependence in $^{63}T_1^{-1}$ at high fields agrees with the results reported by Martindale *et al.* for YBCO aligned powders, although the authors suggest that this temperature dependence may not be physically meaningful [73].

The $1/(^{63}T_1T)$ behavior of UD81 and UD79 is shown in Fig. 5.3. The peak at $T \approx$ 120 K in the UD81 data is a manifestation of the pseudogap (PG) behavior discussed in Chapter 4. The PG temperature, T^*, for UD79 was found by Lee [4] to be 300 K, which is why the UD79 $1/(^{63}T_1T)$ does not show any appreciable maximum in the temperature range $0 \leq T \leq 200$ K.

Although all of the measurements we report were taken with $H_o \parallel c$, it would be interesting to measure the relaxation rate for $H_o \parallel a, b$ as well to compare the anisotropy ratio, $R \equiv {}^{63}T_{1a}^{-1}/{}^{63}T_{1c}^{-1}$ as a function of temperature. Martindale *et al.* [74, 73, 75] measured R in YBCO aligned powders and showed that it was constant above T_c but below T_c the plot exhibited a sort of "coherence peak" similar to what is seen in the T_1^{-1} vs. T plots for conventional (BCS) SCs. The group used theories proposed by Bulut and Scalapino [76] as well as collaborations with Lu *et al.* [77] to show that their $T < T_c$ data corresponds to a BCS singlet pairing with nodes in the gap energy.

In order to get a sense of what the relaxation anisotropy ratio, R, might look like in Hg1201 we extracted ${}^{63}T_1^{-1}$ data from plots reported by Lee [4] and took the ratio of the ${}^{63}T_{1a}^{-1}$ to ${}^{63}T_{1c}^{-1}$ that were measured at the same temperature. The results are shown in Fig. 5.4 for an under-doped sample with a T_c of 87 K (UD87) and an optimally-doped sample with a T_c of 94 K (OP94) at a field of $H_o = 6.4$ T. Both samples are single crystals with characterization reported in [4].

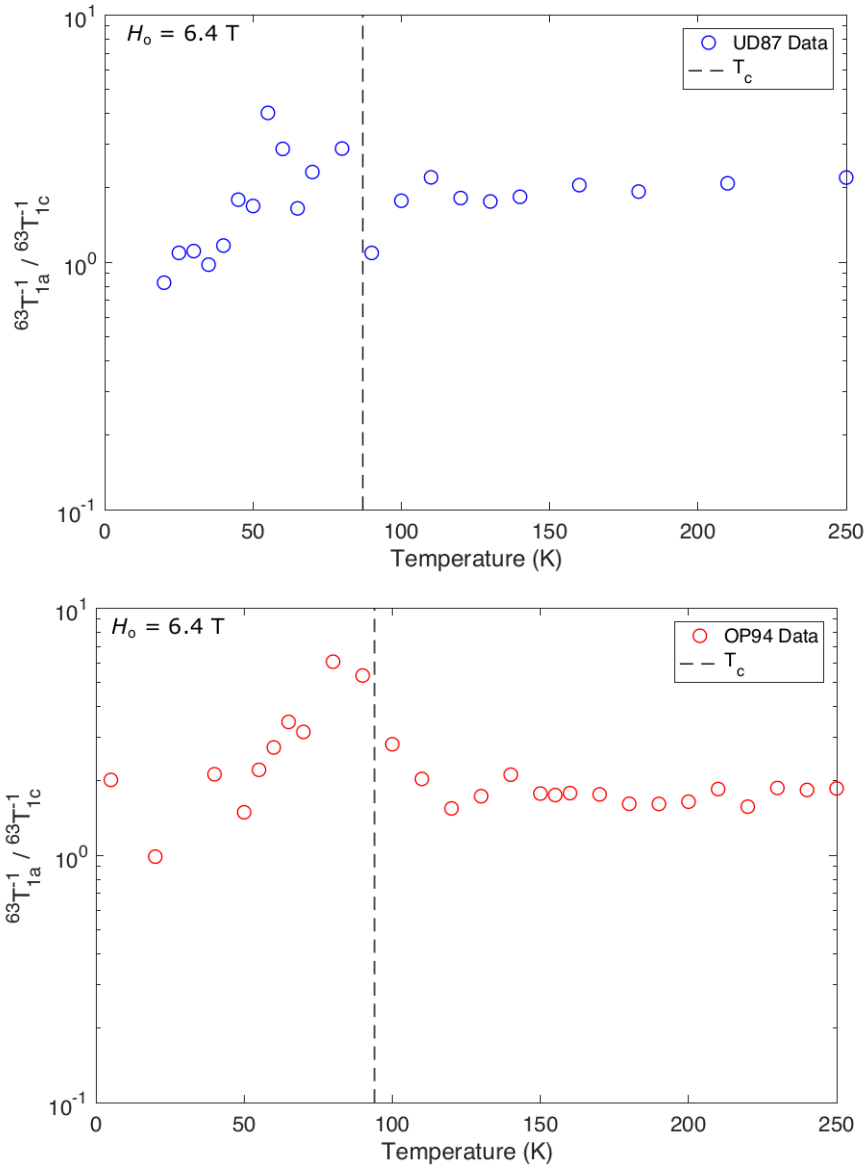

Figure 5.4. A plot of the ratio R (see text) for two single crystal Hg1201 samples. These data were calculated using data points extracted from plots in reference [4]. The dahsed line indicates the location of T_c measured at 10 Oe. The size of the error bars are unknown.

In looking at the plots in Fig. 5.4 we can see that R is constant with a value of $R \approx 1.8$ for OP94 and $R \approx 2.0$ for UD87 at high temperatures. In both cases the anisotropy ratio

begins to deviate from its high-temperature value just above T_c although it is not clear if this deviation is within error bars because these are not included in the plots. It is clear, however, that the anisotropy follows a similar temperature dependence to that reported in YBCO. It should be noted, however, that at high fields ($H_o > H_{c1}$) the $^{63}T_{1c}^{-1}$ is thought to be dominated by vortex cores [74] so one should measure R with NQR in order to extract information about the superconductivity of the system.

5.3.2. ^{63}Cu $T_2{}^{-1}$

The measured ^{63}Cu spin-spin relaxation rates, $^{63}T_2^{-1}$, were extracted from fitting a set of Hahn echo T_2 spectra to the decay function,

$$M(2\tau) = M_o e^{-(2\tau)/T_2},$$

i.e. a single exponential. The magnetization, $M(2\tau)$, is taken to be the value of the area under the NMR spectrum in the frequency domain for the pulse spacing τ. We use a Levenberg-Marquardt non-linear least-squares fit algorithm provided by Matlab for all of our fitting.

Although previous work by Lee [4] reported a combined exponential and Gaussian $M(2\tau)$ dependence in Hg1201 we did not observe any Gaussian decay behavior in our analysis of our own data on UD81. Our re-analysis of Hahn echo T_2 experiments on other single crystal Hg1201 samples also indicated a better fit to a single decay function at all temperatures. Therefore, we have proceeded to use our single exponential function fit to extract all $^{63}T_2^{-1}$ values reported here. We note that Lovellette [48] also reported single

exponential T_2 behavior in his measurements on a YBCO aligned powder.

The rate $^{63}T_2^{-1}$ can be described in terms of its deviation from the rigid lattice limit discussed in 2.4.2.1. The spin-spin relaxation in this limit is given by the expressions for the Van Vleck second moment in the case of like and unlike spin coupling, Eq. (2.37) and (2.38). In calculating $^{63}T_2^{-1}$ in the rigid lattice limit we account for the spin-spin coupling between ^{63}Cu and ^{63}Cu, ^{63}Cu and ^{65}Cu, and ^{63}Cu and ^{17}O. We consider only the nearest neighbor interactions in our sums. We must also include the natural abundances of the ^{63}Cu and ^{65}Cu isotopes which are 69% and 31%, respectively. The measured $^{63}T_2^{-1}$ are shown in Fig. 5.5 along with the rigid lattice limit, which is $T_{2RLL} \approx 0.5$ ms.

From the plot shown in Fig. 5.5 it is clear that the transverse relaxation in ^{63}Cu is dominated by contributions other than nuclear spin-spin coupling at all temperatures. The relaxation rate does decrease with decreasing T below T_c for both samples. However, this decrease is very modest, only slightly outside the range of the 95% confidence intervals (error bars) of our fit. This relatively small T-dependence indicates that the mechanism responsible for the transverse relaxation is not heavily dependent on the electronic spin system; however, to verify this we would need to continue these measurements for $T <$ 20 K.

5.3.3. Redfield

Another comparison that we make is with the Redfield expression. In Chapter 3 we mentioned that the measured T_2 would be influenced by local field distributions and

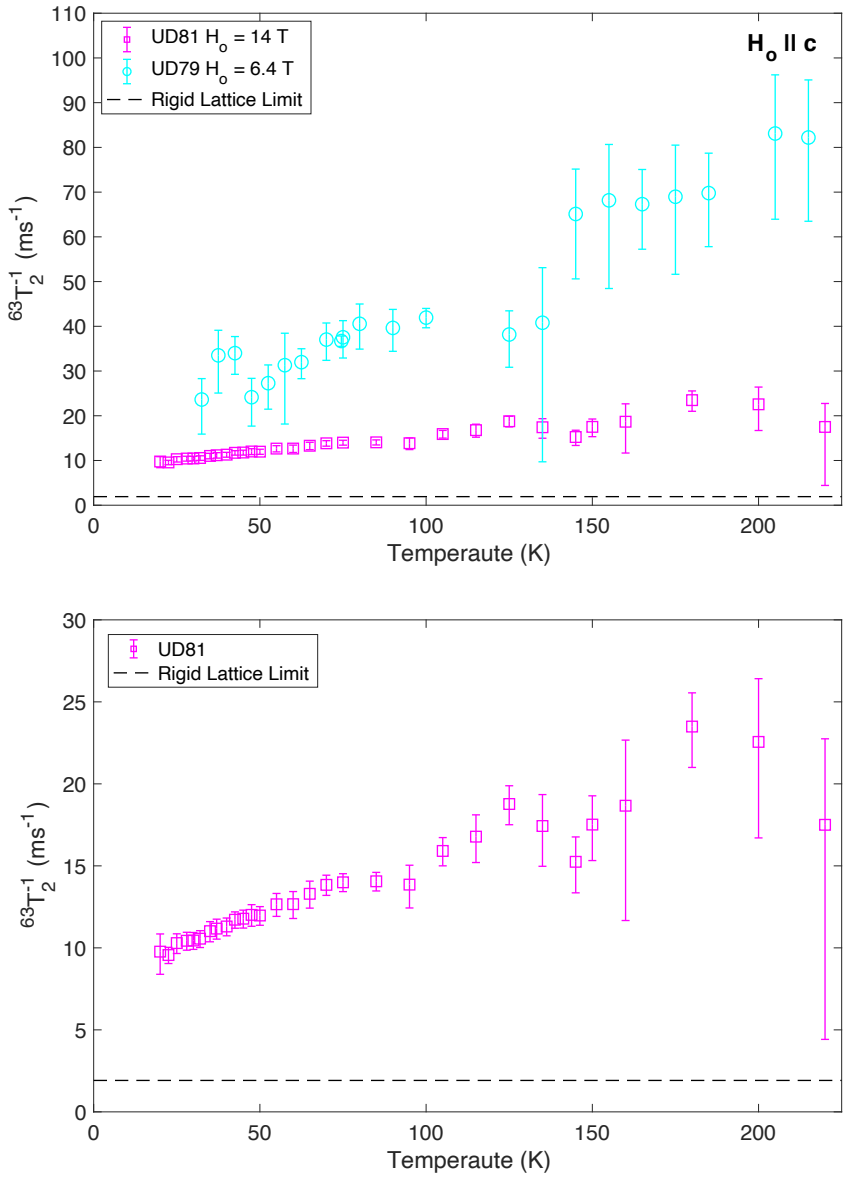

Figure 5.5. The transverse relaxation rate of ^{63}Cu in UD81 at 14 T (magenta) as well as that of UD79 at 6.4 T (cyan). The rigid lattice limit is shown as a dashed line for comparison. The bottom plot is identical to the top but with a smaller $^{63}T_2^{-1}$ scale to show the variation in $T_2{}^{-1}$ for UD81.

inhomogeneties, which are contained in the variable T_2^*. The full expression for $T_2^{-1}(T)$

is,

$$\frac{1}{T_2(T)} = \frac{1}{T_2^*(T)} + \frac{C_R}{T_1(T)},$$

where C_R is the so-called "Redfield coefficient." The derivation of the above expression is included in Appendix B. One can extract C_R by plotting the relaxation rates $T_2^{-1}(T)$ vs $T_1^{-1}(T)$ with T as an implicit parameter and extracting the slope. An example of such a plot is seen in Fig. 5.6.

Recalling the MRS picture in which the Cu^{2+} spin susceptibility is responsible for all nuclear relaxation behavior, we expect the planar ^{17}O relaxation to be influenced by the ^{63}Cu spin-lattice relaxation. We plot the $^{17}T_2^{-1}$ as a function of $^{63}T_1^{-1}$ in Fig. 5.6. The

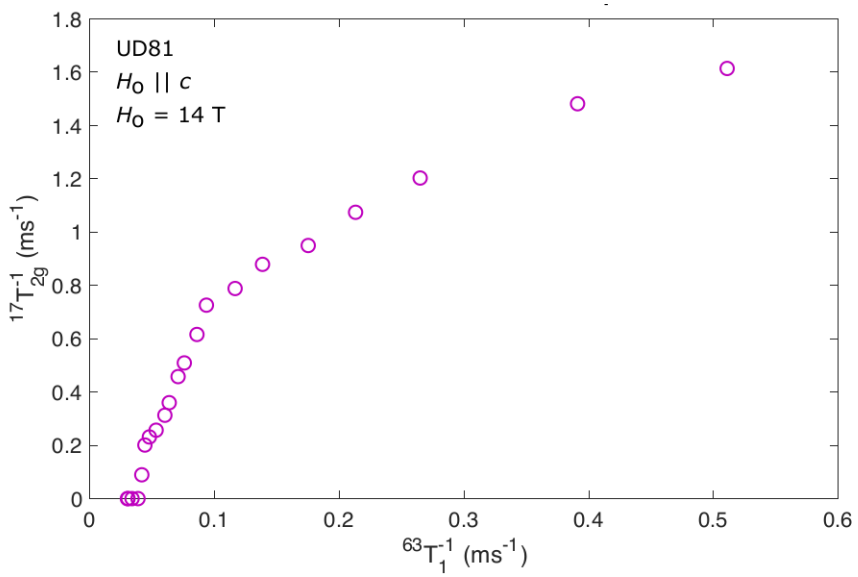

Figure 5.6. A plot of $^{17}T_2^{-1}$ vs. $^{63}T_1^{-1}$ with T as an implicit parameter. The change in slope at the $\approx$ (0.1, 0.8) ms^{-1} mark which corresponds to a temperature between 60 and 70 K.

dependence of $^{17}T_2^{-1}$ on $^{63}T_1^{-1}$ appears to be approximately linear for all temperatures at which $^{17}T_2^{-1}$ is finite, however, the slope of this dependence appears to change at $T \approx 60$ K. This change in slope suggests that around 60 K there is a change in the environment that influences the relaxation mechanism.

5.4. ^{17}O shift and planar $^{17}T_2^{-1}$

We turn now to a discussion of our ^{17}O NMR at the planar oxygen, O(1), site. In Fig. 5.7 we show the total shift, $^{17}K_c$, for $H_o \parallel c$ in the O(1) site of our two under-doped Hg1201 crystals at 14 T. The smaller overall magnitude of this shift tells us that the O(1) orbital shift is much smaller than that of ^{63}Cu (Fig. 5.1). This means that the majority of $^{17}K_c$ comes from the hyperfine coupling to the electronic spin system.

The magnitudes of the shift shown in Fig. 5.7 are in good agreement with those measured by Mounce *et al.* presented in [62] for an under-doped single crystal of Hg1201 at $H_o = 6.4$ T. The percentage value of the spin shift for this same sample is shown in Chapter 5 of Mounce's Ph.D thesis [3]. As we see in our data, the shift is approximately linearly proportional to temperature in our measured range of 20 K to 150 K. If we fit our shift data to a linear slope and extrapolate to 300 K we get a shift of $^{17}K_c = 0.139$ %, which is around what Mounce measured at room temperature. We also note that the error bars shown in our $^{17}K_c$ plots only represent the 95% confidence intervals of the Gaussian fits used to extract the peak frequencies and does not account for the error in our estimation of H_o. The H_o value was estimated by considering the 0.2 ppm/day field drift and adding or subtracting the calculated drift from the measured value of H_o measured

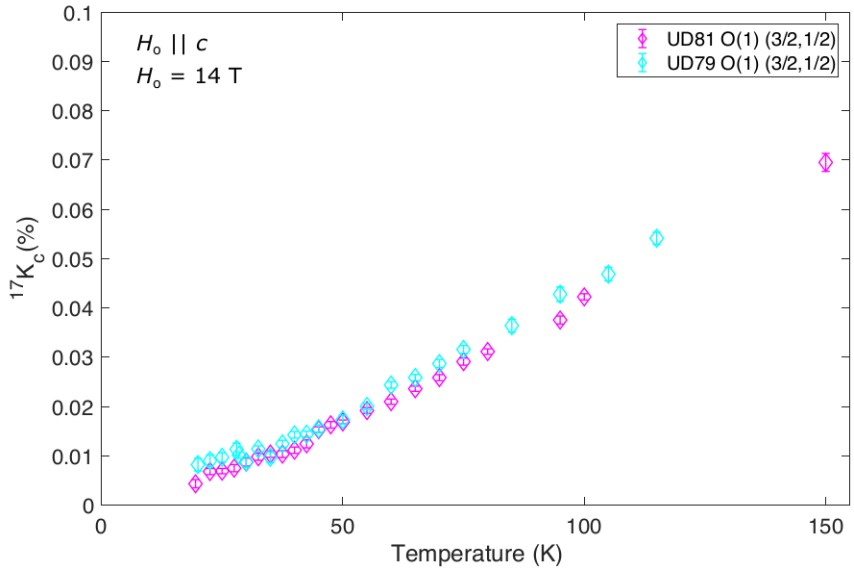

Figure 5.7. The total NMR shift for $H_o \parallel c$ measured at the first high-frequency O(1) ($\pm 3/2 \leftrightarrow \pm 1/2$) satellite. Both UD79 (cyan) and UD81 (magenta) data points were measured at 14 T. The peak frequencies were extracted by fitting to a Gaussian and the error bars are the 95% confidence intervals of the fit.

with ^{63}Cu FID.

For additional comparison with previous NMR data on Hg1201 single crystals we include the total shift measured at the O(2) site of our UD81 sample. This also agrees with data measured by Mounce as well as that presented by Lee [4]. In Fig. 5.8 we show our total shift data for $H_o \parallel c$ at both ^{17}O sites in our UD81 sample measured at 14 T in the top panel. Note that the O(2) shift was measured at the central transition for $T \geq 85$ K since this is the lowest temperature at which the O(1) and O(2) satellites are distinguishable at the $(-1/2 \leftrightarrow +1/2)$ transition at this field. The low temperature shift was measured by subtracting $\nu_Q = 1.2218$ MHz, the O(2) quadrupole shift measured at room

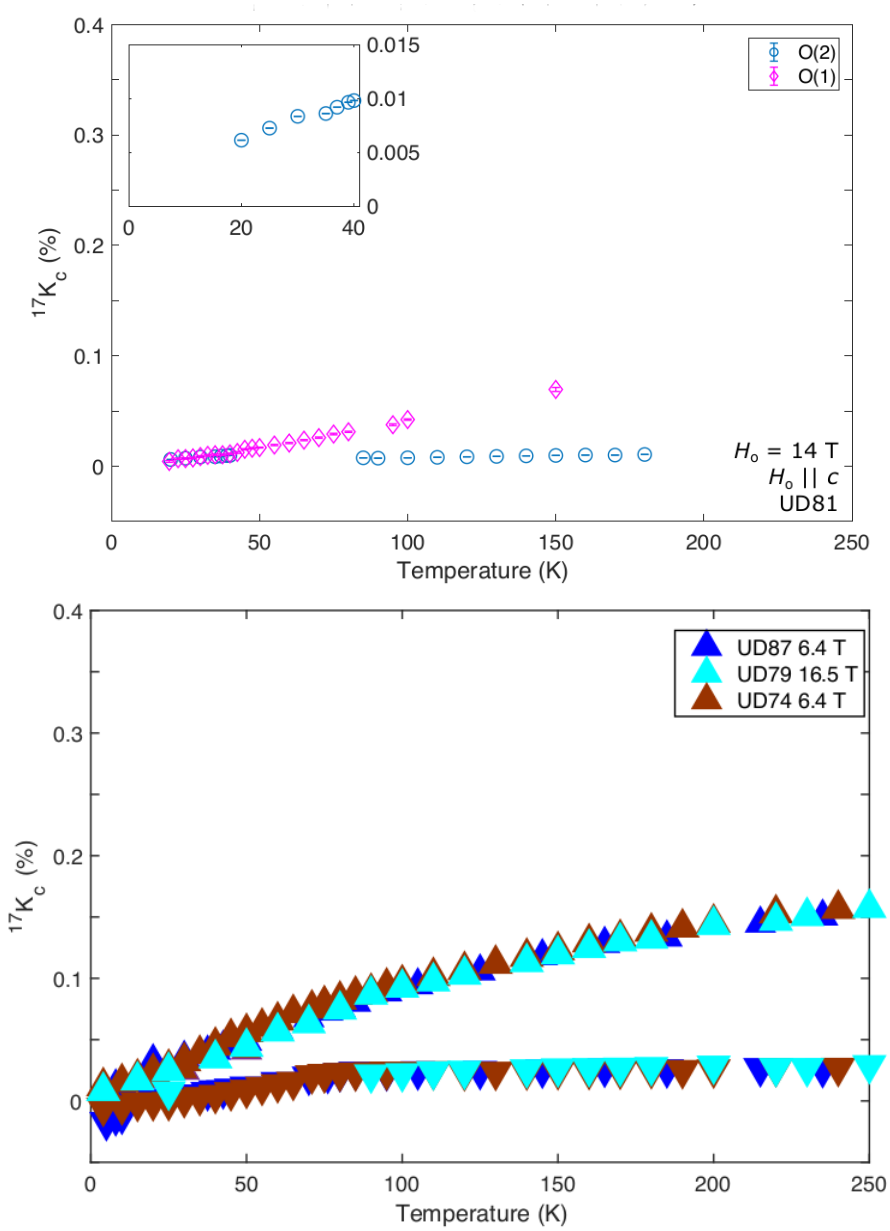

Figure 5.8. The total shift (top) for both apical and planar ^{17}O in our UD81 sample for $H_o \parallel c$. The inset shows the low-temperature behavior of the O(2) shift. The total shift (bottom) presented by Lee in reference [4].

temperature, from the peak frequency of the high-frequency ($\pm 3/2 \leftrightarrow \pm 1/2$) satellite. This procedure likely adds about $\sim \pm 0.005\%$ of error to the $T \leq 80$ K shifts. The shift

data for three under-doped single crystal Hg1201 samples adapted from [4] are shown in the bottom panel.

The data shown in Fig. 5.8 for UD81 are more sparse than those for the other three under-doped samples, but we can see that the magnitudes of the shifts are approximately the same for all samples. Additionally, each sample has a near constant O(2) shift above T_c that begins to decrease with decreasing temperature below T_c while the O(1) shift decreases with temperature at all temperatures. The fact that the magnitude and temperature dependence of the shifts are approximately equal shows that $^{17}K_c$ does not depend strongly on field (note that these measurements were performed at 6.4 T, 14 T and 16.5 T) nor on doping in the under-doped compounds. It also shows that the UD81 sample is comparable in quality and has similar properties to other similar samples.

The similarity of the ^{17}O shift in all samples at fields from 6.4 T to 16.5 T is in contrast to the measured ^{63}Cu shift which varied in magnitude and slightly in temperature dependence between compounds and fields. Lee [4] attributes this to a field-dependence in the ^{63}Cu shift that is not present in ^{17}K as well as a stronger coupling at the Cu sites to the electronic susceptibility.

We return now to our discussion of transverse relaxation. As we saw in Fig. 5.6 the $^{17}T_2^{-1}$ is influenced by the spin-lattice relaxation of the surrounding ^{63}Cu sites. The $^{17}T_2^{-1}$ behavior is also significant because it is influenced by the dynamics of the so-called "mixed state" of cuprate superconductivity. Specifically, the ^{17}O recovery profile

contains valuable information about the motion of magnetic flux lines (vortices) within the CuO_2 planes. These flux lines will be the main focus of the next two chapters. Here we will discuss the theoretical manifestation of the change in vortex dynamics through ^{17}O relaxation and how this compares with our results on Hg1201 single crystals.

5.4.1. $^{17}T_2^{-1}$ in YBCO

In the early ^{17}O NMR studies of $YBa_2Cu_3O_7$ in the mixed state several groups [78, 43] noticed that the spin-spin relaxation rate, T_2^{-1}, exhibited a peak in it's temperature dependence which happened to coincide with the vortex lattice melting temperature, T_m. It was later discovered [9] that this peak was an artifact of extracting T_2^{-1} by fitting the magnetization decay, $M(2\tau)$ vs 2τ, to a single Gaussian form, $M(2\tau) \propto \exp[-(2\tau/T_2)^2]$.

Upon fitting the decay to a two-function form, $M(2\tau) \propto \exp[-(2\tau)/T_{2e} - (2\tau/T_{2g})^2]$, it became clear that the ^{17}O transverse relaxation is dominated by a Gaussian T_2, T_{2g}, above a certain temperature, T_p, whereas below this temperature the decay begins to develop and exponential component, T_{2e}, which increases with decreasing temperature. This increase in T_{2e}^{-1} is accompanied by a decrease in T_{2g}^{-1}, which is approximately zero at the lowest temperatures where all vortices are quasi-static on the time scale of an NMR experiment. Fig. 5.9 shows the T_2 results at four different fields.

Bachmann *et al.* refer to the temperature T_p as the vortex pinning temperature, below which vortices are pinned but not necessarily forming an Abrikosov lattice. There is a region below T_p where the vortex liquid and vortex solid regimes overlap, i.e. a region

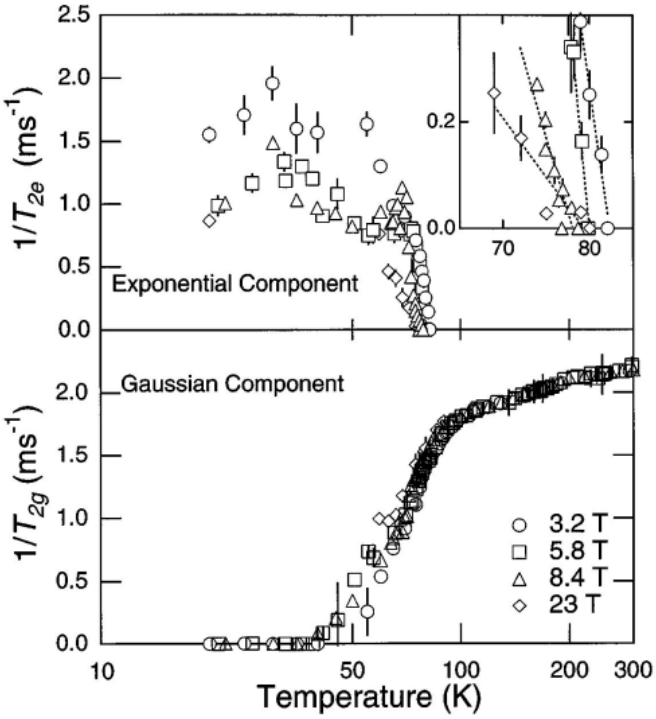

Figure 5.9. Figure 3 from [9] showing the exponential (T_{2e}^{-1}) and Gaussian (T_{2g}^{-1}) contributions to the spin-spin relaxation rate at the planar oxygen site in an aligned powder sample of $YBa_2Cu_3O_7$.

where both T_{2e}^{-1} and T_{2g}^{-1} contribute to the decay. The group notes that their aligned powder samples likely have a much greater density of pinning centers than the clean, untwinned YBCO single crystals for which T_m is well defined [9]. Nevertheless the data in Fig. 5.9 gives strong evidence for the claim that the exponential decay is associated with pinned vortices, which have a Lorentzian spectral density.

5.4.2. $^{17}T_2^{-1}$ in Hg1201

We have performed T_2 measurements on two under-doped Hg1201 single crystal samples and found that the Gaussian spin-spin relaxation rate decayed with decreasing temperature at low temperatures much like in the case of the near-optimally doped YBCO aligned powder samples in reference [9]. However, we do not find any appreciable increase in the measured T_{2e}^{-1} value at any temperature (see Fig. 5.10).

For a clearer picture of the changing relaxation as a function of temperature we fitted the data to the product of a Gaussian and an exponential with constant exponential decay time, T_{2C},

$$M(2\tau) = M_o \exp\left[-\left(\frac{(2\tau)}{T_{2g}}\right)^2 - \frac{(2\tau)}{T_{2C}}\right]. \tag{5.3}$$

The resulting $^{17}T_2^{-1}(T)$ behavior is shown in Fig. 5.12. In Fig. 5.11 we show the magnetization decay profiles of the UD81 and UD79 samples at two different temperatures, T = 20 K, where the Gaussian relaxation rate is negligible, and T = 80 - 85 K, where the decay has some Gaussian contribution. The dashed line shows the exponential component only. Note that at low temperatures (cornflower blue) the decay fits very well to the pure exponential whereas at high temperatures (magenta) the magnetization appears to contain an additional Gaussian component.

From our plots of $^{17}T_2^{-1}$ at 14 T we can see that the Gaussian decay rate is negligibly small below a temperature of around 30 K for both underdoped samples. Lee *et al.* [4, 58] proposed that the onset temperature for the vortex liquid-to-solid transition in Hg1201

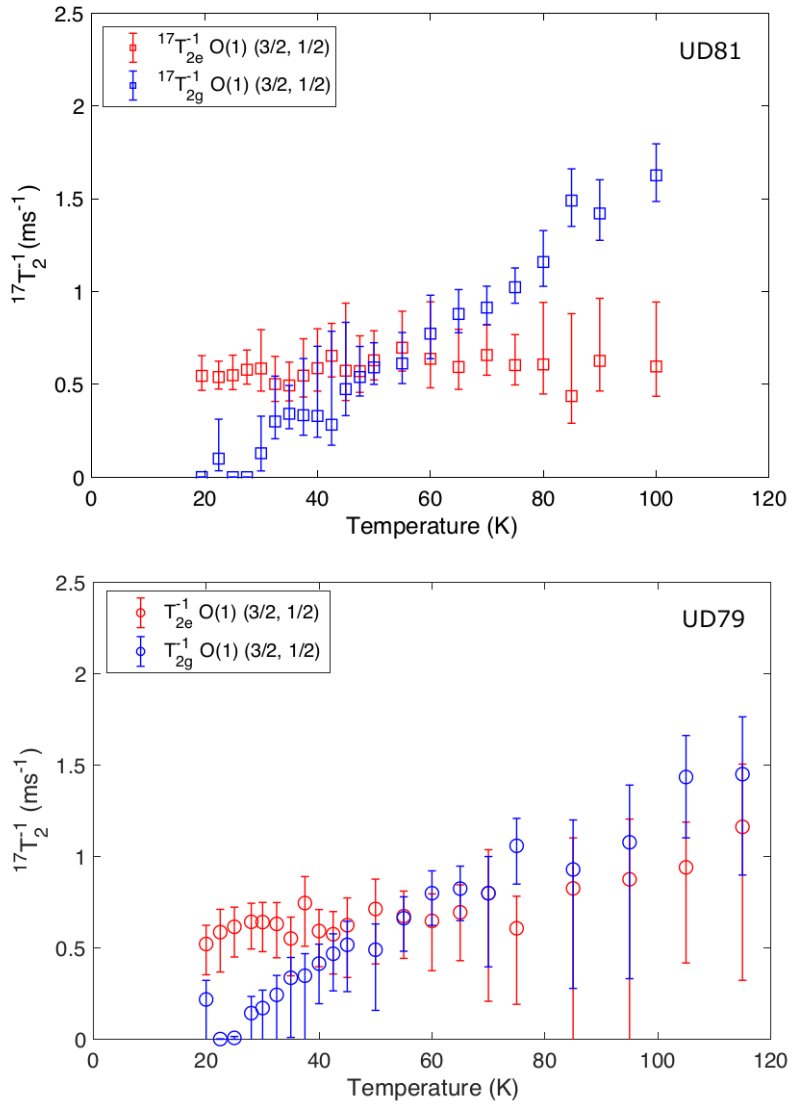

Figure 5.10. Spin-spin relaxation ^{17}O NMR measurements for two under-doped Hg1201 single crystal samples with $T_c = 81$ K (top) and $T_c = 79$ K (bottom). The relaxation was measured at the first high-frequency satellite of the planar oxygen, O(1), site.

single crystal samples could be deduced by the location of a discontinuity in the $T_2{}^{-1}(T)$ when fitting the decay to a single Gaussian function. This was interpreted to take place around 40 K for all under-doped samples investigated. However, the lack of any detectable

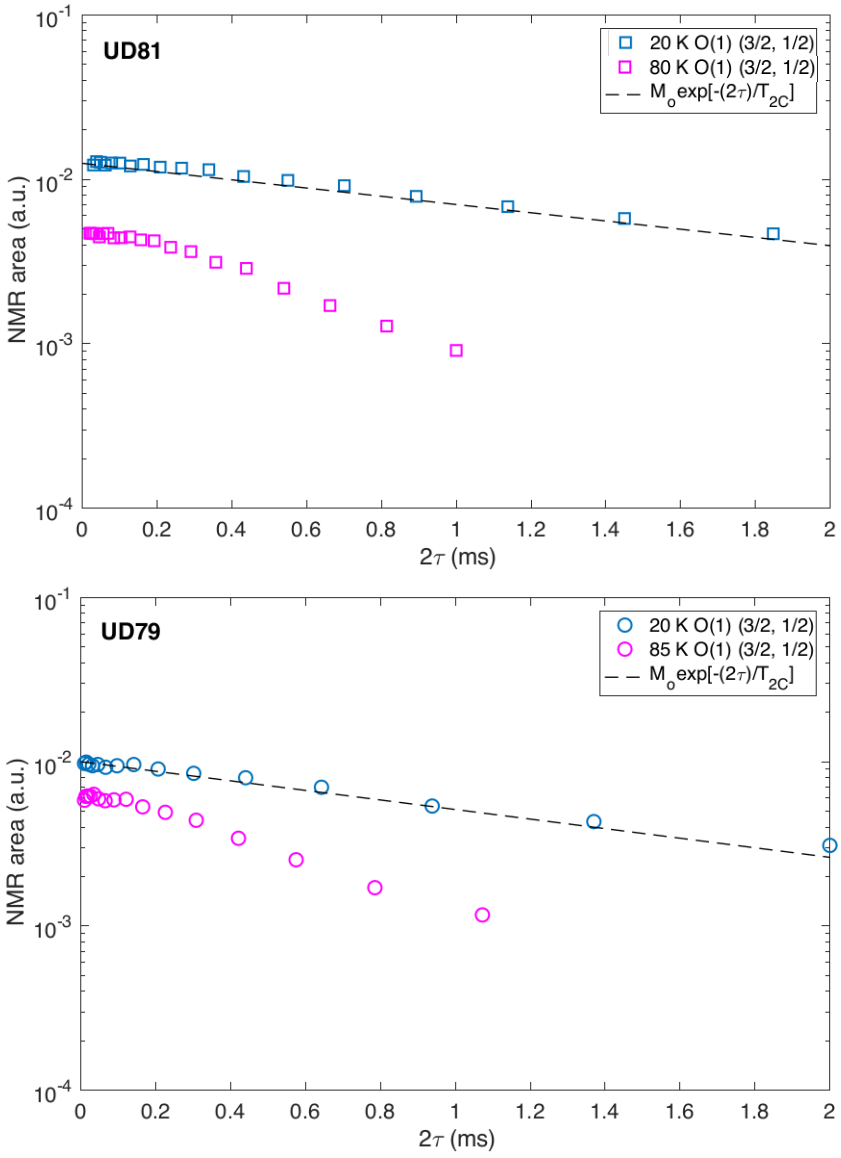

Figure 5.11. Magnetization vs time profiles measured via a Hahn echo sequence of $\pi/2$-τ-π-acquire with varying τ. The dashed line shows the pure exponential with decay constant T_{2C}, where T_{2C} = 1.735 ms (UD81, top) and 1.492 ms (UD79, bottom). These T_{2C} values were obtained by taking the average T_{2e} from the plots seen in Fig. 5.10.

change in the exponential component of T_2 in our 14 T data indicates that vortices in

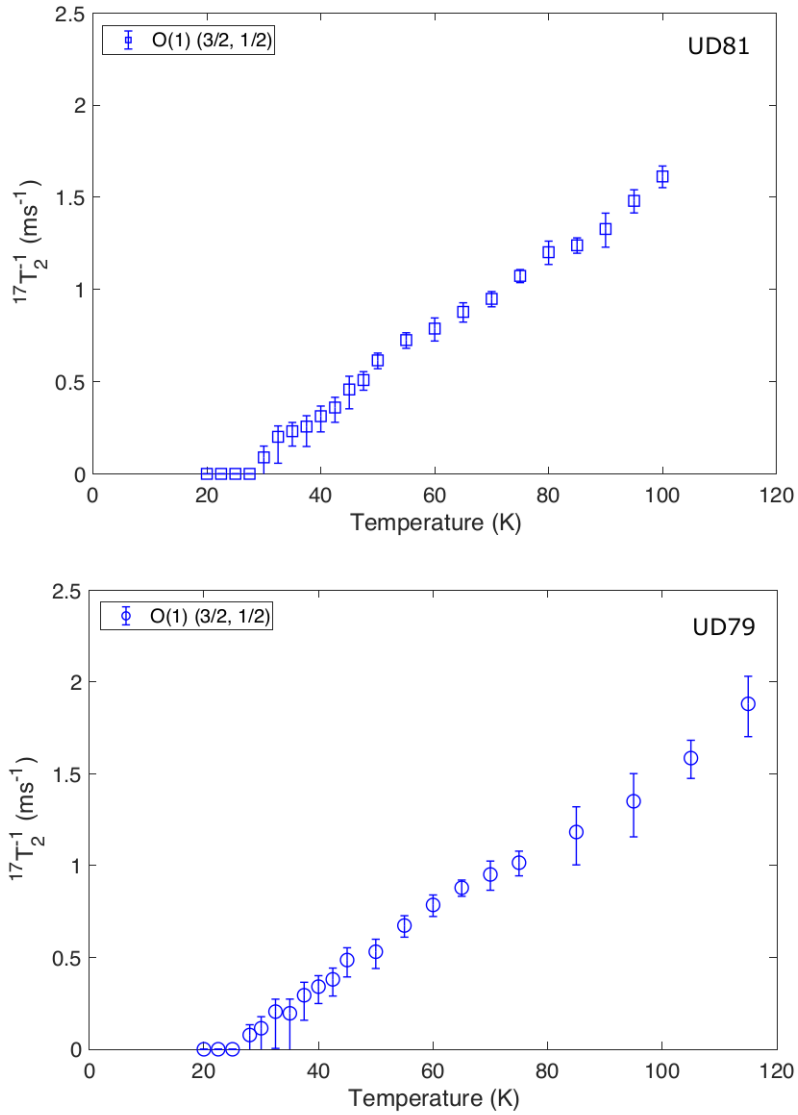

Figure 5.12. Plots of the Gaussian decay rate, T_{2g}, fit to Eq. (5.3) with the T_{2C} values given in the caption of Fig. 5.11.

these compounds may not be in a solid state at $T \geq 20$ K.

To investigate this $^{17}T_2^{-1}$ temperature dependence further we looked at the temperature dependence of $^{17}T_{2e}^{-1}$ and $^{17}T_{2g}^{-1}$ at the O(1) ($\pm 3/2 \leftrightarrow \pm 1/2$) high-frequency transition

at $H_o = 19$ T at temperatures down to 5 K in our UD81 sample. At this field we see an onset of an increase of $^{17}T_{2e}^{-1}$ starting at around 10 K. However, unlike the 14 T data we do not see a $^{17}T_{2g}^{-1}$ contribution to the transverse relaxation rate at temperatures up to 50 K. There is a small increase in $^{17}T_{2g}^{-1}$ at 60 K, but further measurements at this field at higher temperatures are needed to confirm that this is the case. It is also possible that the mechanism for $^{17}T_{2g}^{-1}$ relaxation is suppressed at higher fields, which is also worth investigating by repeating our $^{17}T_2^{-1}$ measurements at various H_o. Our 19 T results are shown in Fig. 5.13.

The observed increase in $^{17}T_{2e}^{-1}$ at low temperatures for $H_o = 19$ T could indicate that vortices in this sample transition to a quasistatic "solid" state at a temperature of about 10 K at this field. It is also possible that a vortex solid has formed at a higher temperature, but that vortex pinning onsets below a temperature of about 10 K. We must also account for the possibility that this increase in $^{17}T_2^{-1}$ is unrelated to vortices and is indicative of the quasiparticle behavior rather than field fluctuations. We discuss some examples of this interpretation as it relates to previous NMR measurements in greater detail in Chapters 6 and 7.

We note that all of our $^{17}T_2^{-1}$ measurements below 20 K were performed at the first high-frequency O(1) satellite. More data is needed to determine if the origin of the low-temperature increase in $^{17}T_2^{-1}$ is caused by field fluctuations, such as those cited by Bachmann *et al.*, or by hyperfine coupling to the nodal quasiparticles. It would be interesting to repeat our T_2 measurements at the O(2) site where the hyperfine coupling to

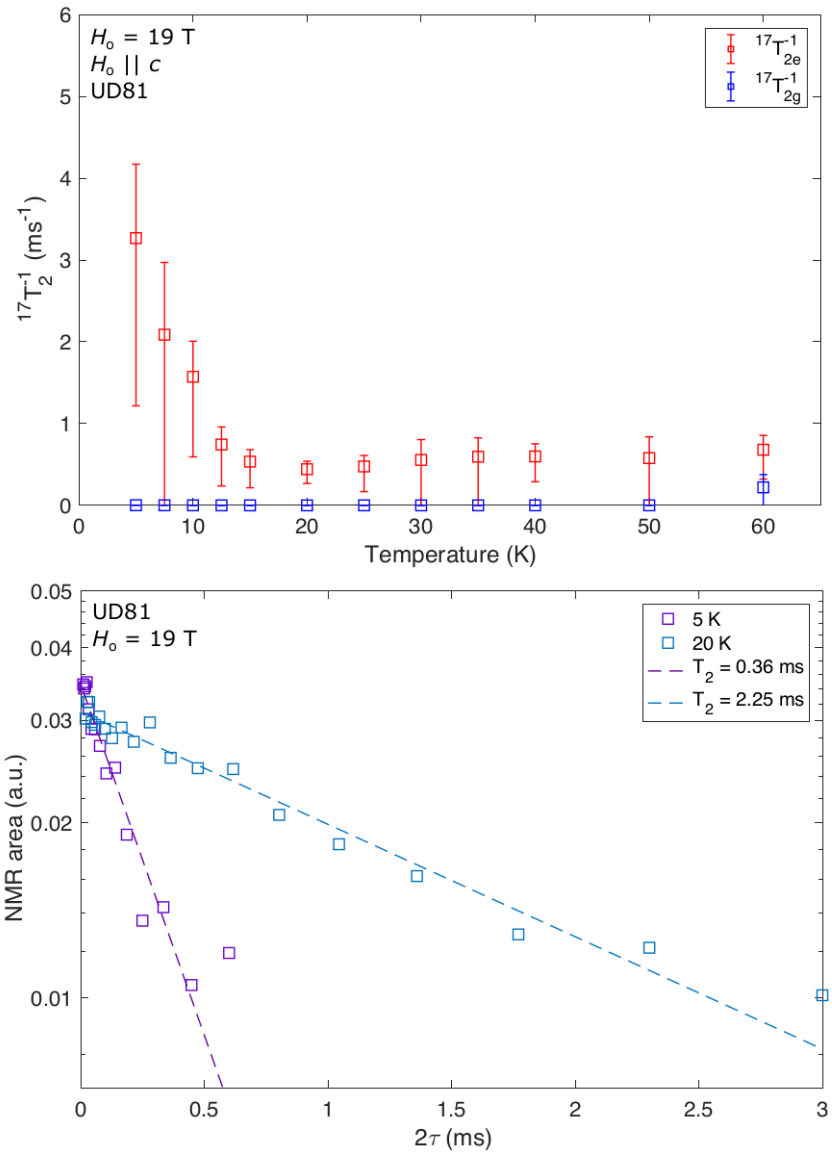

Figure 5.13. Our $^{17}T_2^{-1}$ data for $H_o \approx 19$ T at low temperatures with $H_o \parallel c$. The top plot shows the measured relaxation rates as a function of temperature while the bottom plot shows the decay profiles, $M(2\tau)$ vs. 2τ measured at 20 K (cornflower blue) and 5 K (violet). The dashed lines are fits to an exponential decay with decay constant T_2 (see legend).

the CuO_2 plane is much weaker as evidenced by Knight shift analysis. If the temperature dependence of $^{17}T_2^{-1}$ is similar at both sites then the $^{17}T_{2e}^{-1}$ increase is likely be caused

by a change in the vortex dynamics leading to a change in the local fields. This could also be confirmed by measuring T_2 as a function of temperature at the ^{199}Hg site which will see the same VL field as the other nuclei. If the O(2) site shows a weaker or different temperature dependence of the relaxation than the O(1) site then the low-temperature behavior of $^{17}T_2^{-1}$ is likely related to the physics coupled to the hyperfine field of the CuO_2 plane.

5.5. Conclusions

We have seen how we can probe the physics in the superconducting plane with NMR at the planar ^{63}Cu and ^{17}O sites. The MRS Hamiltonian shows that the hyperfine fields of the CuO_2 plane control the shifts and influences the nuclei in the unit cell. We have also seen how the spin-spin relaxation rate of the nuclei in a system can be affected by the relaxation of the surrounding nuclei. Most notably, we see that the $^{17}T_2^{-1}$ relaxation rate at 14 T does not have a temperature-dependent exponential contribution at temperatures down to 20 K, which is in contrast to the data from Bachmann *et al.* [9] on YBCO. We do see an increase in $^{17}T_{2e}^{-1}$ at 19 T for temperatures below 10 K, but further measurements at this field at higher temperatures are needed to confirm that the relaxation behavior is consistent with the YBCO picture. Additional $^{17}T_2^{-1}$ measurements at the O(2) and ^{199}Hg sites would also aid in our understanding of the origin of the relaxation behavior.

CHAPTER 6

Vortex physics and Brandt's algorithm

As we mentioned in the introduction, the cuprate superconductors are *unconventional*, meaning they cannot be described by BCS theory, in which the energy gap, Δ_{BCS}, is isotropic. In 1987 it was first suggested [79] that the superconducting gap may have a d-wave structure rather than the s-wave structure of the BCS gap. This notion was fueled by growing evidence that quasiparticle excitations were present in cuprate superconductors down to the lowest temperatures even in the cleanest, most defect-free samples. It is now generally accepted that the electron pairs that yield superconductivity in cuprates are spin-singlets with a d-wave gap structure. This implies that quasiparticles (unpaired electrons/holes) are present and contribute to the density of states (DOS) even at the lowest temperatures. Later in this chapter we will show how we can use NMR to study these low-temperature quasiparticle excitations at the nodes of the superconducting gap in the so-called mixed state.

In addition to being unconventional the cuprates are type II SCs, meaning that they exhibit a magnetic state in which superconducting regions are penetrated by non-superconducting regions carrying magnetic flux. In this chapter we focus on the physics of this "mixed state," how to calculate its properties, and how we can use NMR to probe it. We begin by reviewing the classification of SCs as type I or type II.

6.1. Type I and Type II superconductivity

In the years following the discovery of superconductivity in elemental mercury many elemental metals were found to be superconducting, exhibiting zero resistance when cooled down to very low temperatures (several Kelvin or lower), and perfect diamagnetism in a magnetic field, H. As well as having a characteristic transition temperature, T_c, these SCs also have a characteristic *critical field*, H_c. That is, these materials will expel their internal magnetic fields as long as $H < H_c$. If the field is increased to $H > H_c$ the sample will return to a non-superconducting (normal) state where the field can penetrate the bulk of the material.

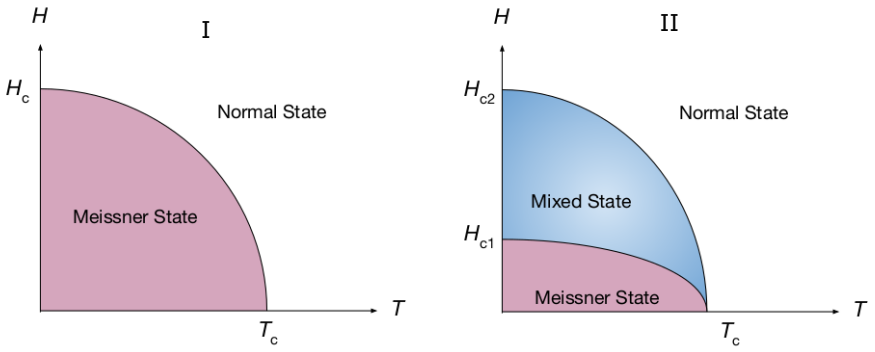

Figure 6.1. The H vs. T phase diagram of a type I (left) and type II (right) SC.

What we have just described is known as a type I SC. When placed in a field, H, these materials will either exhibit a Meissner state or a normal state depending on whether H is stronger than or weaker than H_c. The H vs T phase diagram for this class of materials is shown in Fig. 6.1 (left).

The class of SCs known as type II SCs, however, have two characteristic critical fields, a lower critical field, H_{c1}, and an upper critical field, H_{c2}, where $H_{c1} < H_{c2}$. For $H < H_{c1}$ a type II SC will exist is a Meissner state of perfect diamagnetism. When the field is increased such that $H_{c1} < H < H_{c2}$ the system will form a *mixed state* of superconducting and non-superconducting regions. The non-superconducting regions allow the field to penetrate in fixed areas such that the magnetic flux passing through the area is limited to one magnetic flux quantum, $\Phi_o = \frac{hc}{e}$, where h is Planck's constant, c is the speed of light and e is the magnitude of the electron charge. This normal region is surrounded by circulating superconducting currents which decay on a radial length scale of λ, the superconducting penetration depth. This region of penetrating field surrounded by circulating supercurrents is know as a vortex. The non-superconducting region is the vortex core, which has a radius on the order of the superconducting coherence length, ξ.

The mixed state of a type II SC was first theoretically described by Ginzburg and Landau in 1950 [19]. The pair showed that the criteria for a SC to display type II superconductivity was that the material have a Ginzburg-Landau (GL) parameter, $\kappa \equiv \lambda/\xi > 1/\sqrt{2}$. The GL theory begins by assuming a complex order parameter, $\psi(\boldsymbol{r})$, where $|\psi(\boldsymbol{r})|^2$ is proportional to the density of superconducting charge carriers. The theory assumes that the free energy density of the system can be expanded in powers of $|\psi(\boldsymbol{r})|^2$ and $|\nabla\psi(\boldsymbol{r})|^2$ [29] as follows,

$$f = f_{n0} + \alpha|\psi|^2 + \frac{\beta}{2}|\psi|^4 + \frac{1}{2m^*}\left|\left(\frac{\hbar}{i}\nabla - \frac{e^*}{c}\boldsymbol{A}\right)\psi\right|^2 + \frac{h_a^2}{8\pi}. \tag{6.1}$$

Here f_{n0} is the free energy density in the normal state where $|\psi(\boldsymbol{r})| = 0$, $\hbar$ is the reduced Planck's constant, m^* is the effective mass of the superconducting charge carrier, e^* is the effective charge of such a carrier, c is the speed of light and h_a is the applied magnetic field. The coefficients α and β are phenomenological parameters.

By minimizing the GL free energy density, f, with respect to ψ^* and $\boldsymbol{A}$, the magnetic vector potential, one arrives at the GL equations for $\psi(\boldsymbol{r})$ and $\boldsymbol{A}(\boldsymbol{r})$. In practice the GL theory proves to be valid only at temperatures very close to T_c. However, the theory can be extended to lower temperatures in certain cases where the behavior of the system can be approximated by its $T \approx T_c$ behavior.

6.1.1. The Abrikosov vortex lattice

In 1957 Abrikosov [20, 21] built on the theories developed by Ginzburg and Landau, as well as theories proposed by Onsager [80] and Feynman [81] for vortices in helium II, to calculate and predict that vortices in a type II SC should form a periodic structure in the absence of thermal fluctuations. Abrikosov did this by solving the GL equations for ψ and $\boldsymbol{A}$ in the vicinity of $H \sim H_{c2}$. Abrikosov's periodic system of vortices became known as the *vortex lattice* (VL) and it was first experimentally demonstrated in an indium-lead alloy by scanning electron microscopy in 1967 by U. Essmann and H. Träuble [82]. Since then many experimental methods of observing the VL in type II SCs have been developed.

One popular method of studying the VL is to use Small-Angle Neutron Scattering (SANS) to image the VL by scattering neutrons off the vortex cores. Other methods

of imaging the VL include scanning tunneling microscopy (STM), magnetic decoration and scanning Hall probe microscopy [83]. These methods produce a visual map of the locations of the vortex cores, which makes them useful for studying geometric properties of the VL. However, these methods cannot probe the behavior of quasiparticles in specific regions of the VL. That is, these methods cannot distinguish between excitations of quasiparticles localized in the vortex core and those of quasiparticles outside the core. Additionally, methods such as STM only measure the surface states and involve using an external probe that interacts with vortices thereby potentially changing the properties of the systems as they are observed [9].

One advantage of using NMR is that it is a bulk probe, meaning that we study the bulk of a material within an rf penetration depth below the sample surface. The NMR probe is also relatively non-invasive which lowers the risk of us altering the properties we wish to observe. Additionally, NMR experiments can be performed at higher fields than other imaging methods. Perhaps most importantly, through NMR we are able to study local behavior of quasiparticles through their interactions with the nuclear spin.

We are able to study the VL with the NMR probe because the vortices in the VL state are static on the timescale of an NMR measurement. This static arrangement of normal cores surrounded by circulating supercurrents creates a distinct local magnetic field profile which in turn results in a distinct NMR spectrum. The NMR spectrum is essentially a probability distribution of local fields with certain points in the frequency spectrum corresponding to specific points in real space. Fig. 6.2 shows the correspondence between

the field distribution (the NMR spectrum) and the regions of the VL in real space. The 3D plot at the top right shows vortices represented as peaks in the field $B(x, y)$ as a function of the x and y positions, given in units of the (vortex) lattice spacing, x_1. The apex of each peak is the vortex core (yellow), which is the point of maximum magnetic field; the region of circulating supercurrents (blue) occupies that larges area and therefore has the highest probability; the saddle point (purple) is the region of supercurrent overlap between adjacent vortices and is the region where the field is the smallest. The corresponding regions of the NMR spectrum, $P(H_{int})$, are shaded accordingly in the plot on the left.

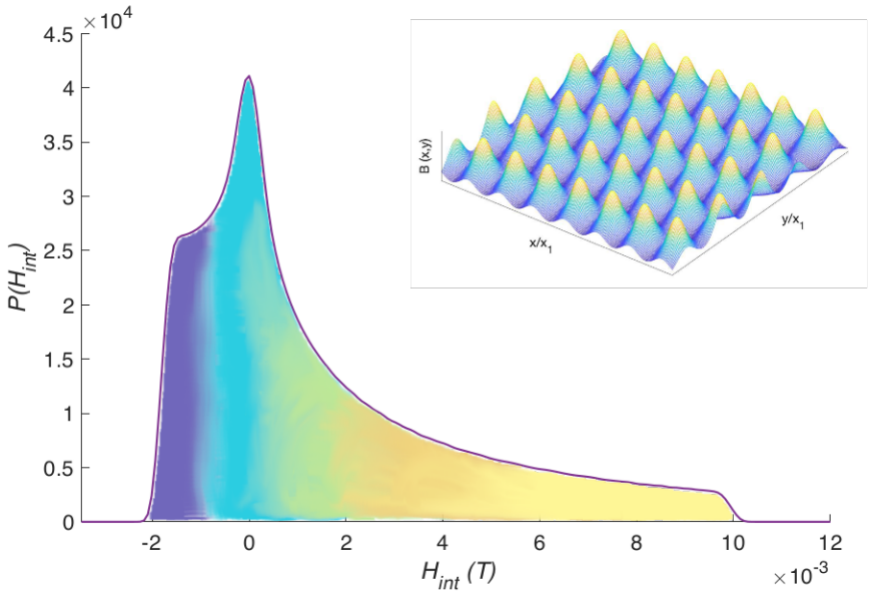

Figure 6.2. The field distribution calculated using GL theory of a VL at 13 T with parameters from YBCO found in reference [2]. The coloring of the area under the $P(H_{int})$ curve corresponds to the region of the VL, whose 3D field plot is represented in the inset at the top right. The spectrum was calculated using Brandt's algorithm.

This direct correspondence between the NMR spectrum and points on the VL allows us to study local quasiparticle excitations through their interaction with nuclei in specific regions of the VL. We will return to this interpretation later in the chapter. First we will show how we can calculate the local magnetic field profile that we expect to see in an NMR spectrum using GL theory.

Although the calculation methods we describe below assume the system is two-dimensional they can be valid for a cuprate system due to the fact that the superconductivity occurs only in the CuO_2 planes. Therefore, as long as the vortices in each layer remain weakly coupled to those in adjacent CuO_2 layers, the system should behave as a 2D superconducting film which is well described by this 2D model.

6.2. Geometry of the vortex lattice

As with a regular lattice structure, a VL consists of a periodically ordered arrangement of vortices, which we assume to carry one magnetic flux quantum each. We can describe the VL geometry by defining lattice vectors and reciprocal lattice vectors which give the positions of the vortices in real and reciprocal space, respectively. The principal lattice vectors are defined as, $\boldsymbol{R}_{mn} = (mx_1 + nx_2)\hat{\boldsymbol{x}} + ny_2\hat{\boldsymbol{y}}$, where

$$x_1 = a_0, \tag{6.2}$$

$$y_2 = \eta x_1 \sin\alpha, \tag{6.3}$$

$$x_2 = \eta x_1 \cos\alpha. \tag{6.4}$$

Here a_0 is the distance between adjacent vortex cores, η is the lattice anisotropy and α is the lattice angle. The corresponding reciprocal lattice vectors are given by $\boldsymbol{K}_{mn} = (2\pi/S)my_2\hat{\boldsymbol{x}} + (nx_1 + mx_2)\hat{\boldsymbol{y}}$, where S is the VL unit cell area, $S = x_1y_2 = \Phi_o/B_{\text{avg}}$. The field B_{avg} is the spatial average of the field over the VL unit cell. Fig. 6.3 shows the contour plot of the local field for an orthorhombic VL in real space calculated using Ginzburg-Landau (GL) theory.

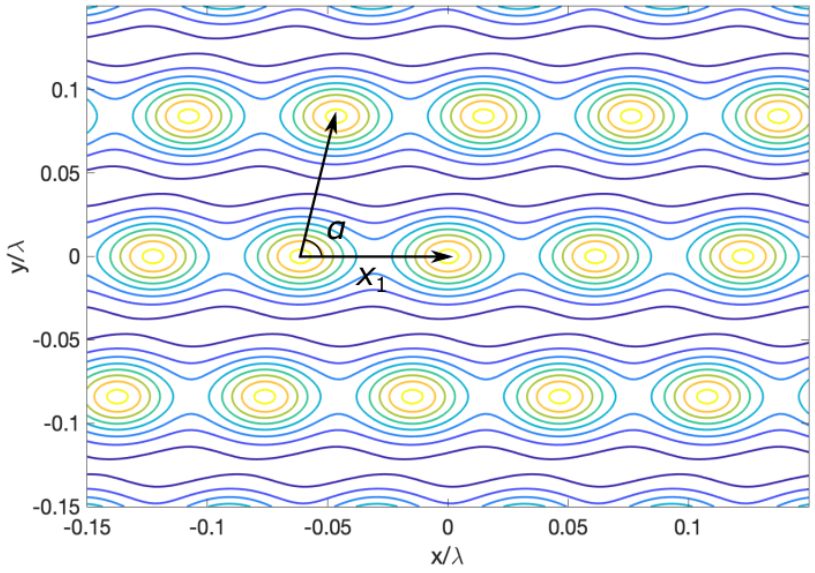

Figure 6.3. A countour plot of the VL field profile shown in Fig. 6.2. The yellow regions correspond to vortex cores and the green-purple lines indicate circulating supercurrents. The opening angle, α, is 80°.

The lattice spacing is dependent on the external field as, $a_0 = \xi\sqrt{(2\pi)H_{c2}/(H_o\eta\sin\alpha)}$ and the anisotropy is defined as, $\eta = \Phi_o/(H_o a_0^2 \sin\alpha)$, which is the ratio of the magnitude of the two vectors shown in Fig. 6.3. If we note that the upper critical field is defined as

$H_{c2} = \Phi_o/(2\pi\xi^2)$ we see that the VL geometry is defined by the intrinsic length scales of the SC, λ and ξ, and the applied field, H_o. In the next section we will discuss how we can calculate the local properties of a VL using only these parameters as inputs. It is useful to be able to calculate local properties of the VL such as local field distribution because the NMR spectrum is essentially a histogram of local fields at the nuclei. By this reasoning, the NMR spectrum should be a convolution of the calculated field distribution and the normal state spectrum.

6.2.1. Resolving VL geometry with NMR

We touch briefly on the claim made by Lee *et al.* [58] that the NMR spectrum of the O(2) satellite in Hg1201 can be used to detect the geometry of the VL. This study relied on a de-convolution technique to isolate the contribution of the VL to the NMR spectrum of the high-frequency O(2) ($\pm 3/2 \leftrightarrow \pm 1/2$) satellite by dividing out the normal-state time domain spectrum measured at 90 K from the low temperature spectrum and taking the Fourier transform of the resulting spectrum to be the isolated VL field distribution. We have avoided using this de-convolution technique due to concerns that this method might complicate the spatial resolution interpretation of the resulting spectrum. As we will discuss in detail in the next chapter, we do not see any evidence for a change in the lineshape with field nor do we see any evidence that the spectrum can be used to resolve the underlying VL geometry. For this reason, we propose that NMR is not suitable for studying VL geometry and have chosen not to pursue this question further.

6.3. Brandt's VL calculation

Following Abrikosov's prediction of the VL and his famous H_{c2} solution of the GL equations, theorists began looking for ways to expand the solution to all fields between H_{c1} and H_{c2} [84]. Early attempts by Ihle [85], Clem [86] and later extensions by Clem and Hao [87] yielded accurate magnetization curves and H_{c2} values using various approximation methods. Although these theories yielded very good approximations to the exact GL result, they were also limited in that they could not distinguish between the energies of various lattice geometries.

In 1972 E. H. Brandt proposed a variational method of solving the GL equations for an ideal 2D VL to any desired accuracy. He did this by writing the GL free energy in terms of real periodic functions $B(x, y)$ and $\omega(x, y) = |\psi(x, y)|^2$, where $\psi(x, y)$ is the complex order parameter and $B(x, y)$ is the induction, and minimizing the free energy with respect to a fixed number of Fourier coefficients [88]. While this method would in principle give exact results, the limited computational efficiency at the time restricted calculations to a small number of variational parameters, which limited the field range that could be used. In 1997 Brandt was able to refine his computational method using an iterative technique that allowed one to calculate up to 1000 Fourier coefficients of B and ω to high precision even on a standard personal computer [84].

Brandt's algorithm is valid at all fields between H_{c1} and H_{c2} and all $\kappa \geq 1/\sqrt{2}$. It is also valid for arbitrary lattice geometries and can be used to compute the shear modulus,

the free energy difference between a triangular and square VL geometry. Here we will discuss how we use Brandt's method to compute the field distribution of a VL. Another good approximation would be to use the London model, which gives a good approximation of local fields for systems with large κ at low fields, $H_{c1} < H_0 \ll H_{c2}$. For a detailed discussion of calculating the field distribution using the London method see references [2, 3, 4].

The GL free energy is given by Eq. (6.1) for a system with order parameter $\psi(x, y)$. We first re-write the GL free energy density, f in units of B_c^2/μ_o, where $B_c = \Phi_o/(\sqrt{8}\pi\lambda\xi)$ is the thermodynamic critical field. The free energy density then becomes,

$$f = \left\langle -|\psi(x,y)|^2 + \frac{1}{2}|\psi(x,y)|^4 + \left|\left(\frac{\nabla}{i\kappa} - \boldsymbol{A}\right)\psi(x,y)\right|^2 + B^2 \right\rangle, \tag{6.5}$$

where the brackets $\langle \cdots \rangle$ denote the spatial average. To simplify the expression we write $\psi(x, y)$ in terms of it's amplitude and phase as follows, $\psi(x, y) = \sqrt{\omega(x, y)}e^{-i\phi(x,y)}$. We also introduce the supervelocity, $\boldsymbol{Q} = \boldsymbol{A} - \nabla\phi(x, y)/\kappa$, where $\boldsymbol{A}$ is the magnetic vector potential defined such that $\boldsymbol{B} = \nabla \times \boldsymbol{A}$. This gives the free energy density as,

$$f = \left\langle -\omega + \frac{\omega^2}{2} + \frac{(\nabla\omega)^2}{4\kappa^2\omega} + \omega\boldsymbol{Q}^2 + (\nabla \times \boldsymbol{Q})^2 \right\rangle. \tag{6.6}$$

In these units all lengths are measured in terms of λ and all fields in terms of $\sqrt{2}B_c$. These units allow all quantities to be defined in terms of κ and $b \equiv H_o/H_{c2}$.

Using the inversion symmetry of the lattice and assuming one magnetic flux quantum, Φ_o, per vortex we may express the variables ω, B and $\boldsymbol{Q}$ as Fourier series:

$$\omega(\boldsymbol{r}) = \sum_{\boldsymbol{K}} a_{\boldsymbol{K}}\big(1 - \cos(\boldsymbol{K}\cdot\boldsymbol{r})\big), \tag{6.7}$$

$$B(\boldsymbol{r}) = B_{\text{avg}} + \sum_{\boldsymbol{K}} b_{\boldsymbol{K}} \cos(\boldsymbol{K}\cdot\boldsymbol{r}), \tag{6.8}$$

$$\boldsymbol{Q}(\boldsymbol{r}) = \boldsymbol{Q}_A(\boldsymbol{r}) + \sum_{\boldsymbol{K}} b_{\boldsymbol{K}} \frac{\hat{\boldsymbol{z}}\times\boldsymbol{K}}{K^2} \sin(\boldsymbol{K}\cdot\boldsymbol{r}). \tag{6.9}$$

Here $\boldsymbol{r} = (x, y)$ is the real space position and the sums are over all reciprocal VL vectors for which $K_{mn} \neq 0$. The subscript A denotes the Abrikosov solution for $B \sim H_{c2}$.

To solve for the Fourier coefficients, $a_{\boldsymbol{K}}$ and $b_{\boldsymbol{K}}$, we first solve the two GL equations, $\delta f/\delta\omega = 0$ and $\delta f/\delta\boldsymbol{Q} = 0$, which gives the following iterative expressions,

$$a_{\boldsymbol{K}} = \frac{4\kappa^2\big\langle(\omega^2 - 2\omega + \omega Q^2 + \frac{(\nabla\omega)^2}{4\kappa^2\omega})\cos(\boldsymbol{K}\cdot\boldsymbol{r})\big\rangle}{K^2 + 2\kappa^2}, \tag{6.10}$$

$$a_{\boldsymbol{K}} = a_{\boldsymbol{K}}\cdot\big\langle\omega - \omega Q^2 - \frac{(\nabla\omega)^2}{4\kappa^2\omega}\big\rangle/\big\langle\omega^2\big\rangle, \tag{6.11}$$

$$b_{\boldsymbol{K}} = \frac{-2\big\langle\big[\omega B + \langle\omega\rangle(B - B_{\text{avg}}) + p\big]\cos(\boldsymbol{K}\cdot\boldsymbol{r})}{K^2 + \langle\omega\rangle}, \tag{6.12}$$

where $p = |(\nabla\omega)\times\boldsymbol{Q}|\hat{\boldsymbol{z}}$. The initial values are $a_{\boldsymbol{K}} = a^A_{\boldsymbol{K}}$, the Abrikosov solution, and $b_{\boldsymbol{K}} = 0$. For the first six iterations $b_{\boldsymbol{K}}$ is kept at zero while Eqs. (6.10) and (6.11) are iterated to allow ω to relax. After the sixth iteration Eq. (6.12) is added to the sequence and Eqs. (6.10)-(6.12) are iterated until the free energy solution, Eq. (6.6), is constant to within $(1 - b)\times 10^{-13}$ between successive iterations.

Once we have calculated the local field at each point in our $N_x \times N_y$ grid[1] we can determine the probability distribution as a function of field, H, using the integral,

$$P(H) = \left(\frac{\Phi_0}{H_0}\right) \int dr \big[\delta(H - H_{VL}(r))\big], \tag{6.13}$$

where $H_{VL}(r)$ is the calculated local field due to vortices. In practice we approximate this integral with the sum,

$$P(H) = \left(\frac{\Phi_0}{H_0}\right) \sum_H \sum_{n_y=1}^{N_y} \sum_{n_x=1}^{N_x} \exp\left[-2\left(\frac{H - H_{VL}(n_x, n_y)}{dh}\right)^2\right], \tag{6.14}$$

where dh gives the width of each Gaussian contributing to the sum and is taken to be between 0.5 - 5 Gauss.

Fig. 6.4 shows the field distribution calculated using Brandt's algorithm for parameters used by [10] for a near optimally-doped YBCO aligned powder sample. Our distributions have a slightly more abrupt high-field cutoff than those of Mitrović *et al.*, however our lineshapes and widths are in agreement with theirs. We attribute the slight difference in our calculated spectra to a different programming methods and software[2].

6.4. Spatially resolved NMR in the cuprates

We now return to our discussion of how we can use NMR to study local quasiparticle behavior using the correspondence between the field profile and locations in the VL. The key variable which we would like to measure is the quasiparticle density of states (DOS)

[1]For smaller fields and κ, a $N_{x(y)}$ value of around 20 is sufficient. However, for the high fields and κ that we work with, a large $N_{x(y)} \geq 100$ is needed for good resolution.

[2]Mitrović utilized an IGOR Pro program, which she wrote herself, for VL calculations whereas we have used a Matlab program written by Brandt which we have modified to accommodate our systems.

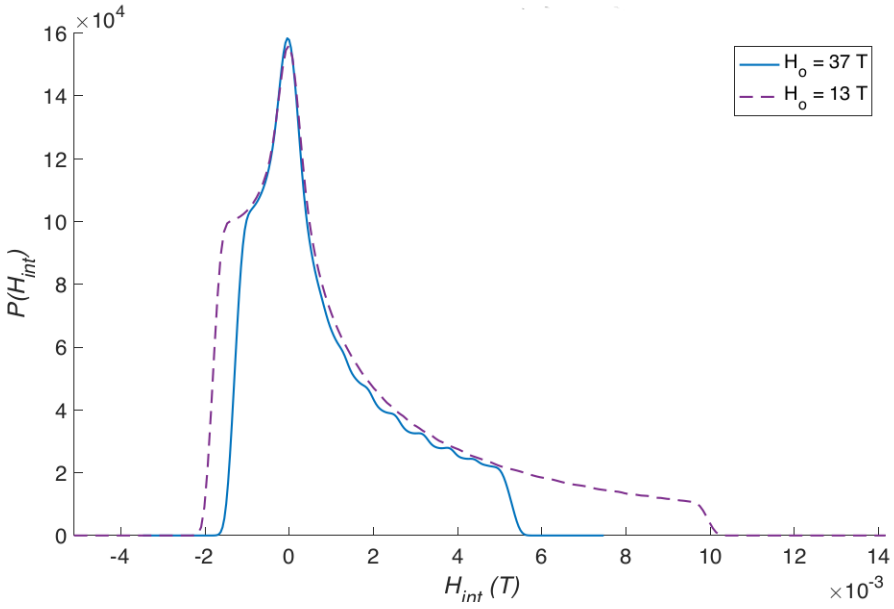

Figure 6.4. The probability distribution calculated using Brandt's algorithm for YBCO parameters at an applied field of 13 T (dashed line) and 37 T (solid line). The input parameters used are $\xi = 16$ Å, $\lambda = 1500$ Å and $\alpha = 80°$.

at the Fermi surface. We can measure the DOS at the Fermi energy, E_F, across an NMR spectrum through the spin-lattice relaxation rate. If we consider a quasiparticle scattering between two gap nodes of wavevector $\boldsymbol{k}$ and $\boldsymbol{k}'$, T_1^{-1} is proportional to the angular average of the product of the initial and final DOS at the Fermi level. If we index the initial and final quasiparticle energy states as $\alpha = i, f$, we can write the following phenomenological expression for T_1^{-1} [10],

$$T_1^{-1} \sim \langle |\epsilon - Z + D_i| \cdot |\epsilon + Z + D_f| \rangle_\epsilon. \tag{6.15}$$

Here $\epsilon = \sqrt{\epsilon_k^2 + \Delta_k^2}$ is of the order of the thermal energy[3] $k_B T$, $Z = -\frac{1}{2}\gamma_e \hbar H_o$ is the Zeeman energy, and D_α is the Doppler term which is proportional to the product $\boldsymbol{v}_{F,\alpha} \cdot \boldsymbol{p}_s$,

[3] k_B is Boltzmann's constant.

where $\boldsymbol{v}_{F,\alpha}$ is the Fermi velocity in the initial/ final scattering state, α, and $\boldsymbol{p}_s$ is the momentum of the supercurrents that circulate around each vortex core. The brackets $\langle \cdots \rangle_\epsilon$ now denote integration over the quasiparticle energy ϵ in the range $k_B T$ of the Fermi energy.

In 1993 Volovik [89] proposed that the main contribution to the DOS at E_F in the VL of a layered SC should come from quasiparticles delocalized outside the vortex core. He also predicted that the contribution of these quasiparticles at the gap nodes should be proportional to the square root of the applied field, $N(0) \propto \sqrt{(H_o/H_{c2})}$. Later theoretical work determined that the contributions of quasiparticle excitations to the DOS at E_F will have two regimes [90, 91]. In the limit of high fields and low temperatures the DOS contributions will be dominated by the Doppler shifting of quasiparticles, as Volovik originally suggested, and in this case the DOS will be proportional to $\sqrt{H_o}$. In the limit of low field and high temperature, however, the dominant contributions to the DOS will come from thermally excited quasiparticles and the Doppler term will only be appreciable near the vortex cores. In the latter case the DOS will be proportional to the applied field, $N(0) \propto H_o$.

Researchers initially tried to test Volovik's predictions using specific heat measurements of YBCO single crystals [92, 93, 94]. However, it is difficult to discriminate the contributions to the specific heat due to electronic excitations from those of e.g. phonons [93]. Additionally, the conditions of the specific heat measurements fall in the intermediate region between the high-field, low temperature and low-field, high temperature [2]. The

advantages of using spatially resolved NMR to test Volovik's theory are that, provided the resources are available, it can be done in the high-field low-temperature limit and can resolve contributions to T_1^{-1} from quasiparticles inside and outside the vortex cores.

We make note of two previous spatially resolved cuprate NMR studies performed by Mitrović [10] and Mounce [11] on YBCO powders and BSCCO single-crystals, respectively. We will leave our own results for the next chapter. Both Mitrović and Mounce used the Progressive Saturation Technique (PST), described in Chapter 3, to measure $^{17}T_1^{-1}$, inside and outside the vortex core in the mixed state of their cuprate samples at low-temperatures. Both used Brandt's algorithm to calculate the VL distribution as well as the expected $^{17}T_1^{-1}$ to compare with their experimental data. The results of their experiments are as follows.

6.4.1. YBCO NMR

Mitrović used the model described by Eq. (6.15) to analyze the planar ^{17}O NMR spectrum of an aligned powder sample of YBCO near optimal doping. She performed PST measurements at fields from 13 T to 37 T and at temperatures from 7 K to 25 K to test the field and temperature dependence of $^{17}T_1^{-1}$, and thereby the DOS at E_F, $N(0)$. These measurements revealed a monotonic increase in $^{17}T_1^{-1}$ and $(^{17}T_1T)^{-1}$ across the frequency spectrum on approaching the vortex core region. They also showed a Curie-Weiss temperature dependence of $(^{17}T_1T)^{-1}$, i.e. decreasing with increasing temperature in the highest frequency (vortex core) region. Mitrović also observed an unexpectedly large broadening of the spectral peaks at the lowest temperatures compared to the normal state

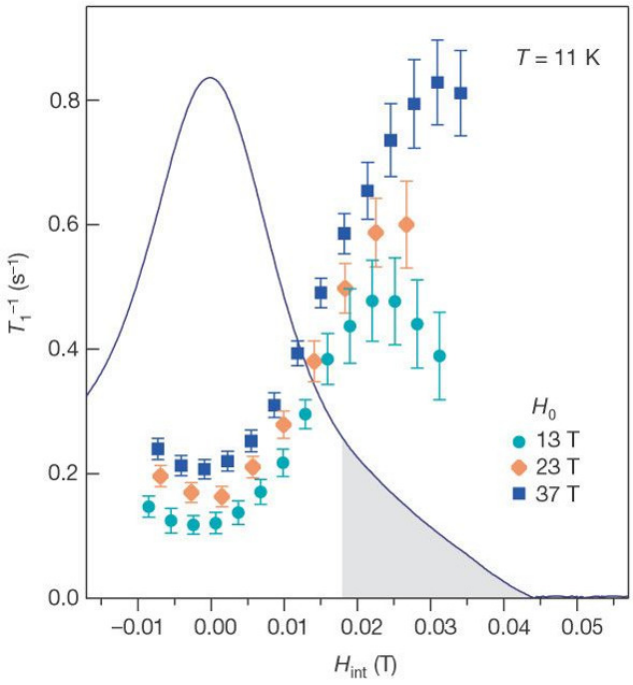

Figure 6.5. A plot of the $^{17}T_1^{-1}$ measured across the planar (-3/2 $\leftrightarrow$ -1/2) transition of a YBCO aligned powder sample by Mitrović *et al.* [10]. The shaded region of the spectrum is the region occupied by the vortex core for $H_o = 37$ T.

(100 K) spectrum.

Mitrović interpreted the above results as evidence for the presence of antiferromagnetic (AFM) correlations between quasiparticles localized in the vortex cores. This conclusion was partly based on the fact that the Curie-Weiss behavior, $1/(T_1T) \sim C/(T + T_N)$ for some characteristic temperature T_N, which the group observed in the planar ^{17}O spectrum, is a property of AFM materials. Additionally, because the spectral broadening at low temperatures was too large to be accounted for by random VL disorder, as calculated

by Brandt [95], Mitrović proposed that the extra broadening could be due to the additional magnetic field contribution arising from AFM moments in vortex cores.

There are a few caveats with the YBCO data and conclusions drawn from them. Firstly, the planar ^{17}O satellite, at which the NMR measurements were performed, overlaps with the $(\pm 5/2 \leftrightarrow \pm 3/2)$ ^{17}O satellite on the low-frequency side at low temperatures which adds an extra source of error in the $^{17}T_1^{-1}$ data. The overlap also invalidates any $^{17}T_1^{-1}$ measured at the low-frequency of the spectrum, so the low-field relaxation behavior is unknown. Additionally, the samples were aligned powders which are inherently disordered and have a higher density of pinning centers which can affect the physics being measured with NMR. Therefore, we wish to repeat Mitrović's methods to study other cuprates under the assumption that some of the physics revealed by YBCO will be universal to all of these compounds. Mounce attempted to do this with the highly anisotropic cuprate, $Bi_2SrCa_2Cu_2O_{8+\delta}$ (BSCCO).

6.4.2. BSCCO NMR

Mounce [11, 12] found that the ^{17}O NMR spectrum of over-doped BSCCO single crystals in the VL state (Fig. 6.6) behaved differently from that of near optimally-doped YBCO aligned powders. Mounce's spatially resolved PST experiments revealed a $^{17}T_1^{-1}$ which varied as a non-monotonic function of the field across the NMR spectra, increasing at the lowest and highest fields and decreasing at the peak of the spectrum. This led to a dip in the $^{17}T_1^{-1}$ at the part of the spectrum corresponding to the VL saddle point. This behavior could not be attributed to the physics (field fluctuations and quasiparticle

dynamics) of the VL alone.

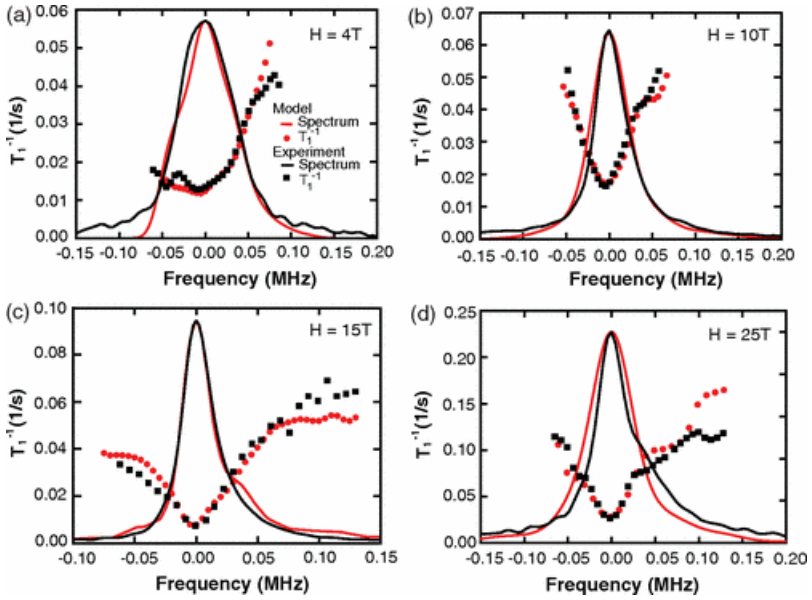

Figure 6.6. The $^{17}T_1^{-1}$ behavior reported by Mounce *et al.* in [11] for a single-crystal sample of BSCCO. The spectrum and $^{17}T_1^{-1}$ calculated from the SDW + VL model are shown in red and the experimental results are shown in black for four different fields.

To resolve this issue, Mounce proposed that the NMR spectrum was influenced by a second field arising due to a spin density wave (SDW) with its center at the vortex core. This notion was based on the results of several STM experiments [96, 97, 98] showing that vortices induce a "checkerboard" pattern in the local DOS with a spatial period of about four times the VL spacing. The BSCCO spectra were fit to a field distribution that was modeled as the sum of the VL field calculated from GL theory and a SDW contribution which produced a good fit to the experimental data. At low fields ($H_o < 4$ T), Mounce found that the NMR spectrum and $^{17}T_1^{-1}$ were dominated by the field fluctuations of the VL. At fields above 5 T the SDW field contributions become comparable to those of the

VL and at high fields ($H_o \geq 15$ T) the SDW contribution to the field dominated the local field distribution.

In addition to the contribution of the SDW to the local magnetic field, Mounce *et al.* also observed a field-induced narrowing of the ^{17}O linewidth at high fields followed by a slight broadening as the field was increased further [12]. The group was able to account for this apparent field-induced instability by considering the vortex cores of BSCCO to carry a charge of $\sim 2 \times 10^{-3}e$, where e is the magnitude of the electron charge. The exact value of the effective charge per vortex depends on doping. The fact that vortices should carry charge had been theoretically predicted [99, 100] but the experimental evidence for vortex charging was not universally accepted. Mounce *et al.* used a model system of charged Abrikosov vortices and calculated the energy cost of displacing a stack of vortex pancakes in the *ab*-plane relative to the Abrikosov lattice. The group used Clem's [101] model to calculate the magnetic energy cost of the displacement and used a periodic lattice of charges to calculate the electrostatic energy cost via the Coulomb potential of the system.

In general, the magnetic interaction between vortices in the same plane is repulsive and the interaction between vortices in adjacent planes is attractive. The latter interaction, known as Josephson coupling, is very weak at high fields and is therefore ignored in the calculations discussed here. In contrast to the magnetic interaction, the electrostatic interaction between charges on different planes increases at short range [12]. Mounce found that there is a field for which the electrostatic and magnetic interactions between

vortices balance, leading to a structural instability of the VL, assuming an effective charge per vortex of 2.1 and 2.5 $\times 10^{-3}e$ for each over-doped single crystal sample.

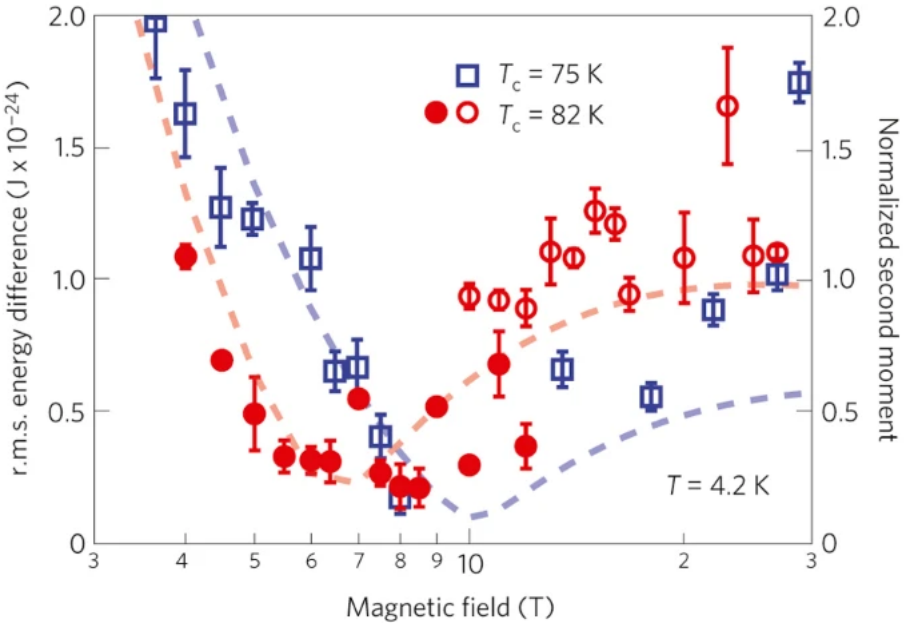

Figure 6.7. From reference [12]. The calculated r.m.s. energy cost for vortex displacements (left axis) along with the normalized second moment (right axis) for three over-doped single crystal BSCCO samples. The sample T_c's are given in the legend.

The plot of the calculated root-mean-squared (r.m.s.) energy cost for vortex displacements, assuming a certain charge per vortex, as a function of magnetic field is shown in Fig. 6.7 (dashed lines). The markers show the second moment (essentially the square of the ^{17}O NMR linewidth) measured for three over-doped single crystal samples of BSCCO. Note that the markers fit well to the dashed lines, indicating that the minimum linewidth corresponds to the r.m.s. energy difference at which the electrostatic and magnetic vortex

interactions are equal. This minimum is where the VL is unstable.

Mounce suggested that, because of the prevalence of the SDW and charge/field-induced instability in BSCCO at high fields as well as its high anisotropy and short coherence length, this compound may not be ideal for studying vortices with NMR. He suggested that Hg1201 may be better suited for such studies due to its longer coherence length (smaller H_{c2}), simpler crystal structure and smaller anisotropy. From our spatially resolved NMR results on Hg1201 single crystals in the mixed state, which we discuss in the following chapter, we find that this may not be the case.

6.5. Conclusions

The vortex lattice (VL) forms in a type II SC when the thermal fluctuations are overpowered by the electromagnetic interactions between circulating vortex supercurrents, i.e. at low temperatures. The VL creates a distinct local magnetic field which can be detected with NMR. The well-defined relationship between points in the field profile and points on the VL makes it possible to study the physics of quasiparticle excitations in specific regions of the VL. Previous attempts to measure $^{17}T_1^{-1}$ across the NMR spectra of YBCO and BSCCO have revealed possible AFM correlations in the nodal quasiparticle excitations in YBCO, but not in BSCCO, where a SDW field is dominant at fields greater than 4 T and vortex charging effects create a field-induced structural VL instability. In the next chapter we will discuss our own NMR results and compare them with the theory as well as previous data.

CHAPTER 7

Vortices in Hg1201

Whereas there have been a plethora of investigations of the VL state of cuprates such as YBCO and BSCCO, the data for Hg1201 is scarce. One key reason for the lack of available data on Hg1201 single crystals in particular is that until as recently as 2006 researchers were unable to grow the sizeable single crystals of the cuprate needed for experiments such as SANS [102]. Recent breakthroughs in crystal growth techniques [60] have led to a slight increase in the available data on Hg1201 single crystals, but the data is still scarce compared to those available for other cuprates. Here we will present some of the available data from the literature as well as from our own findings on the observation, or lack thereof, of the VL in Hg1201 single crystals.

7.1. SANS results and the 2D limit

Of the avaiable data there is a notable SANS study by Li *et al.* [103] on two near optimally-doped single crystals of Hg1201 with a T_c of 94 K and a ΔT_c of less than 2 K as measured by magnetometry in reference [102]. The two crystals (60 mg and 90 mg) were co-aligned on a Si wafer and their c-axes were within 1° of the incident neutron beam. The sample was field-cooled from room temperature to 2 K and the SANS signal was measured from 2 K to room temperature. This procedure was repeated for fields of $B =$ 0.10, 0.15, 0.20, 0.25, 0.30 and 0.35 T.

Li *et al.* used the azimuthal intensity distribution of the momentum transfer, q, to determine that the VL at 0.10 T $\leq B \leq$ 0.35 T was undistrorted and triangular [103] with an opening angle of $\alpha = 60°$. The low-field triangular VL geometry has also been observed in YBCO [104, 105], which has been shown to undergo a structural transition from a triangular VL at $B < 6.7$ T to a square VL at higher fields. In Hg1201, however, Li *et al.* found that the scattered neutron intensity diminished rapidly with increasing field and was completely undetectable for $B > 0.35$ T. The group attempted measurements at fields up to 4.0 T to see if the VL signal re-appeared as the field strength was increased but did not observe such a re-emergence at higher fields. Therefore, the structure of the VL in Hg1201 at high fields has yet to be imaged directly.

The authors of reference [103] proposed that the reason for their loss of signal at $B \geq 0.4$ T was that the vortices in Hg1201 become disordered along the c-axis, causing the VL in each CuO_2 layer to become decoupled thereby reducing the characteristic spatial variation of the local magnetic field detected by SANS. These 2D ordered vortices are know as "vortex pancakes" and the limit in which this de-coupling along the c-axis occurs is known as the "2D limit." Prior to the study by Li *et al.*, this disappearance of the SANS signal had been seen by Cubitt *et al.* [106] in the highly anisotropic cuprate, $Bi_{2.15}Sr_{1.95}CaCu_2O_{8+x}$ (BSCCO). In the case of BSCCO the group found that the signal disappeared at a field of 0.1 T.

One widely quoted phase diagram used to describe this 2D melting transition in highly anisotropic superconductors such as BSCCO is that described by Glazman and

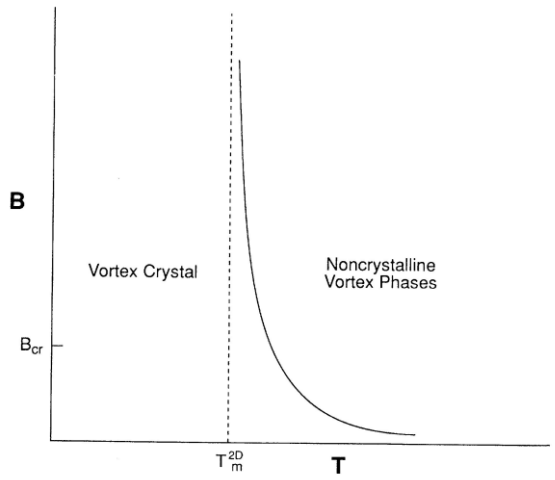

Figure 7.1. The B vs T VL phase diagram from reference [13] showing the field dependence of the VL melting temperature, represented by the solid line. The dashed line represents the 2D melting temperature, T_m^{2D}, the melting temperature in the limit that the VL in each CuO_2 layer is completely de-coupled from those in adjacent layers.

Koshelev in reference [13]. This B vs T phase diagram (shown in Fig. 7.1) shows the field-dependence of the VL melting temperature as asymptotically approaching its so-called "2D limit," at a temperature, T_m^{2D}, which is given by,

$$T_m^{2D} = \left(\frac{A}{8\pi\sqrt{3}}\right)\frac{d\Phi_o^2}{k_B(4\pi\lambda_{ab})^2}. \tag{7.1}$$

In the above expression d is the distance between CuO_2 layers, Φ_o is the magnetic flux quantum, k_B is Boltzmann's constant and λ_{ab} is the penetration depth in the ab-plane. In Hg1201 $d = 9.6$ Å, which is also the c-axis lattice constant and λ_{ab} has been measured [107] to be 1620 ± 50 Å in under-doped crystals with a T_c of 96 K. The constant A has been calculated to be ~ 0.61 from the Lindemann criterion [108, 15, 109]. Interestingly, plugging these values –choosing $\lambda_{ab} = 1620$ Å– into expression (7.1) gives a T_m^{2D} of approximately 10 K ($T_m^{2D} = 10.06$ K), which is the temperature at which we see an onset

of the exponential relaxation, $^{17}T_{2e}^{-1}$ (see Fig. 5.13). It is unclear from our data whether this is physically meaningful or coincidental.

The *crossover field*, $B_{\rm cr}$, separates the regions of the phase diagram of 2D and 3D melting. Glazman and Koshelev's calculations center around a phenomenological parameter, γ, the mass anisotropy, defined as, $\gamma \equiv \lambda_c/\lambda_{ab}$, where λ_c is the penetration depth measured along the crystal c-axis. In performing their calculations the authors assume that the anisotropy is large, $\gamma \gg 1$. Glazman and Koshelev estimate the crossover field to be,

$$B_{\rm cr} \approx 2\pi\left(\frac{\Phi_o}{\gamma^2 d^2}\right)\ln(\gamma k_{max} d), \tag{7.2}$$

where k_{max} is given by,

$$k_{max} \sim \frac{1}{\xi_{ab}}\left(1 + \frac{T(4\pi)^2\lambda_c^2 d}{2\Phi_o^2\xi_{ab}^2}\right)^{-1/2},$$

where ξ_{ab} is the in-plane coherence length and T is the temperature. Note that the expression for $B_{\rm cr}$ (7.2) is estimated under the assumption that the Josephson coupling between layers dominates over the line tension of a single vortex, i.e. $\gamma < \lambda_{ab}/d$ [13]. Li *et al.* estimated this crossover field as $B_{\rm cr} \sim \Phi_o/(d\gamma)^2 \approx 1.4$ T for their measured[1] $\gamma = 40$. These authors also posited that the 2D vortices in the same layer should be pinned together by a small density of pinning centers. This is in contrast to vortices being pinned individually.

[1]Other groups have reported measured values of $\gamma \sim 27 - 30$ [107, 14], which puts $B_{\rm cr}$ closer to 3 T.

In a recent study by Eley *et al.* [14] on a high-quality single crystal of Hg1201 the authors used magnetization measurements to show that the vortex dynamics in Hg1201 would be 2D at all fields and temperatures in the mixed state. The group used measurements of the rate of thermally activated vortex motion (creep) to extract the vortex dynamics over a range of temperatures and fields from 0 to 7 T. They found behavior consistent with a low-field and low-temperature vortex glass state characterized by collective creep of large bundles of vortex pancakes. As the field increased the vortex state remains glassy and the size of the 2D vortex bundles involved in creep decreases. Their results are summarized in their proposed vortex phase diagram, which we include here for reference.

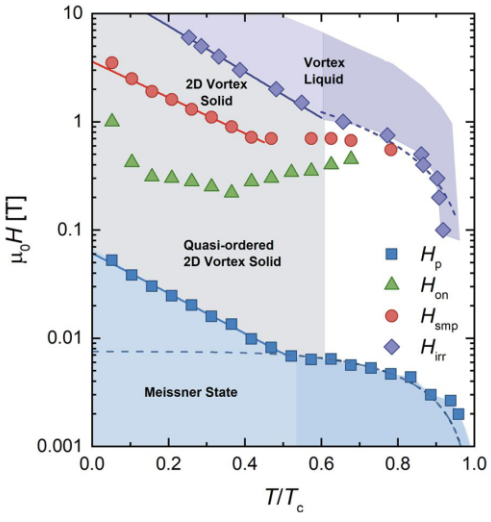

Figure 7.2. The proposed vortex dynamics phase diagram for Hg1201 from [14]. If the boundaries are extrapolated to high fields this would put our sample at 5 K and 14 T in the "vortex liquid" state.

This study provides further evidence that the vortices in Hg1201 will be decoupled along the c-axis such that the VL has a 2D character at all fields that we use in NMR. This is also in agreement with what we see in one of our under-doped Hg1201 single crystals, UD81, as we show later in this chapter. This under-doped crystal also happen to be provided by one of the authors of reference [14]. We also note that the proposed phase diagram shown in Fig. 7.2 is based on low-field data which the authors have extrapolated to 10 T. If the vortex liquid-to-solid boundary is extrapolated to higher fields it would indicate that our Hg1201 sample is in the "vortex liquid" state at fields of 14 T and above at a temperature of 5 K. While this is a possibility, we also consider that the boundaries may deviate from the low-field behavior at higher fields. We also note that the absence of vortex pinning, which is indicated by a lack of irreversibility, does not necessarily imply the system is a vortex liquid.

7.2. Low-temperature ^{17}O NMR lineshape

If we recall the relation, $\omega = \gamma H$, between the frequency that appears in an NMR spectrum and the magnetic field, H, surrounding the nuclei, it is clear that the frequency-domain NMR spectrum can be easily converted to a field-domain spectrum using the nuclear gyromagnetic ratio. This means that when a system forms a VL and the nuclei are only affected by the local field produced by the quasi-static vortices, the NMR spectrum will essentially be a histogram of local magnetic fields produced by the VL. Of course, as we noted in Chapter 2, the frequency of an NMR signal will be affected by hyperfine interactions as well as local fields which will complicate the interpretation of an NMR

spectrum as a field distribution in the VL state.

Fortunately, in Hg1201 the Knight shift at the O(2) site has been shown to be negligibly affected by the hyperfine field of the CuO_2 plane [62, 4]. A Knight shift analysis shows that the only appreciable contribution to ^{17}K at the O(2) site is K_{dia}, which is small and onsets below T_c. This makes the O(2) site a perfect candidate for studying the VL state through NMR because its NMR spectrum should directly correspond to the local field distribution at the nucleus. Additionally, if we recall the 90 K ^{17}O NMR spectrum shown in Fig. 4.3 we see that the O(2) satellites (B and C) are well separated in frequency (field) space so we will not have any contributions to our O(2) spectrum from overlapping peaks corresponding to other sites in the Hg1201 unit cell.

In principle the location of the O(2) site in the NMR spectrum as well as its lack of coupling to the electronic structure of the CuO_2 plane makes this site an ideal candidate for spatially-resolved NMR of the VL. However, our ability to study the VL with NMR also depends on the ordering of the VL between the stacked CuO_2 layers. If the system is in the 2D limit, as Li *et al.* and Eley *et al.* predicted, and the VL is not sufficiently ordered along the *c*-axis, the VL will not produce a distinct field profile and the NMR spectrum will appear no different from that of the vortex liquid state. Fig. 7.3 shows the O(2) high-frequency ($\pm 3/2 \leftrightarrow \pm 1/2$) satellite at 20 K (black) and 85 K (blue) of the UD81 and UD79 samples at 14 T. Neither of the spectra show the significant broadening at low temperature that we expect for a VL spectrum compared to the normal state spectrum

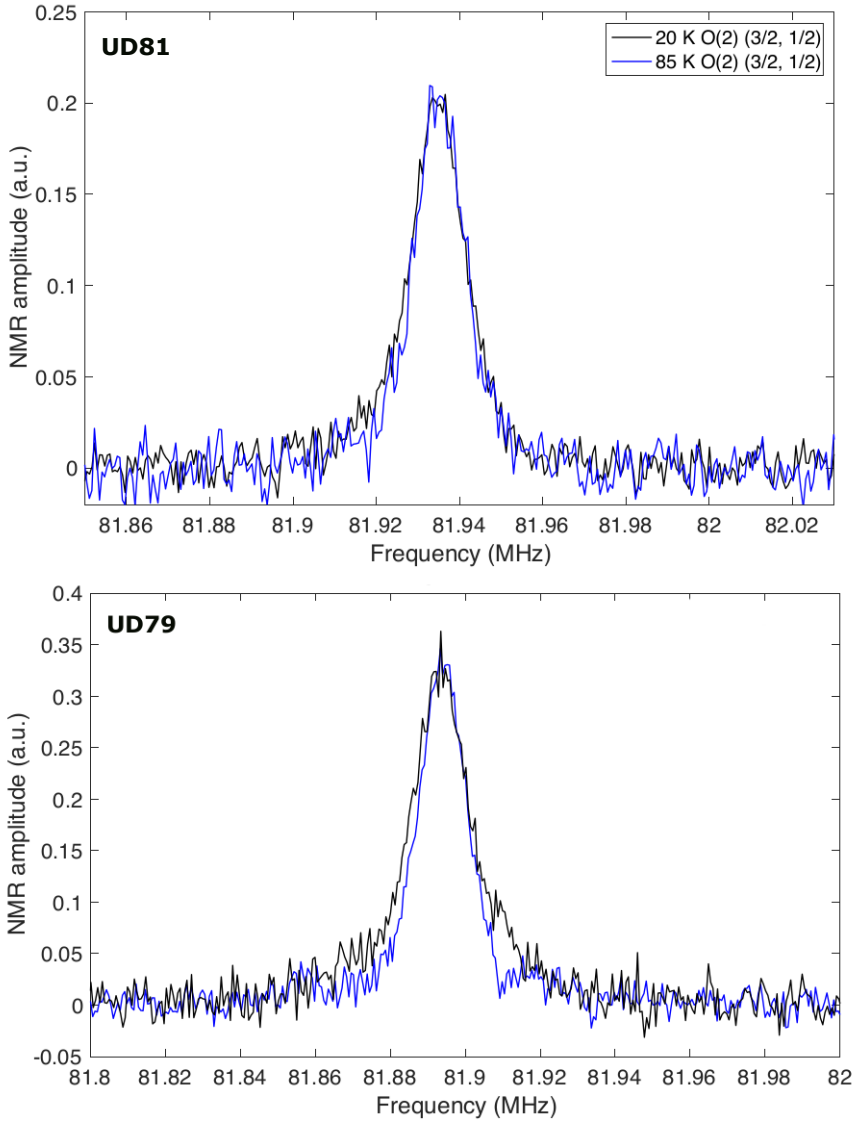

Figure 7.3. The O(2) high-frequency ($\pm 3/2 \leftrightarrow \pm 1/2$) satellite at $T = 20$ K (black) and $T = 85$ K (blue). Both UD81 (top) and UD79 (bottom) spectra were measured with $H_o \| \, c$ in a field of 14 T.

(85 K).

It is possible that the absence of broadening at 20 K under these conditions is due to the fact that the VL melting temperature, T_m, is lower than 20 K at 14 T. Fig. 7.4 shows

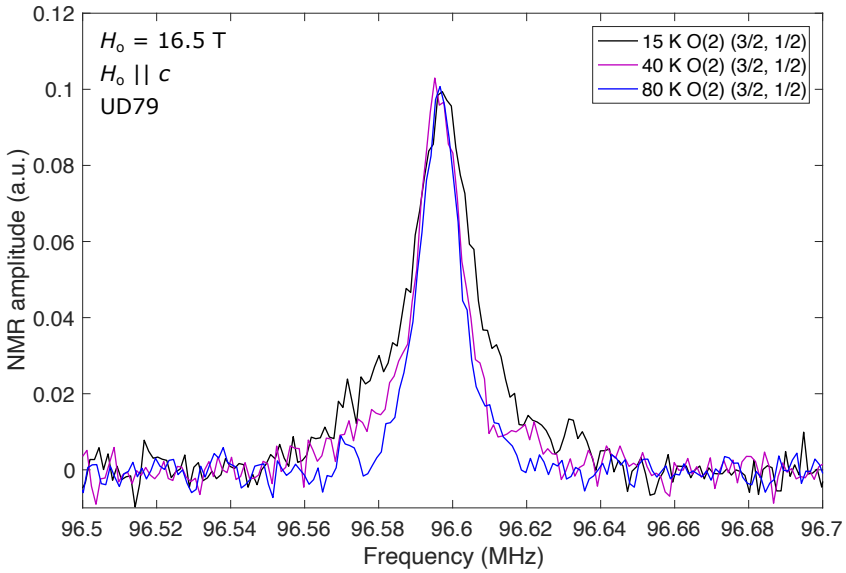

Figure 7.4. The NMR spectrum of the UD79 sample in $H_o = 16.5$ T, $H_o \parallel c$ at three different temperatures.

a spectrum measured by Lee of the UD79 sample in an applied field of 16.5 T at $T =$ 80 K, 40 K and 15 K. The 15 K spectrum (black) is significantly broadened compared to that measured at 40 K (magenta) and 80 K (blue) which indicates that the system has formed a VL at this field and temperature. On the other hand, the 40 K and 80 K spectra do not appear to be significantly different despite 40 K being below T_c and 80 K being just above T_c.

One might note that there appears to be a bit more broadening in the 20 K spectrum of the UD79 sample compared to the 85 K spectrum than we see in the UD81 sample. However, if we compare the UD79 spectra at 16.5 T (Fig. 7.4) to those at 14 T (Fig. 7.3) we see that the modest difference between linewidths at 20 K and 85 K in 14 T is much smaller than we expect for a low-temperature VL spectrum compared to a vortex liquid

or normal state spectrum. From this data it appears that there is a VL that forms at a higher temperature in the UD79 sample than in the UD81 sample.

7.2.1. Field and temperature independence of linewidth

In order to further investigate the absence of the broadening of the spectrum in our UD81 sample we have performed high-field and low temperature measurements at the NHMFL using the setup discussed in Chapter 3. We measured the spectrum of the high-frequency O(2) ($\pm 3/2 \leftrightarrow \pm 1/2$) satellite at various fields from 14 T to 29 T. For fields below 20 T the exact H_o value was measured using an ^{27}Al reference signal from an Al powder set in epoxy inside the sample holder. For $H_o > 20$ T the field value was estimated from the ^{17}O central transition. The temperature fluctuations were less than 0.1 K throughout all our measurements at the NHMFL and less than 0.2 K for our measurements at NU[2].

Figure 7.5 shows the temperature dependence of the full-width at half-maximum (FWHM) of a Lorentzian fit to the O(2) satellite (top) at fields of about 14 T. We also show (bottom) the normalized FWHM of the corresponding O(1) satellite at 19 T where the fit is to a Gaussian. The open markers represent data points measured at the NHMFL and the solid markers are data measured at NU. The linewidths are normalized by the applied field. Clearly, there is a negligible change in the linewidth of both the O(1) and O(2) spectra upon decreasing temperature. In the case of a 3D ordered vortex lattice we expect a broadening on decreasing the temperature through the VL melting

[2]This is excluding the 20 K data points measured at NU where the temperature fluctuations were about 1 K.

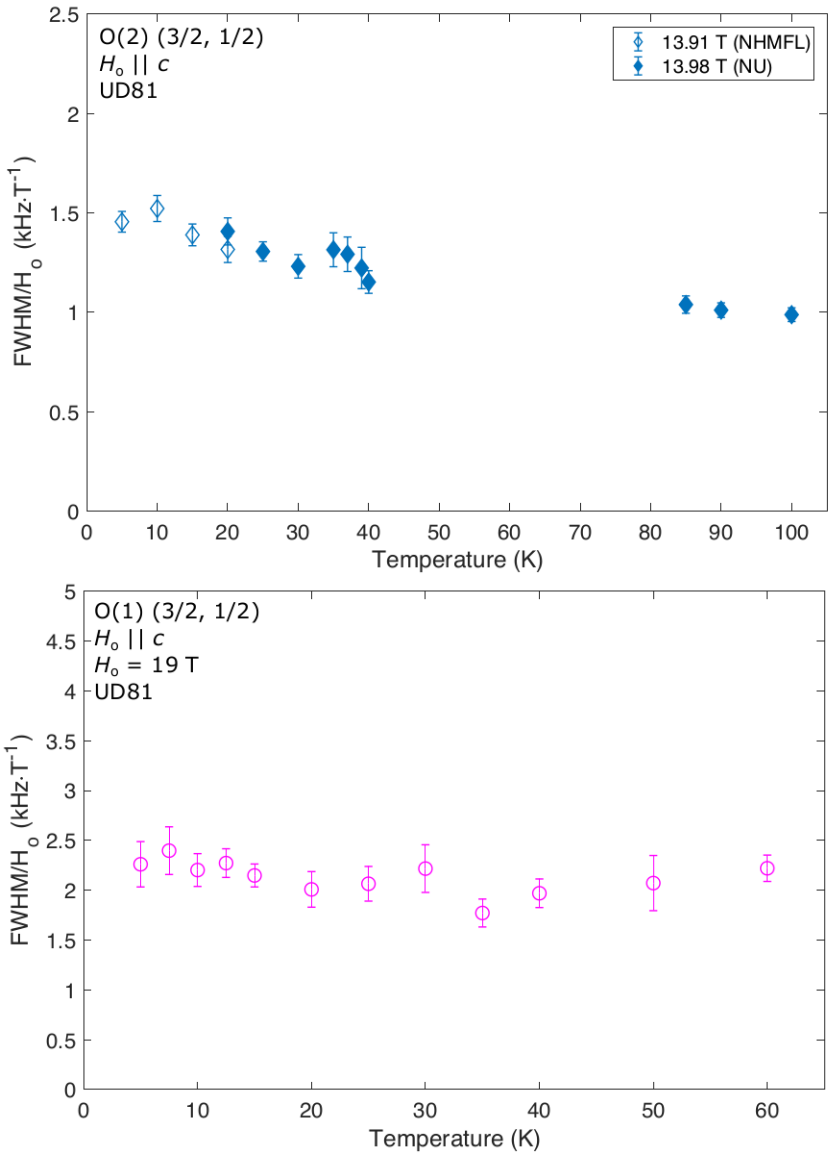

Figure 7.5. The top plot shows the full-width at half-maximum (FWHM) of a Lorentzian fit to the O(2) satellite spectra as a function of temperature at 14 T normalized by the applied field. The bottom plot shows the Gaussian FWHM temperature dependence of the corresponding O(1) satellite at 19 T.

temperature. As an example, we show (Fig. 7.6) the measured linewidth (normalized by H_o) recorded by Chen *et al.* [15] for an over-doped BSCCO single crystal. Note that the

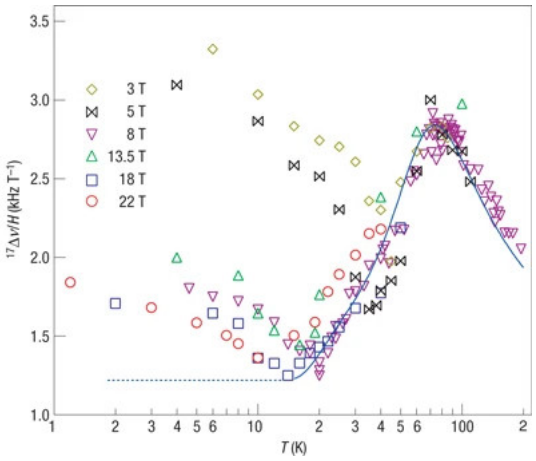

Figure 7.6. From reference [15], the linewidth (divided by H_o) of the measured ^{17}O spectra as a function of temperature of a BSCCO over-doped single crystal sample. The curve is a theoretical dependence of the linewidth on background magnetic contributions, applied field and Knight shift.

low-temperature broadening is much greater than what we see (Fig. 7.5) for UD81.

In order to compare our data to that of another under-doped sample we have re-analyzed data measured by Lee on the UD79 sample at $H_o = 16.5$ T. The results are displayed in Fig. 7.7. Both satellites correspond to the first high-frequency ($\pm 3/2 \leftrightarrow \pm 1/2$) transition. The plot shows a negligible change in the O(1) linewidth upon changing the temperature whereas the O(2) linewidth does appear to increase below $\sim$40 K. This is the same O(2) data set whose spectra are displayed in Fig. 7.4. Although there is slightly more broadening in the O(2) spectrum in the UD79 sample compared to the UD81 sample, the difference is fairly modest and neither sample shows a temperature dependence in the O(1) linewidth or shape.

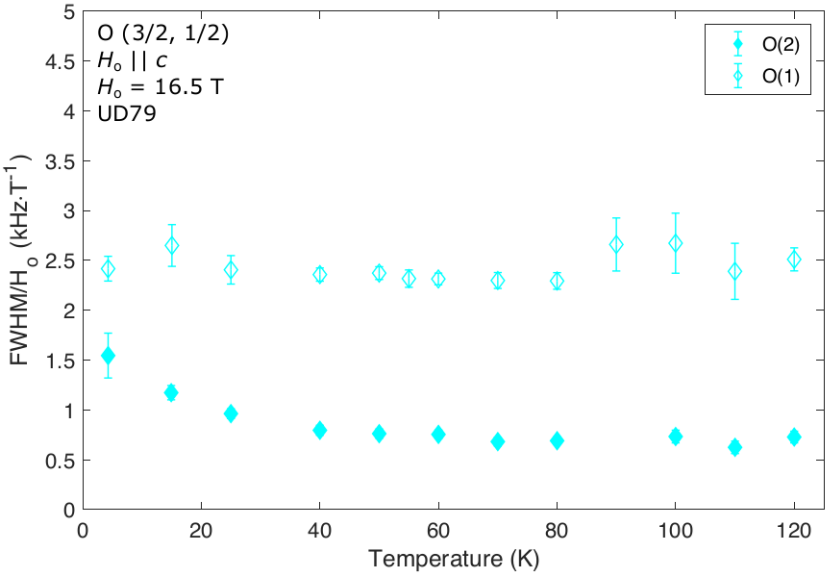

Figure 7.7. Data measured by Lee for the UD79 sample at 16.5 T with $H_o \parallel c$.

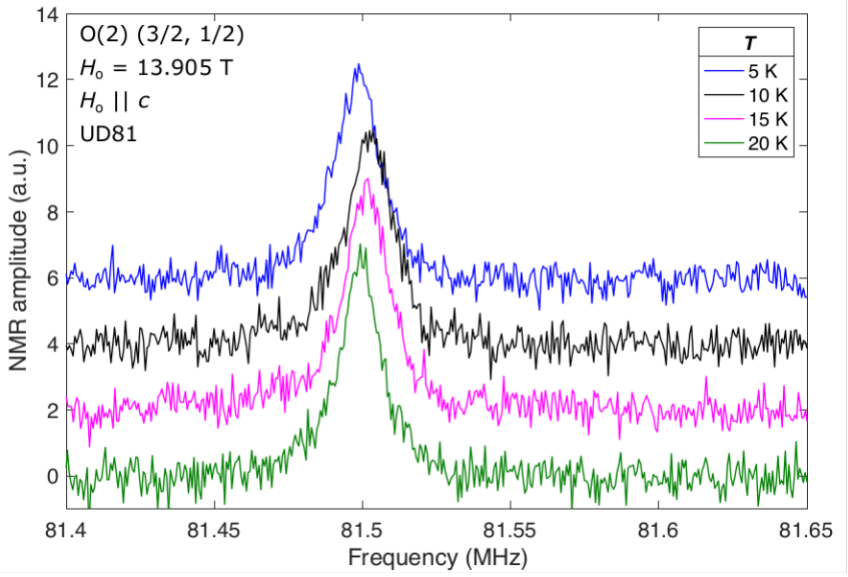

Figure 7.8. A plot of the O(2) ($\pm 3/2 \leftrightarrow \pm 1/2$) high-frequency satellite spectra measured at 13.9 T at various temperatures. The peak frequencies have been normalized to 13.905 T according to the exact field values measured by ^{27}Al NMR such that any difference in peak frequency must be due to a Knight shift.

In the case that a VL is formed on decreasing the temperature below a melting temperature, T_m, the spectrum should also develop an asymmetric shape like the calculated VL field distribution shown in Fig 6.4. In Fig. 7.8 we show the O(2) spectra to which we performed the Lorentzian fit in Fig. 7.5. We can see that, for our UD81 sample, in addition to there not being an increased broadening upon lowering the temperature we also do not see any evidence of a change in the lineshape to indicate the formation of a VL. The same can be argued of the UD79 results shown in Fig. 7.4. Although in the UD79 case the spectrum does appear slightly broader at the lowest temperature, it does not appear to have changed shape appreciably.

In addition to to lack of observable temperature dependent broadening, we also do not see any field-induced broadening or narrowing of the O(2) satellite. In Fig. 7.9 we show the field dependence of the linewidth of the O(2) ($\pm 3/2 \leftrightarrow \pm 1/2$) satellite at fields from 14 T to 29 T. Note that there is no discernible change at any field. We also show the lineshape for three different fields in Fig. 7.10 to illustrate the negligible change in the shape of the spectra at different fields. The peak of each spectrum in Fig. 7.10 were normalized by subtracting the measured $\nu_Q = 1.227$ MHz as well as the measured Larmor frequency, $\omega_L =^{17} \gamma H_o$, from the peak frequency.

The lack of field-induced broadening is an interesting result because if the spectrum were a perfect VL field distribution (see Fig. 6.4) the linewidth would narrow upon increasing the field since the increase in vortex density would create a larger region of overlapping supercurrents that would cancel and result in a smaller spatial variation in

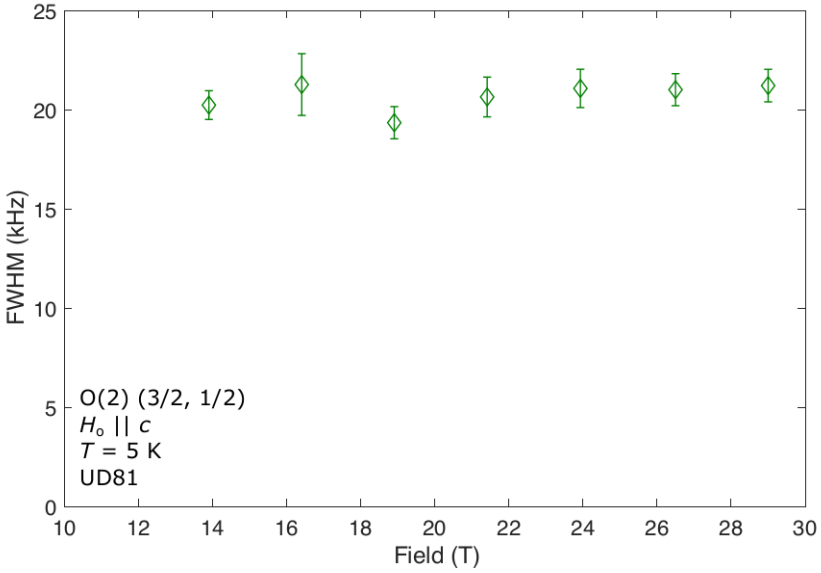

Figure 7.9. The FWHM of the Gaussian fit to the O(2) spectrum of the UD81 sample at $T = 5$ K.

the local fields. On the other hand, even in the absence of a VL one would expect there to be a spectral broadening upon increasing the field due to an increase in the field variations on a local scale due to structural defects or impurities.

The fact that we do not see any change in the width or lineshape of our O(2) spectra in our UD81 sample for any field or temperature is further evidence that this sample is very clean, i.e. free of any defects to which vortices could be pinned or that would cause an amplified field gradient to appear at high fields. It is also further evidence that if there is a VL formed in the CuO_2 planes it must be highly disordered along the c-axis such that the vortices are 2D pancakes and are completely uncorrelated along the c-axis. Such disorder would make the local field profile of the VL less well resolved since it will be that of many 2D vortex pancakes superposed on one another without being aligned by

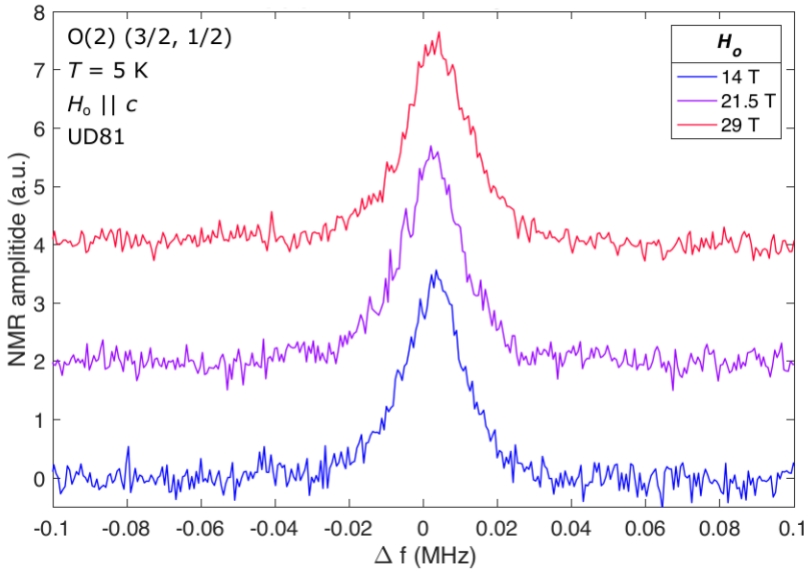

Figure 7.10. The O(2) satellite transition at three different fields. The exact field values were measured to be $H_o = 13.905$ T and 21.416 T, using the ^{27}Al signal and $H_o \approx 28.95$ T using the central ^{17}O transition. The horizontal axis, Δf, represents the shift in frequency from $\omega_L + \nu_Q$ as described in the text.

Josephson coupling.

While we have not measured the field-dependent broadening at the O(1) site of the UD81 sample directly, we have measured the central transition which is an overlap of the O(1) and O(2) sites. At temperatures below 50 K the two peaks are indistinguishable and form a single peak. In Fig. 7.11 we show our data for the FWHM of a Gaussian fit to the central transition at $T = 5$ K for our own UD81 sample (top) as well as the UD74 sample at $T = 4$ K (bottom). The data on the UD74 sample was measured by Mounce and re-analyzed for this work. Note the broadening of this peak at high fields for both samples. This broadening must originate in the O(1) site since we have shown that the O(2) spectrum does not broaden with increasing field. This field-induced spectral

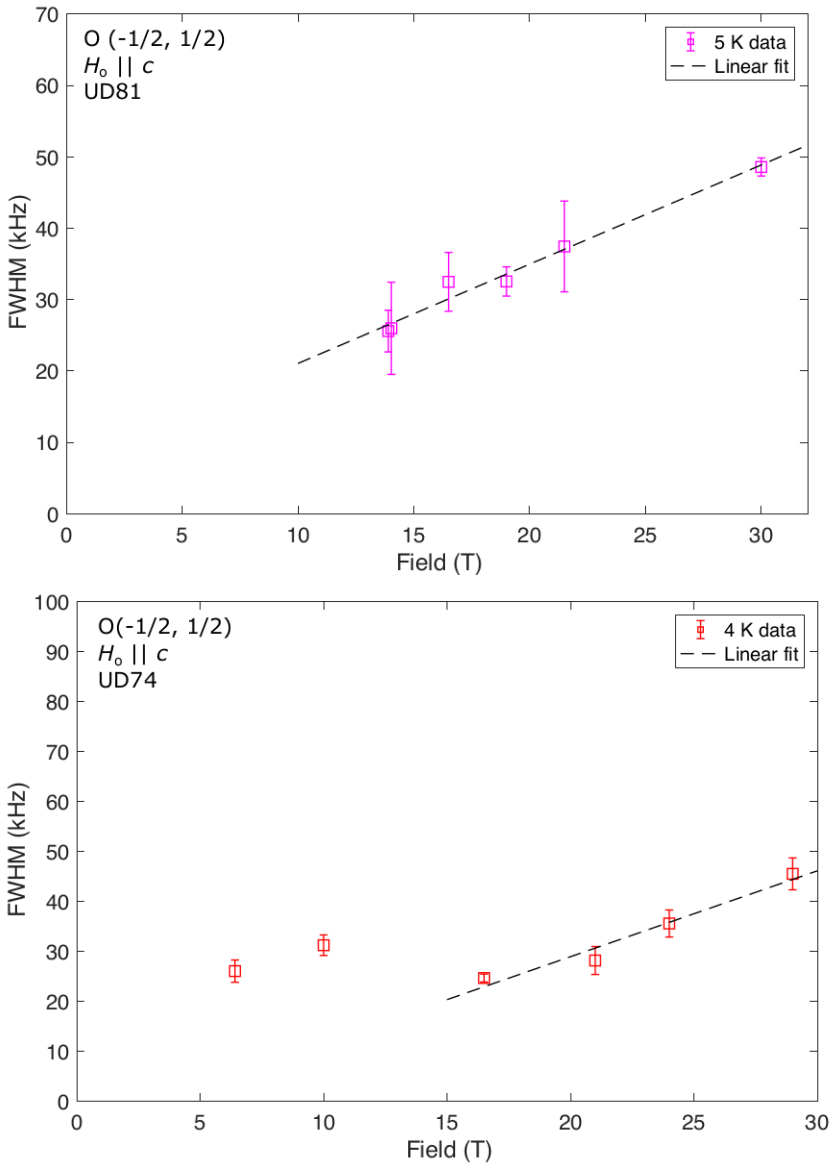

Figure 7.11. The (Gaussian) FWHM of the central ^{17}O transition measured at 5 K (UD81, top) and 4 K (UD74, bottom). The dashed lines are linear fits to the data in the region of linear behavior.

broadening at O(1) is evidence that there is a contribution to the field in the CuO_2 plane originating from a source other than a VL.

It is possible, of course, that the lack of broadening and static lineshape that we observe in the O(2) spectra are manifestations of the system remaining in the vortex liquid state even at temperatures as low as 5 K. If this is the case our observation of $^{17}T_{2e}^{-1}$ (see Fig. 5.13) increasing below 10 K must be due to some other mechanism than the increased presence of stationary vortices. It may be the case that the VL is present but that there is some additional field that dominates the spectrum as was the case with the SDW in BSCCO as discussed in 6.4.2. As we mentioned in Chapter 5, more data is needed to confirm the source of this additional relaxation mechanism at low temperatures. It is also possible that a VL is present, but that the force applied by an rf pulse is enough to overcome the pinning forces and destroy the order. In this case, NMR is not a good method for studying the VL in the under-doped Hg1201 system.

7.2.1.1. Vortex charge. Another possibility is that a charge-induced instability is affecting the linewidths of our ^{17}O spectra as was also the case with BSCCO [12]. This instability is due to the vortices carrying a charge trapped in the vortex core creating a Coulomb interaction that competes with the magnetic interaction between vortices. This vortex charge is a result of the difference in chemical potential between the superconducting and normal state at the vortex core [110, 99] as well as the presence of particle-hole asymmetry [100].

The theory of vortex charging is relatively well established and has been discussed in the context of Hall effect experiments [111, 112] in which researchers observed a change in the sign of the Hall coefficient in high-temperature SCs below T_c. Blatter *et al.* [100]

used BCS theory to calculate the charge, Q, trapped in the core of a type II SC in the presence of metallic screening. They found that the accumulated charge in the vortex core per layer is,

$$Q = \frac{2ek_F d}{\pi^3}\left(\frac{\lambda_{\mathrm{TF}}}{\xi}\right)^2 \frac{d\ln T_c}{d\ln \mu}, \tag{7.3}$$

where e is the magnitude of the electron charge, k_F is the Fermi wavenumber, d is the interlayer distance, μ is the chemical potential and λ_{TF} is the Thomas-Fermi screening length.

In further theoretical work [113, 114, 115] researchers began incorporating antiferromagnetic (AFM) order, d-wave superconducting order, doping concentration and Coulomb interactions into their models of vortices in cuprate SCs. Chen *et al.* [113] found that the vortex charge had a strong doping dependence. Their model revealed that the vortices in over-doped systems carried a net positive charge and displayed no antiferromagnetism whereas the vortices in under-doped carried a negative charge and displayed AFM order. This result is in disagreement with the experimental NMR results of Kumagai *et al.* [116] in which they found the opposite sign of the vortex charge in one under-doped and one over-doped YBCO aligned powder sample.

It should be noted that Mounce's BSCCO samples, in which he observed a field-induced instability manifested in a minimum spectral linewidth (see Fig. 6.7) at a certain field, were over-doped. If the theory is correct in that under-doped cuprates will have AFM ordered cores in addition to carrying a vortex charge, the manifestation of vortex

charge in these systems may be different from that seen in over-doped crystals. It should also be noted that Mounce did observe [11] the low-temperature broadening signature of VL formation in his BSCCO crystals whereas we did not observe such a broadening in our UD81 sample, as discussed above. Therefore, more data is needed at low fields and low temperatures to determine if the vortex core charge in under-doped Hg1201 crystals creates a field-induced VL instability.

7.2.2. Spatially-resolved NMR in Hg1201

As we touched on in the previous chapter, the regions of the NMR spectrum can correspond to regions in real space when the system is a vortex solid ordered along the c-axis or a 2D (film) type II superconductor with $H_o \parallel c$. In this case the highest frequency (field) portion of the NMR spectrum will correspond nuclear spins within the vortex core, which is an area of interest in condensed matter physics. In particular, because quasiparticles are present in a d-wave SC down to the lowest temperatures at the nodes of the superconducting gap their excitations will contribute to the density of states (DOS) at the Fermi level at all temperatures [29]. We wish to study how the contributions to the DOS from the excitations of quasiparticles localized in the vortex cores differs from those of quasiparticles that are delocalized outside the core.

We have performed $^{17}T_1^{-1}$ measurements on both UD81 and UD79 samples at 20 K and 25 K, respectively. The results are shown in Fig. 7.12 along with the same measurement performed at 34 K for comparison. The measurement does not show any appreciable variation in $^{17}T_1^{-1}$ across the frequency spectrum at either temperature. The modest

increase in the T_1^{-1} at the edges of the spectrum are unlikely to be meaningful due to the lower signal-to-noise in these regions which creates larger calculation error.

In order to further investigate the possible variation in $^{17}T_1^{-1}$ across the frequency spectrum in the UD81 sample we used PST to measure T_1^{-1} at a temperature of 5 K at a field of $\approx$ 19 T. The results, shown in Fig. 7.13, also do not show any appreciable variation of $^{17}T_1^{-1}$ across the frequency spectrum. In fact, the $^{17}T_1^{-1}$ at 19 T arguably shows less frequency (field) dependence than that measured at 14 T and 20 K. Note that the $^{17}T_1^{-1}$ measured at 5 K is an order of magnitude smaller than those measured at 20 and 34 K (Fig. 7.12). This shows that the O(2) spins are coupled to the electronic susceptibility of the remaining quasiparticles. Therefore, the lack of variation across the spectrum is further evidence for the system being in the vortex liquid state where the field fluctuations would be averaged out across the spectrum. In this case we would not expect any variation in $^{17}T_1^{-1}$ across the spectra since the correspondence between frequency and field no longer has a well-defined spatial correspondence.

We have also measured $^{17}T_1^{-1}$ in the same sample across the spectrum of the O(1) ($\pm 5/2 \leftrightarrow \pm 3/2$) high-frequency satellite at 5 K at a field of about 30 T. The results (Fig. 7.14) also do not show any appreciable difference in the T_1^{-1} across the spectrum. This absence of observed frequency (field) dependence of $^{17}T_1^{-1}$ could be an additional indication that the VL is absent in this system under the given conditions. Even if we consider the possibility that there is another source of local field fluctuations, such as a spin-density wave (SDW), that dominates the local field profile as well as the relaxation

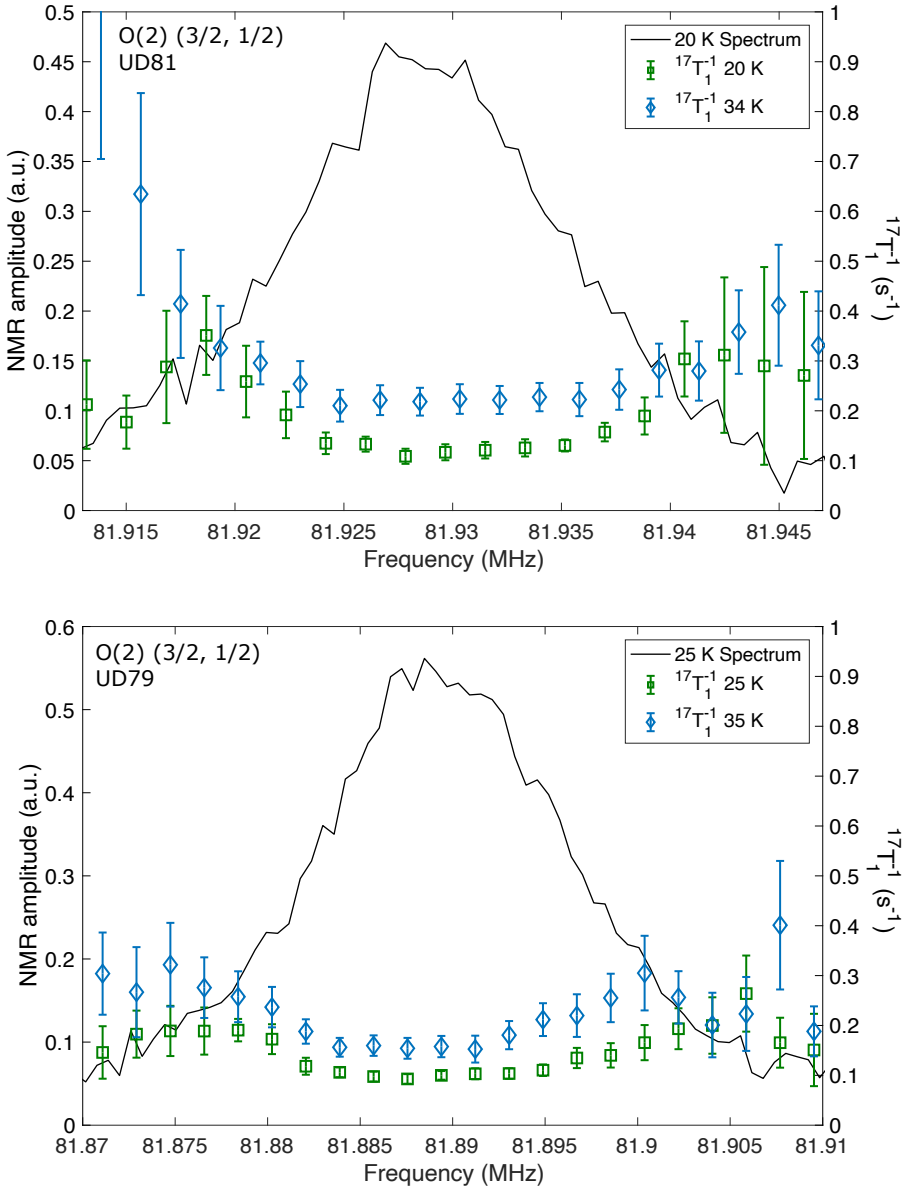

Figure 7.12. A spatially-resolved $^{17}T_1^{-1}$ measurement of the UD81 (top) and UD79 (bottom) samples with $H_o \parallel c$ at 20 K and 25 K (green squares) and 34 K (blue squares). The size of the frequency bins used was 1.8 kHz.

mechanism at high fields it does not explain the absence of the spatial dependence of $^{17}T_1^{-1}$. Recall that Mounce [11] was able to spatially resolve the $^{17}T_1^{-1}$ in his over-doped

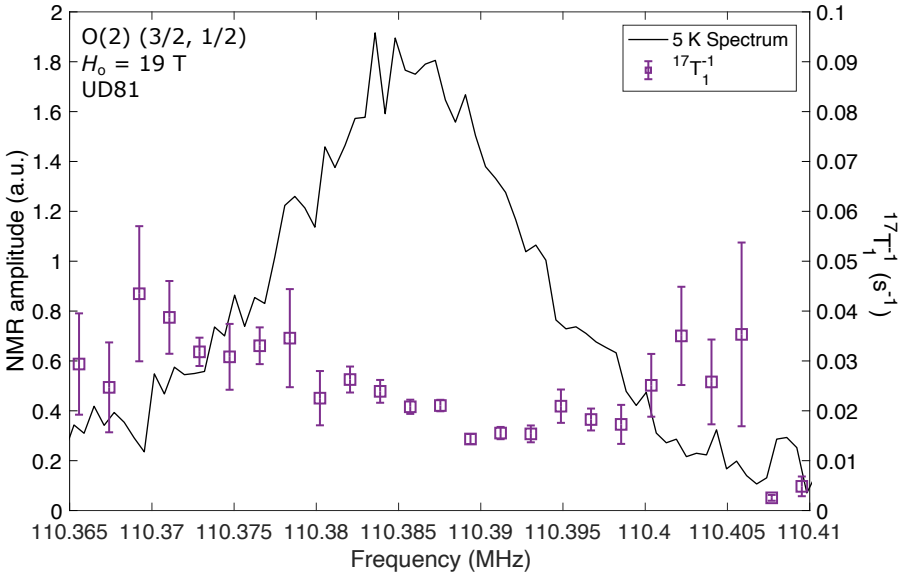

Figure 7.13. The spatially resolved PST measurement of $^{17}T_1^{-1}$ at a field of $\approx$ 19 T at a temperature of 5 K.

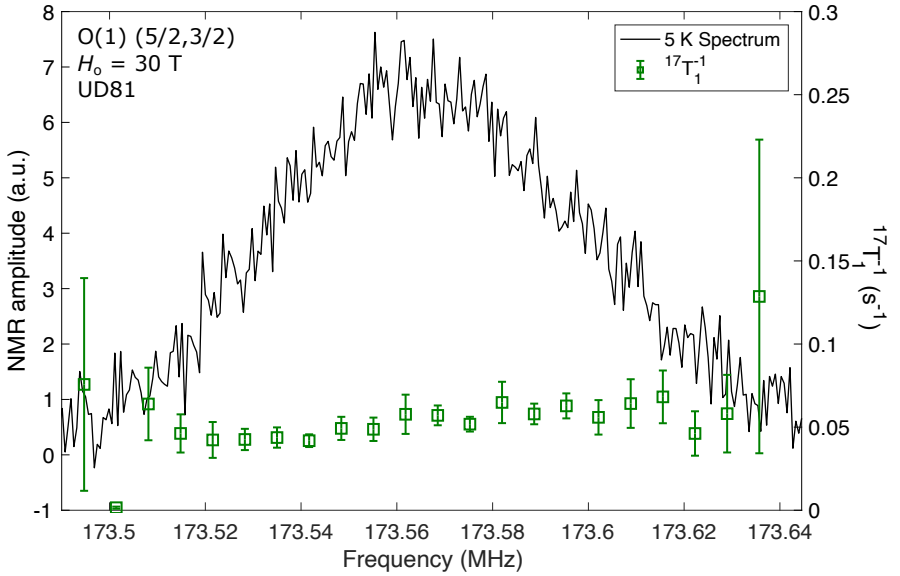

Figure 7.14. The spatially-resolved $^{17}T_1^{-1}$ measurement for the O(1) site at 30 T.

BSCCO samples even with the presence of the SDW field. It is likely that the vortices in our UD81 sample are not quasi-static on the timescale of our NMR measurements at high fields in the temperature range we have probed.

The $^{17}T_1^{-1}$ measurements reported in this section have all been performed on the same under-doped sample of Hg1201 at high fields of ≥ 13.9 T and temperatures down to 5 K. It would be valuable to repeat these measurements at fields below 14 T in this sample. It will also be necessary to repeat these measurements on other single crystal Hg1201 samples of various doping concentrations in the under-doped region of the phase diagram in order to draw conclusions about the under-doped Hg1201 system in general.

7.3. Conclusions

From these data we conclude that we have not observed enough evidence to claim that we see a formation of a VL in our UD81 sample using NMR. From the data we do have it is clear that if a VL is formed at some melting temperature, that temperature is likely much lower than the previously reported value of 40 K [58]. It is also clear that if such a vortex solid state exists in the UD81 sample the vortices in the CuO_2 layers must be de-coupled along the c-axis to explain the absence of a change in the spectral linewidth. These results would put our data in agreement with those of Li [103] and Eley [14].

We propose that further NMR measurements at both O(1) and O(2) sites are needed at low fields ($H_o < 14$ T) and temperatures ($T < 80$ K) to determine whether or not a

VL is formed in our under-doped Hg1201 single crystal sample and whether this system can be studied with NMR.

CHAPTER 8

Conclusions

We have presented our NMR data on two single-crystal samples of the cuprate superconductor Hg1201. Our zero-field cooled magnetization measurements and ^{199}Hg NMR spectra show that both samples are under-doped with the dopant oxygen distributed relatively homogeneously in the ^{199}Hg plane. The lack of spectral broadening in our high-field NMR data on UD81 also indicates that this sample is free of structural defects that would act as pinning centers or cause an amplified field inhomogeneity at higher fields.

Our ^{17}O spin-spin relaxation rate measurements at 14 T indicate that pinned vortices are not present at a temperature of 20 K in either of our under-doped samples. The 19 T $^{17}T_2^{-1}$ data shows evidence for an onset of vortex pinning/freezing in UD81 at a temperature of around 10 K, but further measurements are required at this field at temperatures above 60 K to confirm the validity of this interpretation. We also note that the ^{63}Cu spin-spin relaxation data does not show a change from Gaussian to Lorentzian magnetization decay at any temperature between 20 K and room temperature for either UD81 or UD79 sample.

Other than the increase in the Lorentzian contribution to $^{17}T_2^{-1}$ at temperatures below 10 K in UD81 we do not see any evidence for the formation of a vortex lattice in Hg1201

in our ^{17}O NMR spectra for this sample. We do not observe the formation of the characteristic lineshape of a vortex lattice field in the O(2) ($\pm 3/2 \leftrightarrow \pm 1/2$) spectrum at any field from 14 T to 30 T or temperature from 5 K to room temperature. We also do not observe any field or temperature induced broadening/ narrowing in these O(2) spectra for this sample. The lack of broadening/ narrowing could either indicate that the system remains in the vortex liquid state down to 5 K or that the vortex lattice that forms below 10 K consists of 2D vortex pancakes, which are correlated in the CuO_2 planes but not along the c-axis.

We have attempted spatially resolved $^{17}T_1^{-1}$ measurements at the O(2) satellite of UD81 to detect the contribution of nodal quasiparticle excitations to the density of states at the Fermi level inside and outside the vortex cores. Unlike previous measurements on YBCO [10] and BSCCO [11, 12] we find no evidence for any physically meaningful spatial variation in $^{17}T_1^{-1}$ across the spectrum. It is possible that this is due to a weak hyperfine coupling to the quasiparticles at the O(2) site and that the O(1) site would be optimal for this type of investigation. However, our only spatially-resolved $^{17}T_1^{-1}$ measurement at the O(1) satellite are at the high field of $H_o \approx 30$ T and more measurements at low temperatures (≤ 5 K) are needed to confirm or deny that any new vortex physics would result from such measurements. Our 30 T data do not appear to show any spatial variation in $^{17}T_1^{-1}$ across the spectrum.

In Chapter 7 we noted that data recorded by Lee (Fig. 7.4) shows a modest temperature induced broadening of the O(2) ($\pm 3/2 \leftrightarrow \pm 1/2$) at a field of 16.5 T in our

other under-doped sample, UD79. One possible explanation for this difference in results between the samples is that the UD79 sample contains defects not present in the UD81 sample and that these defects act as pinning centers at temperatures below 15 K. However, this interpretation is incongruent with the fact that the UD79 sample has a narrower ΔT_c transition as measured by magnetometry (Fig. 4.5). This discrepancy between the results for two different single-crystal Hg1201 samples of similar doping concentrations highlights the fact that more measurements are needed on other Hg1201 samples at low temperatures and various fields in order to draw strong conclusions about the Hg1201 system.

Overall, our results indicate that a vortex lattice does not form in the under-doped Hg1201 single crystal samples at the previously reported temperature of 40 K, but rather at a much lower temperature below 20 K if at all. The observed lack of characteristic lineshape or increase in linewidth at low temperatures and high fields suggest that NMR is not an appropriate method of studying vortex lattice geometry. Our results also suggest that the O(2) site may not be appropriate for studying the density of states contribution by quasiparticle scattering between nodes of the energy gap due to the absence of hyperfine coupling at this nuclear site. If this is the case then further $^{17}T_1^{-1}$ measurements are needed at the O(1) site to draw any conclusions about nodal quasiparticle excitations from the NMR data.

APPENDIX A

Recovery profiles

In Chapter 2 we saw that the recovery profile for the j^{th} transition was proportional to the population difference, $n_j(t)$, which was described by the differential equation,

$$\frac{d\boldsymbol{n}(t)}{dt} = \hat{\mathcal{D}}\boldsymbol{n}(t),$$

where the $\hat{\mathcal{D}}$ matrix contained the relaxation rates. We repeat the information obtained from reference [2] here for convenience.

For $I = 1/2$,

(A.1a) $$\hat{\mathcal{D}}_{1/2} = 1/T_1$$

For $I = 3/2$,

(A.1b) $$\hat{\mathcal{D}}_{3/2} = \frac{1}{T_1}\begin{pmatrix} -3 & 2 & 0 \\ 3/2 & -4 & 3/2 \\ 0 & 2 & -3 \end{pmatrix}$$

For $I = 5/2$,

$$\hat{\mathcal{D}}_{5/2} = \frac{1}{T_1}\begin{pmatrix} -5 & 4 & 0 & 0 & 0 \\ 5/2 & -8 & 9/2 & 0 & 0 \\ 0 & 4 & -9 & 4 & 0 \\ 0 & 0 & 9/2 & -8 & 5/2 \\ 0 & 0 & 0 & 4 & -5 \end{pmatrix} \tag{A.1c}$$

The full-recovery and PST profiles are as follows.

A.1. Full-recovery

Below are the n_j/n_o values used in our fitting procedures. We have omitted the higher order transitions for compactness although these are also included in [2].

$I = 1/2$

For a spin-1/2 nucleus there is only one transition for which the population difference is,

$$\frac{n}{n_o} = -e^{-t/T_1}. \tag{A.2}$$

$I = 3/2$

For an excitation of the central $(-1/2 \leftrightarrow 1/2)$ transition the population difference is,

$$\frac{n}{n_o} = -\frac{1}{10}e^{-t/T_1} - \frac{9}{10}e^{-6t/T_1}. \tag{A.3}$$

This is the fit we have used in our ^{63}Cu NMR measurements, all of which have been performed at the central transition.

$I = 5/2$

For an excitation of the central transition the population difference is,

$$\frac{n}{n_o} = -\frac{2}{35}e^{-t/T_1} - \frac{4}{15}e^{-6t/T_1} - \frac{100}{63}e^{-15t/T_1}. \tag{A.4}$$

For an excitation of the first satellite, $(\pm 3/2 \leftrightarrow \pm 1/2)$, we have,

$$\frac{n}{n_o} = -\frac{2}{35}e^{-t/T_1} - \frac{3}{28}e^{-3t/T_1} - \frac{1}{20}e^{-6t/T_1} - \frac{25}{28}e^{-10t/T_1} - \frac{100}{63}e^{-15t/T_1}. \tag{A.5}$$

The majority of our T_1 data in Hg1201 for $I = 5/2$ nuclei are at the ^{17}O $(\pm 3/2 \leftrightarrow \pm 1/2)$ satellite. This is because the central transitions of the two inequivalent stoichiometric oxygen sites overlap at low temperatures due to their difference in temperature dependence of their Knight shifts.

A.2. Progressive saturation recovery fits

In this project we have performed progressive saturation T_1 measurements at the $(\pm 3/2 \leftrightarrow \pm 1/2)$ and the $(\pm 5/2 \leftrightarrow \pm 3/2)$ transitions of the ^{17}O nucleus only. Therefore, we omit the PST profiles for $I = 1/2, 3/2$ and for other transitions and show only the population difference corresponding to this satellite. This population difference is,

$$\frac{n}{n_o} = -Ae^{-t/T_1}\frac{F(t)}{L(t)}, \tag{A.6}$$

where A is a fit parameter related to the tip angle of the magnetization.

$(\pm 3/2 \leftrightarrow \pm 1/2)$.

$$F(t) = 280e^{-21t/T_1} - 272e^{-20t/T_1} + 280e^{-19t/T_1} + 23e^{-18t/T_1} - 7e^{-17t/T_1} + 303e^{-16t/T_1}$$
$$- 242e^{-15t/T_1} + 266e^{-14t/T_1} + 53e^{-13t/T_1} + 16e^{-12t/T_1} + 141e^{-11t/T_1} - 72e^{-10t/T_1}$$
$$+ 141e^{-9t/T_1} + 16e^{-8t/T_1} + 53e^{-7t/T_1} - 14e^{-6t/T_1} + 38e^{-5t/T_1} + 23e^{-4t/T_1} - 7e^{-3t/T_1}$$
$$+ 23e^{-2t/T_1} + 8,$$

$$L(t) = 140(1 - e^{-t/T_1} + e^{-2t/T_1} + e^{-5t/T_1} - e^{-6t/T_1} + e^{-7t/T_1} - e^{-15t/T_1} + e^{-16t/T_1}$$
$$- e^{-17t/T_1} - e^{-20t/T_1} + e^{-21t/T_1} - e^{-22t/T_1}) + A(280e^{-22t/T_1} - 272e^{-21t/T_1} + 280e^{-20t/T_1}$$
$$+ 23e^{-19t/T_1} - 7e^{-18t/T_1} + 303e^{-17t/T_1} - 242e^{-16t/T_1} + 266e^{-15t/T_1} + 53e^{-14t/T_1}$$
$$+ 16e^{-13t/T_1} + 141e^{-12t/T_1} - 72e^{-11t/T_1} + 141e^{-10t/T_1} + 16e^{-9t/T_1} + 53e^{-8t/T_1}$$
$$- 14e^{-7t/T_1} + 38e^{-6t/T_1} + 23e^{-5t/T_1} - 7e^{-4t/T_1} + 23e^{-3t/T_1} + 8e^{-t/T_1}).$$

$(\pm 5/2 \leftrightarrow \pm 3/2)$.

$$F(t) = 70e^{-21t/T_1} - 68e^{-20t/T_1} + 70e^{-19t/T_1} + 17e^{-18t/T_1} - 13e^{-17t/T_1} + 87e^{-16t/T_1}$$
$$-23e^{-15t/T_1}+29e^{-14t/T_1}+62e^{-13t/T_1}+4e^{-12t/T_1}+24e^{-11t/T_1}+42e^{-10t/T_1}+24e^{-9t/T_1}+4e^{-8t/T_1}$$
$$+ 62e^{-7t/T_1} - 41e^{-6t/T_1} + 47e^{-5t/T_1} + 17e^{-4t/T_1} - 13e^{-3t/T_1} + 17e^{-2t/T_1} + 2),$$

$$L(t) = 35(1 - e^{t/T_1} + e^{-2t/T_1} + e^{-5t/T_1} - e^{-6t/T_1} + e^{-7t/T_1} - e^{-15t/T_1}$$

$$+ e^{-16t/T_1} - e^{-17t/T_1} - e^{-20t/T_1} + e^{21t/T_1} - e^{-22t/T_1}) + A(70e^{-22t/T_1} - 68e^{-21t/T_1}$$

$$+ 70e^{-20t/T_1} + 17e^{-19t/T_1} - 13e^{-18t/T_1} + 87e^{-17t/T_1} - 23e^{-16t/T_1} + 29e^{-15t/T_1} + 62e^{-14t/T_1}$$

$$+ 4e^{-13t/T_1} + 24e^{-12t/T_1} + 42e^{-11t/T_1} + 24e^{-10t/T_1} + 4e^{-9t/T_1} + 62e^{-8t/T_1} - 41e^{-7t/T_1}$$

$$+ 47e^{-6t/T_1} + 17e^{-5t/T_1} - 13e^{-3t/T_1} + 17e^{-3t/T_1} + 2e^{-t/T_1}).$$

APPENDIX B

The density matrix formulation and Redfield theory

We can describe both T_1 and T_2 processes using the density matrix formulation, where a system of nuclear spins interacting with the "lattice" can be described using the density matrix and statistical mechanics[1]. This description utilizes Boltzmann statistics to describe the spin system at thermal equilibrium as well as time-dependent perturbation theory to describe time-dependent fluctuating fields that contribute to transitions between energy levels.

We begin by assuming the spin states can be described by the wavefunctions, Ψ, where,

$$\Psi = \sum_n c_n u_n, \tag{B.1}$$

where the u_n's are a complete set of orthonormal functions which are time-independent eigenstates of the Zeeman Hamiltonian. Thus, the c_n's carry all the time dependence. Writing the u_n in bra-ket notation we can express the expectation value of an operator, such as the x-component of the magnetization, $\hat{M}_x$, as,

$$\langle \hat{M}_x \rangle = \sum_{n,m} c_m^* c_n \langle m|\hat{M}_x|n\rangle. \tag{B.2}$$

[1]The following explanation was adapted from Ref. [34] as well as notes from J. A. Sauls' Graduate Quantum Mechanics III Lectures in 2016.

The matrix formed by the coefficient products $c_n c_m^*$ can be written as the matrix elements of a Hermitian operator, $\hat{O}$,

$$\langle n|\hat{O}|m\rangle = c_n c_m^*. \tag{B.3}$$

We have defined Ψ as the wavefunction of a single spin, but in an NMR system we will have an ensemble of spins, each described by their own Ψ. It is then useful to talk about expectation value in terms of an ensemble average, denoted by bar, $\overline{\langle\ \rangle}$. The expectation value of $\hat{M}_x$ in an ensemble is then expressed as the ensemble average,

$$\overline{\langle \hat{M}_x \rangle} = \sum_{n,m} \overline{c_n c_m^*} \langle m|\hat{M}_x|n\rangle, \tag{B.4}$$

where the matrix element, $\langle m|\hat{M}_x|n\rangle$, remains the same for all systems. We define the ensemble average, $\overline{c_n c_m^*}$, as the density matrix, $\hat{\rho}$. Thereby, the elements of the density matrix are,

$$\langle n|\hat{\rho}|m\rangle = \overline{c_n c_m^*} = \overline{\langle n|\hat{O}|m\rangle}. \tag{B.5}$$

Then, by definition, the ensemble-averaged expectation value of the $\hat{M}_x$ operator is defined as,

$$\begin{aligned} \overline{\langle \hat{M}_x \rangle} &= \sum_{n,m} \langle n|\hat{\rho}|m\rangle \langle m|\hat{M}_x|n\rangle, \\ &= \mathrm{Tr}\{\hat{\rho}\hat{M}_x\} = \mathrm{Tr}\{\hat{M}_x\hat{\rho}\}, \end{aligned} \tag{B.6}$$

where Tr{} denotes the trace.

We can solve for the time dependence of $\hat{\rho}$ by setting up the time-dependent Schrödinger equation for one spin system, Ψ, and take the ensemble average of the solution. This gives us the differential equation,

$$\frac{d}{dt}\hat{\rho} = \frac{i}{\hbar}\big[\hat{\rho}, \hat{\mathcal{H}}\big], \tag{B.7}$$

where $\hat{\mathcal{H}}$ is the Hamiltonian for all systems in the ensemble. The solution for $\hat{\rho}$ in the case of a time-independent Hamiltonian is,

$$\hat{\rho}(t) = e^{-(i/\hbar)\hat{\mathcal{H}}t}\hat{\rho}(0)e^{(i/\hbar)\hat{\mathcal{H}}t}. \tag{B.8}$$

Now we apply the density matrix formulation to an NMR systems, i.e. a system of nuclear spins in thermal equilibrium with a reservoir (spin lattice) at temperature T. The basis states are the eigenstates of the Zeeman Hamiltonian, $\hat{\mathcal{H}}_Z = -\gamma\hbar H_o\hat{I}_z$, where γ is the nuclear gyromagnetic ratio, H_o is the static applied field and $\hat{I}_z$ is the operator corresponding to the z-component of the nuclear spin. In this case the diagonal elements of $\hat{\rho}$ are the populations of the eigenstates given by the Boltzmann distribution,

$$\overline{c_m c_m^*} = \mathcal{Z}^{-1}e^{-\beta E_m}, \tag{B.9}$$

where $\beta = k_B T$, k_B is the Boltzmann factor and $\mathcal{Z}$ is the partition function, defined as,

$$\mathcal{Z} = \sum_n e^{-\beta E_n}, \tag{B.10}$$

and E_n is the energy of the Zeeman eigenstate n.

In the case of spin-lattice relaxation we have the additional contribution to the NMR Hamiltonian from the spin-lattice interaction. We can consider this contribution to the Hamiltonian, $\hat{\mathcal{H}}_1(t)$, to be a time-dependent perturbation to $\hat{\mathcal{H}}_Z$. We can then treat the problem of finding relaxation rates using time-dependent perturbation theory. We do all calculations in the interaction picture where the operators are transformed as,

$$\hat{\rho}^*(t) = e^{(i/\hbar)\hat{\mathcal{H}}_Z t}\hat{\rho}(t)e^{-(i/\hbar)\hat{\mathcal{H}}_Z t}, \tag{B.11}$$

$$\hat{\mathcal{H}}_1^*(t) = e^{(i/\hbar)\hat{\mathcal{H}}_Z t}\hat{\mathcal{H}}_1(t)e^{-(i/\hbar)\hat{\mathcal{H}}_Z t}, \tag{B.12}$$

where the asterisk indicates that the operator has been transformed to the interaction basis and not that the operator is a complex conjugate. In the interaction picture we extract the time dependence that would result if $\hat{\mathcal{H}}_1(t) = 0$, i.e. (B.8). This causes the wavefunctions in (B.1) to be replaced by,

$$\Psi = \sum_n a_n e^{-(i/\hbar)E_n t}u_n, \tag{B.13}$$

where the coefficients have redefined as $c_n = a_n e^{-(i/\hbar)E_n t}$ where the E_n are the eigenvalues of $\hat{\mathcal{H}}_Z$ and $\overline{a_n a_m^*} = \langle n|\hat{\rho}^*|m\rangle$.

Recall that the solutions for a time-dependent perturbation $\hat{\mathcal{H}}_1(t)$ is to first order,

$$\hat{\rho}^*(t) = \hat{\rho}^*(0) + \frac{i}{\hbar}\int_0^t dt' \big[\hat{\rho}^*(0), \hat{\mathcal{H}}_1^*(t')\big], \tag{B.14}$$

which is obtained by substituting $\hat{\rho}^*(t') = \hat{\rho}^*(0)$ into the expression,

$$\hat{\rho}^*(t) = \hat{\rho}^*(0) + \frac{i}{\hbar}\int_0^t dt' \big[\hat{\rho}^*(t'), \hat{\mathcal{H}}_1^*(t')\big]. \tag{B.15}$$

Also recall that we obtain the n^{th} order corrections to (B.15) by plugging the $n-1$ order solution for $\hat{\rho}^*(t)$ so that to second order we have,

$$\hat{\rho}^*(t) = \hat{\rho}^*(0) + \frac{i}{\hbar}\int_0^t dt' \left[\left(\hat{\rho}^*(0) + \frac{i}{\hbar}\int_0^{t'} dt''[\hat{\rho}^*(0), \hat{\mathcal{H}}_1^*(t'')]\right), \hat{\mathcal{H}}_1^*(t')\right]. \tag{B.16}$$

Then, to second order, the evolution of $\hat{\rho}^*(t)$ is described by,

$$\frac{d\hat{\rho}^*(t)}{dt} = \frac{i}{\hbar}\big[\hat{\rho}^*(0), \hat{\mathcal{H}}_1^*(t)\big] - \left(\frac{1}{\hbar}\right)^2 \int_0^t dt' \big[[\hat{\rho}^*(0), \hat{\mathcal{H}}_1^*(t')], \hat{\mathcal{H}}_1^*(t)\big]. \tag{B.17}$$

Here we can define the frequency $\omega_n \equiv E_n/\hbar$, and note that, $\langle m|\hat{\mathcal{H}}_1^*(t)|n\rangle = e^{i(\omega_m-\omega_n)t}\langle m|\hat{\mathcal{H}}_1(t)|n\rangle$. This latter relation is useful because we must find the expectation value of (B.17) in order to find the relaxation rates.

Reference [34] gives a useful example of the use of the density matrix in an ensemble of nuclear spins where the perturbation $\hat{\mathcal{H}}_1(t)$ varies randomly in time and is different from ensemble to ensemble. If we want to find the rate of the probability of a transition from a state with energy E_k to one with energy E_m we take the expectation value and

ensemble average of (B.17) in the state $|m\rangle$ and define the correlation function $G_{mk}(\tau)$,

$$G_{mk}(\tau) = \overline{\langle m|\hat{\mathcal{H}}_1(t-\tau)|k\rangle\langle k|\hat{\mathcal{H}}_1(t)|m\rangle}, \tag{B.18}$$

where $\tau \equiv t - t'$; this function is a measure of how the perturbation is correlated in time. The correlation function has the property that,

$$G_{mk}(\tau) = G_{km}(-\tau), \tag{B.19}$$

in the region where the change in the perturbation $\hat{\mathcal{H}}_1(t)$ is negligible. The timescale over which this holds is the correlation time, τ_c, which describes the timescale of the motion of each ensemble. Note that $G_{mk}(\tau)$ is a function of τ only and is independent of time, t.

B.1. Redfield theory

The Redfield theory is a general formulation of the density matrix to describe a nuclear spin system. The formulation is named after physicist A. G. Redfield who published his work [117] based on previous work by Wangsness and Bloch [118] and Bloch [119]. Redfield also drew inspiration from the mean-field treatment used by Bloembergen, Purcell and Pound [120] to describe the effect of the nuclear spin coupling to a thermal bath. Redfield expanded on these previous theories by considering a system of nuclear spins relaxed by a randomly fluctuating perturbation and considering both diagonal and off-diagonal elements of the density matrix. Previous theories had considered only the diagonal elements of the density matrix, which are those that give spin-lattice relaxation

rates, to be significant.

Redfield [117] considers the density matrix as consisting of two independent components, the spin system density matrix, $\hat{\sigma}$, and that which describes the thermal reservoir (the lattice), $\hat{\rho}^L$. He considers the spin system to be an ensemble of ensembles and the time-dependent perturbation, $\hat{\mathcal{H}}_1(t)$, to vary randomly between spin ensembles and to be statistically static for each ensemble. The length scale of this variation is the same correlation time, τ_c, which we saw in the previous section. This perturbation is also the interaction that couples the spins to the lattice. We also assume that the density matrix of all ensembles coincides at $t = 0$.

We will adopt the indexing convention of [117] and index the spin (Zeeman) eigenstates by α, β, γ, rather than by n, m, and k. We also define,

$$\hat{\sigma}_{\alpha\alpha'} \equiv \langle\alpha|\hat{\sigma}|\alpha'\rangle,$$

for compactness. The Redfield equation of motion is,

$$\frac{d}{dt}\hat{\sigma}^*_{\alpha\alpha'} = \sum_{\beta,\beta'} R_{\alpha\alpha',\beta\beta'} e^{i(\omega_\alpha - \omega_{\alpha'} - \omega_\beta + \omega_{\beta'})} \hat{\sigma}^*_{\beta\beta'}, \tag{B.20}$$

where $\omega_\alpha \equiv \frac{E_\alpha}{\hbar}$. This is an equation only for the spin component of the density matrix, $\hat{\rho} = \hat{\sigma}\hat{\rho}^L$ because the latice is assumed to remain in thermal equilibrium even in the presence of the spin relaxation processes. The coefficient $R_{\alpha\alpha',\beta\beta'}$ is time-independent [34]

and defined in Redfield's paper as,

$$R_{\alpha\alpha',\beta\beta'} = \frac{1}{\hbar^2}\big[J_{\alpha\beta\alpha'\beta'}(\omega_{\alpha'} - \omega_{\beta'}) + J_{\alpha\beta\alpha'\beta'}(\omega_{\alpha'} - \omega_{\beta'})$$

$$- \delta_{\alpha'\beta'}\sum_{\gamma} J_{\gamma\beta\gamma\alpha}(\omega_{\gamma} - \omega_{\beta}) - \delta_{\alpha\beta}\sum_{\gamma} J_{\gamma\beta'\gamma\alpha'}(\omega_{\gamma} - \omega_{\beta'})\big], \tag{B.21}$$

where,

$$J_{\alpha\beta\alpha'\beta'}(\omega) = \frac{1}{2}\int_{-\infty}^{\infty} d\tau e^{-i\omega\tau} G_{\alpha\beta\alpha'\beta'}(\tau), \tag{B.22}$$

is a spectral density of the interaction described by correlation function, $G_{\alpha\beta\alpha'\beta'}(\tau)$.

The complex exponential in (B.20) ensures that the only terms contributing to the sum will be those for which $\omega_\alpha - \omega_{\alpha'} = \omega_\beta - \omega_{\beta'}$. If we include only these terms in the sum we can simplify (B.20) to,

$$\frac{d}{dt}\hat{\sigma}^*_{\alpha\alpha'} = {\sum_{\beta,\beta'}}' R_{\alpha\alpha',\beta\beta'}\hat{\sigma}^*_{\beta\beta'}, \tag{B.23}$$

where the prime on the sum indicates that the sum is only over the states which satisfy $\omega_\alpha - \omega_{\alpha'} = \omega_\beta - \omega_{\beta'}$.

The above equations of motion for the spin density matrix are valid over a time interval, Δt, under the conditions,

$$\Delta t \gg \tau_c, \tag{B.24a}$$

$$\frac{1}{R_{\alpha\alpha',\beta\beta'}} \gg \Delta t. \tag{B.24b}$$

Condition (B.24a) says that our time interval is greater than that over which the correlation function, $G_{\alpha\beta,\alpha'\beta'}(\tau)$, is non-zero. We take the correlation of the interaction to be non-zero only in the range $|\tau| < \tau_c$ and to drop rapidly to zero for all $|\tau| > \tau_c$ such that for our time interval, Δt, we can extend our integration limits to $\pm\infty$. The second condition, (B.24b), ensures that our density matrix does not vary rapidly over time interval Δt.

In the general example of Redfield theory we consider a $\hat{\mathcal{H}}_1(t)$ which consists of randomly fluctuating fields in the x, y and z directions,

$$\hat{\mathcal{H}}_1(t) = \sum_q H_q(t)\hat{K}^q. \tag{B.25}$$

Here, $H_q(t)$ is the $q = x, y, z$ component of the fluctuating magnetic field and is independent of spin and $\hat{K}^q = -\gamma\hbar\hat{I}_q$ where the $\hat{I}_q$ are the q components of the nuclear spin operators. We take the $H_q(t)$ to be uncorrelated so that the time average of the fluctuating fields is zero. This condition mandates that the relaxation of this spin system will be due only to the spin and lattice coupling and not to an external driving field such as the $\boldsymbol{H}_1$ discussed in Chapter 2.

We re-write our correlation function, (B.18), using (B.25) as,

$$\begin{aligned} G_{\alpha\beta,\alpha'\beta'}(\tau) &= \overline{\langle\alpha|\hat{\mathcal{H}}_1(t)|\beta\rangle\langle\beta'|\hat{\mathcal{H}}_1(t+\tau)|\alpha'\rangle}, \\ &= \sum_{q,q'}\langle\alpha|K^q|\beta\rangle\langle\beta'|K^{q'}|\alpha'\rangle\overline{H_q(t)H_{q'}(t+\tau)}. \end{aligned} \tag{B.26}$$

The spectral density of this interaction is,

$$L_{qq'}(\omega) = \int_0^\infty d\tau \overline{H_q(t)H_{q'}(t+\tau)} e^{-i\omega t}, \tag{B.27}$$

where the $H_q(t)$ are real functions of time and their correlation function is an even function of τ. If we divide (B.27) into real and imaginary parts and note that the real component gives us the relaxation behavior we define a function $k_{qq'}(\omega)$ as,

$$Re\{L_{qq'}(\omega)\} = \frac{1}{2}\int_{-\infty}^\infty d\tau \overline{H_q(t)H_{q'}(t+\tau)} \cos\omega\tau \equiv k_{qq'}(\omega). \tag{B.28}$$

With this in mind we can re-write (B.22) as,

$$J_{\alpha\beta\alpha'\beta'}(\omega) = \sum_{q,q'} K^q_{\alpha\beta} K^{q'}_{\alpha'\beta'} k_{qq'}(\omega). \tag{B.29}$$

One might notice that in our current system we would have an equal rate of probability of transition in both directions, i.e. $R_{\alpha\alpha',\beta\beta'} = R_{\beta\beta',\alpha\alpha'}$. If we work in the high temperature limit, which is often the case in NMR, we can remedy this by replacing the density matrix by the difference, $\hat{\sigma} \to \hat{\sigma} - \hat{\sigma}(T)$, where,

$$\hat{\sigma}_{\beta\beta'}(T) = \delta_{\beta\beta'} e^{-\hbar\omega_\beta/k_BT} \left(\sum_{\beta''} e^{-\hbar\omega_{\beta''}/k_BT} \right)^{-1}, \tag{B.30}$$

is the thermal equilibrium value of $\hat{\sigma}$.

Recall that we assumed that the fluctuations in the field in each direction were independent. This means that the correlation function, $\overline{H_q(t)H_{q'}(t+\tau)} = 0$ unless $q = q'$.

Therefore, the only terms contributing to our spectral density will be $k_{qq}(\omega)$.

We can now find the effects of relaxation on the x, y, z components of the spins by using (B.23) to find the differential equation for the expectation values of the $\hat{I}_r$ operators. First we re-write (B.23) by noting,

$$\hat{\sigma}^*_{\alpha\alpha'} = e^{i(\omega_\alpha - \omega_{\alpha'})t}\hat{\sigma}_{\alpha\alpha'}, \tag{B.31}$$

and taking the time derivative,

$$\frac{d}{dt}\hat{\sigma}^*_{\alpha\alpha'} = i(\omega_\alpha - \omega_{\alpha'})\hat{\sigma}^*_{\alpha\alpha'} + e^{i(\omega_\alpha - \omega_{\alpha'})t}\frac{d}{dt}\hat{\sigma}_{\alpha\alpha'}. \tag{B.32}$$

Rearranging (B.32) to get $d\hat{\sigma}_{\alpha\alpha'}/dt$ in terms of $\hat{\sigma}^*$ we get the expression,

$$\begin{aligned}\frac{d}{dt}\hat{\sigma}_{\alpha\alpha'} &= i(\omega_{\alpha'} - \omega_\alpha)\hat{\sigma}_{\alpha\alpha'} + \sum_{\beta,\beta'} R_{\alpha\alpha',\beta\beta'}\hat{\sigma}_{\beta\beta'}, \\ &= \frac{i}{\hbar}\left[\hat{\sigma}, \hat{\mathcal{H}}_Z\right]_{\alpha\alpha'} + \sum_{\beta,\beta'} R_{\alpha\alpha',\beta\beta'}\hat{\sigma}_{\beta\beta'}. \end{aligned} \tag{B.33}$$

We can also write the expression for $J_{\alpha\beta\alpha'\beta'}(\omega)$ with the K^q given in terms of the spin operators,

$$J_{\alpha\beta\alpha'\beta'}(\omega) = \gamma^2\hbar^2 \sum_q \langle\alpha|\hat{I}_q|\beta\rangle\langle\beta'|\hat{I}_q|\alpha'\rangle k_{qq}(\omega). \tag{B.34}$$

Our goal is to calculate the effects of relaxation on the x, y, z components of the nuclear spins. To do this, we can set up the equation of motion for the expectation value of the

$\hat{I}_r$ operators, where $r = x, y, z$. This differential equation is,

$$\frac{d}{dt}\langle \hat{I}_r \rangle = \sum_{\alpha,\alpha'} \left[\left(\frac{i}{\hbar} \right) \left[\hat{\sigma}, \hat{\mathcal{H}}_Z \right]_{\alpha\alpha'} \langle \alpha' | \hat{I}_r | \alpha \rangle + \sum_{\beta,\beta'} R_{\alpha\alpha',\beta\beta'} \hat{\sigma}_{\beta\beta'} \langle \alpha' | \hat{I}_r | \alpha \rangle \right]. \tag{B.35}$$

We can evaluate the first and second term in (B.35) separately. The first term can be evaluated by noting the identity, $\sum_n |n\rangle\langle n| = \hat{1}$, where $\hat{1}$ is the identity matrix and that the trace of an operator is the sum of its diagonal elements. Thus, the first term becomes,

$$\left(\frac{i}{\hbar} \right) \sum_{\alpha,\alpha'} \left[\hat{\sigma}, \hat{\mathcal{H}}_Z \right]_{\alpha\alpha'} \langle \alpha' | \hat{I}_r | \alpha \rangle = -i\gamma_n H_o Tr\{ \hat{\sigma} [\hat{I}_q, \hat{I}_r] \}. \tag{B.36}$$

The second term in (B.35) requires a lot more algebra and the use of orthogonality and completeness relations. For each term in (B.21) we can use the sums over the indices not included in the argument of the $k_{qq}(\omega)$ to collapse the wavefunctions. For example, the second term can be evaluated as,

$$\begin{aligned} &\frac{1}{\hbar^2} \sum_{\alpha,\alpha'} \sum_{\beta,\beta'} J_{\alpha\beta,\alpha'\beta'}(\omega_\alpha - \omega_\beta) \hat{\sigma}_{\beta\beta'} \langle \alpha' | \hat{I}_r | \alpha \rangle \\ &\quad = \gamma_n^2 \sum_q \sum_{\alpha,\alpha'} \sum_{\beta,\beta'} \langle \alpha | \hat{I}_q | \beta \rangle \langle \beta' | \hat{I}_q | \alpha' \rangle \langle \beta | \hat{\sigma} | \beta' \rangle \langle \alpha' | \hat{I}_r | \alpha \rangle k_{qq}(\omega_\alpha - \omega_\beta) \\ &\quad = \gamma_n^2 \sum_q \sum_{\alpha,\beta} \langle \alpha | \hat{I}_q | \beta \rangle \langle \beta | \hat{\sigma} \hat{I}_q \hat{I}_r | \alpha \rangle k_{qq}(\omega_\alpha - \omega_\beta), \end{aligned} \tag{B.37}$$

where we have taken the sum over the primed indices because the unprimed α, β contribute to the integral in $k_{qq}(\omega_\alpha - \omega_\beta)$. We can repeat this process for the other three terms and

end up with,

$$\sum_{\alpha,\alpha'}\sum_{\beta,\beta'} R_{\alpha\alpha',\beta\beta'}\hat{\sigma}_{\beta\beta'}\langle\alpha'|\hat{I}_r|\alpha\rangle$$

$$= \gamma_n^2 \sum_q \sum_{\alpha,\beta} \langle\alpha|\hat{I}_q|\beta\rangle\langle\alpha|\left[[\hat{I}_r,\hat{I}_q],\hat{\sigma}\right]|\beta\rangle k_{qq}(\omega_\beta - \omega_\alpha). \tag{B.38}$$

We can find the relaxation rate, $1/T_1$ by using $\hat{\sigma} - \hat{\sigma}(T)$ rather than $\hat{\sigma}$ in (B.35) and solving for $r = z$. The result is,

$$\frac{d}{dt}\langle\hat{I}_z\rangle = \gamma_n\left[\langle\hat{\boldsymbol{I}}\rangle \times \boldsymbol{H}_o\right]_z - \gamma_n^2[k_{xx}(\omega_L) + k + yy(\omega_L)](\langle\hat{I}_z\rangle - I_o), \tag{B.39}$$

where ω_L is the Larmor frequency, which appears because in $\hat{I}_x$ and $\hat{I}_y$ the only non-vanishing terms will be those that differ by $\Delta m = \pm 1$ which correspond to the energy, $\hbar\omega_L = \gamma_n\hbar H_o$. Therefore, the only contributing frequency differeence is $\omega_\beta - \omega_\alpha = \omega_L$. The spin-lattice relaxation rate is the coefficient of the $(\langle\hat{I}_z\rangle - I_o)$ (I_o is the equilibrium nuclear spin) term,

$$\frac{1}{T_1} = \gamma_n^2[k_{xx}(\omega_L) + k_{yy}(\omega_L)]. \tag{B.40}$$

The procedure for finding $1/T_2$ is similar in that we are looking for the expectation value of the transverse spin components, $\hat{I}_x, \hat{I}_y$, which are relaxed by both fluctuations in the opposite transverse field components and the longitudinal field, H_z. The x and y spin expectation values should have an equilibrium value of zero so we do not need to subtract $\hat{\sigma}(T)$ from $\hat{\sigma}$ to get a physically reasonable solution for (B.35). The resulting equation of

motion for the x component is,

$$\frac{d}{dt}\langle \hat{I}_x \rangle = \gamma_n \big[\langle \hat{\boldsymbol{I}} \rangle \times \boldsymbol{H}_o \big]_x - \gamma_n^2 [k_{yy}(\omega_L) + k_{zz}(0)] \langle \hat{I}_x \rangle. \tag{B.41}$$

Here we see that the contribution of the spectral density of the fluctuating z field enters at zero frequency. The spin-spin relaxation rate is then the coefficient,

$$\frac{1}{T_2} = \gamma_n^2 [k_{yy}(\omega_L) + k_{zz}(0)]. \tag{B.42}$$

These results were derived for the specific example of $\hat{\mathcal{H}}_1(t)$ being given by three independent fluctuating fields in the x, y, z directions. Nonetheless, this example illustrates that the experimental relaxation rates give us information about the physics involved in each relaxation mechanism.

Note that the spin-lattice relaxation rate (B.40) depends on the spectral densities of the transverse fluctuating fields at the Larmor frequency. This is an intuitive result that can be thought of in relation to the semi-classical model where the extra terms in the torque on $\boldsymbol{M}$ was due to the frame rotating at ω_L. The physics [34] behind the spin-spin relaxation result is more interesting. Notice that (B.42) has one term in common with (B.40) and one term that depends on the fluctuating z field at zero frequency. The latter term can also be thought of in analogy to the rotating frame in that it is due to the x spin component being relaxed by the stationary field component H_z, which is also stationary in the rotating frame[2].

[2]The z-axis is a common axis between the laboratory and rotating frames.

The first term in (B.42) is shared with the expression for ${T_1}^{-1}$ because this term is a result of the finite lifetime of and energy eigenstate due to the spin-lattice relaxation. This is an important result of Redfield's theory and can be expressed by the following statement,

$$\frac{1}{T_2} = \frac{1}{T_2^*} + \frac{C_R}{T_1}, \tag{B.43}$$

where T_2^* is discussed in Chapter 2 and C_R is the Redfield coefficient.

References

[1] A. P. Reyes, *MAGRes2000 Integrated Wideband NMR Spectrometer and Network Analyzer: Hardware and Programming Technical Reference Manual*. National high Magnetic Field Laboratory, 1800 E. Paul Dirac Drive, Tallahassee, FL 32310, 2007.

[2] V. F. Mitrović, *Nuclear Magnetic Resonance Study of the Onset of Superconductivity and Low-Engergy Excitations in High Temperature Superconductors*. PhD thesis, Northwestern University, December 2001.

[3] A. M. Mounce, *Nuclear Magnetic Resonance Study of High-Temperature Superconductivity*. PhD thesis, Northwestern University, August 2013.

[4] J. Lee, *Nuclear Magnetic Resonance Study of the High Temperature Superconductors and Unconventional Mass Diffusion*. PhD thesis, Northwestern University, September 2016.

[5] N. Barii, S. Badoux, M. Chan, C. Dorow, W. Tabis, B. Vignolle, G. Yu, J. Béard, X. Zhao, C. Proust, and M. Greven, "Universal quantum oscillations in the underdoped cuprate superconductors," *Nature Physics*, vol. 9, pp. 761–764, Dec. 2013.

[6] W. Tabis, B. Yu, I. Biao, M. Bluschke, T. Koodziej, A. Kozlowski, E. Blackburn, K. Sen, E. Forgan, M. Zimmermann, Y. Tang, E. Weschke, B. Vignolle, M. Hepting, H. Gretarsson, R. Sutarto, F. He, M. Le Tacon, N. Barišić, and M. Greven, "Synchrotron x-ray scattering study of charge-density-wave order in $HgBa_2CuO_{4+\delta}$," *Physical Review B*, vol. 96, 10 2017.

[7] I. Stolt, J. A. Lee, A. Mounce, Y. Xin, and W. Halperin, "Location of the oxygen dopant in the high temperature superconductor $HgBa_2CuO_{4+\delta}$ from ^{199}Hg NMR," *Physica C: Superconductivity and its Applications*, vol. 555, pp. 24 – 27, 2018.

[8] R. Stern, I. Heinmaa, D. Pavlov, and I. Bryntse, "Exploring the oxygen order in Hg-1223 and Hg-1201 by (199)Hg MAS NMR," in *New Challenges in Superconductivity: Experimental Advances and Emerging Theories* (J. Ashkenazi, M. Eremin, J. Cohn, E. Ilya, D. Manske, D. Pavuna, and F. Zou, eds.), vol. 183 of *NATO Science Series II-Mathematics Physics and Chemistry*, pp. 69–72, 2005.

[9] H. N. Bachman, A. P. Reyes, V. F. Mitrovic, and W. P. Halperin, "High-Field Vortex Dynamics in $YBa_2Cu_3O_7$ from ^{17}O Nuclear Magnetic Resonance," *Phys. Rev. Lett.*, vol. 80, pp. 1726–1729, February 1998.

[10] V. F. Mitrović, E. E. Sigmund, M. Eschrig, H. N. Bachman, W. P. Halperin, A. P. Reyes, K. P., and W. G. Moulton, "Spatially resolved electronic structure inside and outside the vortex core of a high temperature superconductor," *Nature*, vol. 413, no. 6855, pp. 501–504, 2001.

[11] A. M. Mounce, S. Oh, S. Mukhopadhyay, W. P. Halperin, A. P. Reyes, P. L. Kuhns, K. Fujita, M. Ishikado, and S. Uchida, "Spin-density wave near the vortex cores in the high-temperature superconductor $Bi_2Sr_2CaCu_2O_{8+y}$," *Phys. Rev. Lett.*, vol. 106, p. 057003, Feb 2011.

[12] A. M. Mounce, S. Oh, W. P. Halperin, A. P. Reyes, P. L. Kuhns, K. Fujita, M. Ishikado, and S. Uchida, "Charge-induced vortex lattice instability," *Nature Physics*, vol. 7, pp. 125–128, Nov 2011.

[13] L. I. Glazman and A. E. Koshelev, "Thermal fluctuations and phase transitions in the vortex state of a layered superconductor," *Phys. Rev. B*, vol. 43, pp. 2835–2843, Feb 1991.

[14] S. Eley, R. Willa, M. K. Chan, E. D. Bauer, and L. Civale, "Vortex phases and glassy dynamics in the highly anisotropic superconductor $HgBa_2CuO_{4+\delta}$," *Scientific Reports*, vol. 10, no. 10239, 2020.

[15] B. Chen, W. P. Halperin, P. Guptasarma, D. G. Hinks, V. F. Mitrović, A. P. Reyes, and P. L. Kuhns, "Two-dimensional vortices in superconductors," *Nature Physics*, vol. 3, pp. 239–242, 2007.

[16] H. K. Onnes, "Further experiments with liquid helium. c. on the change of electric resistance of pure metals at very low temperatures etc. iv. the resistance of pure mercury at helium temperatures," in *KNAW, Proceedings*, vol. 13, (Amsterdam), pp. 1274–1276, Huygens Institute - Royal Netherlands Academy of Arts and Sciences (KNAW), 1910–1911.

[17] W. Meissner and R. Ochsenfeld, "Ein neuer Effekt bei Eintritt der Supraleitfähigkeit," *Naturwissenschaften*, vol. 21, pp. 787–788, Nov 1933.

[18] F. London and H. London, "The electromagnetic equations of the supraconductor," *Proceedings of the Royal Society A: Mathematical, Physical and Engineering Sciences*, vol. 149, no. 866, 1935.

[19] V. L. Ginzburg and L. D. Landau, "On the theory of superconductivity," *Zhurnal Eksperimental'noi i Teoreticheskoi Fiziki*, vol. 20, p. 1064, 1950.

[20] A. A. Abrikosov, "On the Magnetic Properties of Superconductors of the Second Group," *Soviet Physics JETP*, vol. 5, pp. 1442–1452, December 1957.

[21] A. A. Abrikosov, "The magnetic properties of superconducting alloys," *Journal of Physics and Chemistry of Solids*, vol. 2, no. 3, pp. 199–208, 1957.

[22] R. E. Walstedt, *The NMR Probe of High-T_c Materials*, vol. 228 of *Springer Tracts in Modern Physics*. Springer, 2008.

[23] J. G. Bednorz and K. A. Mueller, "Possible high T_c superconductivity in the Ba–La–Cu–O system," *Z. Phys. B.*, vol. 64, pp. 189–193, 1986.

[24] R. J. Cava, R. B. van Dover, B. Batlogg, and E. A. Rietman, "Bulk superconductivity at 36 K in $La_{1.8}Sr_{0.2}CuO_4$," *Phys. Rev. Lett.*, vol. 58, pp. 408–410, Jan 1987.

[25] M. K. Wu, J. R. Ashburn, C. J. Torng, P. H. Hor, R. L. Meng, L. Gao, Z. J. Huang, Y. Q. Wang, and C. W. Chu, "Superconductivity at 93 K in a new mixed-phase Y-Ba-Cu-O compound system at ambient pressure," *Phys. Rev. Lett.*, vol. 58, pp. 908–910, Mar 1987.

[26] H. Maeda, Y. Tanaka, M. Fukutomi, and T. Asano, "A new high-T_c oxide superconductor without a rare earth metal," *Japanese Journal of Applied Physics*, vol. 27, pp. L209–L210, February 1988.

[27] Z. Z. Sheng and A. M. Hermann, "Bulk superconductivity at 120 K in the Tl–Ca/Ba–Cu–O system," *Nature*, vol. 332, pp. 138–139, March 1988.

[28] A. Schilling, M. Cantoni, J. D. Guo, and H. R. Ott, "Superconductivity above 130 K in the Hg–Ba–Ca–Cu–O system," *Nature*, vol. 363, pp. 56–58, May 1993.

[29] M. Tinkham, *Introduction to Superconductivity*. New York: McGraw-Hill Book Co., second ed., 1996.

[30] I. I. Rabi, J. R. Zacharias, S. Millman, and P. Kusch, "A new method of measuring nuclear magnetic moment," *Phys. Rev.*, vol. 53, no. 4, p. 318, 1938.

[31] H. Bloch, W. W. Hansen, and M. Packard, "Nuclear induction," *Phys. Rev.*, vol. 69, no. 3-4, p. 127, 1946.

[32] H. Bloch, W. W. Hansen, and M. Packard, "The nuclear induction experiment," *Phys. Rev.*, vol. 70, no. 7-8, pp. 474–485, 1946.

[33] E. M. Purcell, H. C. Torrey, and R. V. Pound, "Resonance absorption by nuclear magnetic moments in a solid," *Phys. Rev.*, vol. 69, pp. 37–38, Jan 1946.

[34] C. P. Slichter, *Principles of Magnetic Resonance*. Harper and Row, 1963.

[35] A. Abragam, *The Principles of Nuclear Magnetism*. The International Series of Monographs on Physics, Walton Street, Oxford OX2 6DP: Oxford University Press, 1961.

[36] E. Fukushima and S. B. W. Roeder, *Experimental Pulse NMR A Nuts and Bolts Approach*. Perseus Publishing, 1981.

[37] W. D. Knight, "Nuclear magnetic resonance shift in metals," *Phys. Rev.*, vol. 76, no. 8, pp. 1259–1260, 1949.

[38] H. Monien and D. Pines, "Spin excitations and pairing gaps in the superconducting state of $YBa_2Cu_3O_{7-\delta}$," *Phys. Rev. B*, vol. 41, pp. 6297–6305, Apr. 1990.

[39] H. Monien, D. Pines, and C. P. Slichter, "Spin and charge excitations in $YBa_2Cu_3O_7$: Constraints from spin-relaxation rates in the normal state," *Phys. Rev. B*, vol. 41, pp. 11120–11127, Jun 1990.

[40] E. Pardo, D. X. Chen, and A. Sanchez, "Demagnetizing factors for completely shielded rectangular prisms," *J. Appl. Phys.*, vol. 96, p. 5365, 2004.

[41] J. Korringa, "Nuclear magnetic relaxation and resonnance line shift in metals," *Physica*, vol. 16, pp. 601–610, Jul 1950.

[42] J. T. Markert, T. W. Noh, S. E. Russek, and R. M. Cotts, "NMR of ^{89}Y in normal and superconducting $YBa_2Cu_3O_{9-\delta}$," *Solid State Communications*, vol. 63, pp. 847–851, Sept. 1987.

[43] C. Recchia, J. A. Martindale, C. Pennington, W. Hults, and J. Smith, "NMR and vortex lattice melting in $YBa_2Cu_3O_7$," *Physical Review Letters*, vol. 78, pp. 3543–3546, 05 1997.

[44] Y. Xin, *Nuclear Magnetic Resonance Study of Magnetism in $NaFe_{1-x}Cu_xAs$ Single Crystals*. PhD thesis, Northwestern University, 2021.

[45] A. Bangura, "32 Tesla Superconducting Magnet (SCM-32T)," 2021.

[46] D. M. Pozar, *Microwave Engineering*. John Wiley & Sons, Inc., 4 ed., 2011.

[47] A. P. Reyes, H. N. Bachman, and W. P. Halperin, "Versatile 4 K nuclear magnetic resonance probe and cryogenic system for small-bore high-field Bitter magnets," *Review of Scientific Instruments*, vol. 68, no. 5, pp. 2132–2137, 1997.

[48] M. N. Lovellette, *Investigation of $YBa_2Cu_3O_{7-\delta}$ by NMR and construction of an ultra low temperature cryostat*. PhD thesis, Northwestern University, 1989.

[49] E. L. Hahn, "Spin echoes," *Phys. Rev.*, vol. 80, pp. 580–594, November 1950.

[50] H. Y. Carr and E. M. Purcell, "Effects of diffusion on free precession in nuclear magnetic resonance experiments," *Phys. Rev.*, vol. 94, pp. 630–638, May 1954.

[51] S. Meiboom and D. Gill, "Modified spin-echo method for measuring nuclear relaxation time," *Review of Scientific Instruments*, vol. 29, pp. 688–691, August 1958.

[52] J. H. de Boer and E. J. W. Verwey, "Semi-conductors with partially and with completely filled $_3d$-lattice bands," *Proc. Phys. Soc.*, vol. 49, pp. 59–71, 1937.

[53] N. F. Mott and R. Peierls, "Discussion of the paper by de Boer and Verwey," *Proc. Phys. Soc.*, vol. 49, pp. 72–73, 1937.

[54] C. Park and R. L. Snyder, "Structures of high-temperature cuprate superconductors," *J. Am. Ceram. Soc.*, vol. 78, no. 12, pp. 3171–3194, 1995.

[55] W. W. Warren, R. E. Walstedt, G. F. Brennert, R. J. Cava, R. Tycko, R. F. Bell, and G. Dabbagh, "Cu spin dynamics and superconducting precursor effects in planes above T_c in $YBa_2Cu_3O_{6.7}$," *Phys. Rev. Lett.*, vol. 62, pp. 1193–1196, Mar 1989.

[56] H. Alloul, T. Ohno, and P. Mendels, "^{89}Y NMR evidence for a fermi-liquid behavior in $YBa_2Cu_3O_{6+x}$," *Phys. Rev. Lett.*, vol. 63, pp. 1700–1703, Oct 1989.

[57] J. M. Harris, Z. X. Shen, P. J. White, D. S. Marshall, M. C. Schabel, J. N. Eckstein, and I. Bozovic, "Anomalous superconducting state gap size versus T_c behavior in underdoped $Bi_2Sr_2Ca_{1-x}Dy_xCu_2O_{8+\delta}$," *Phys. Rev. B*, vol. 54, pp. R15665–R15668, Dec 1996.

[58] J. A. Lee, Y. Xin, I. Stolt, W. P. Halperin, A. P. Reyes, P. L. Kuhns, and M. K. Chan, "Magnetic-field-induced vortex-lattice transition in $HgBa_2CuO_{4+\delta}$," *Phys. Rev. B*, vol. 95, p. 024512, Jan 2017.

[59] A. Yamamoto, W.-Z. Hu, and S. Tajima, "Thermoelectric power and resistivity of $HgBa_2CuO_{4+\delta}$ over a wide doping range," *Phys. Rev. B*, vol. 63, no. 2, pp. 1–6, 2000.

[60] B. X. Zhao, G. Yu, Y.-c. Cho, G. Chabot-couture, N. Barišic, P. Bourges, N. Kaneko, Y. Li, L. Lu, E. M. Motoyama, O. P. Vajk, and M. Greven, "Crystal growth and

characterization of the model high-temperature superconductor $HgBa_2CuO_{4+d}$**," *Advanced Material*, vol. 18, no. 24, pp. 3243–3247, 2006.

[61] L. E. Wright, "Oxygen isotopes," in *Encyclopedia of Geoarchaeology* (A. S. Gilbert, ed.), (Dordrecht), pp. 567–574, Springer Netherlands, 2017.

[62] A. M. Mounce, S. Oh, J. A. Lee, W. P. Halperin, A. P. Reyes, P. L. Kuhns, M. K. Chan, C. Dorow, L. Ji, D. Xia, X. Zhao, and M. Greven, "Absence of static loop-current magnetism at the apical oxygen site in $HgBa_2CuO_{4+\delta}$ from NMR," *Phys. Rev. Lett.*, vol. 111, p. 187003, Nov 2013.

[63] Q. Huang, J. W. Lynn, Q. Xiong, and C. W. Chu, "Oxygen dependence of the crystal structure of $HgBa_2CuO_{4+\delta}$ and its relation to superconductivity," *Phys. Rev. B*, vol. 52, pp. 462–470, Jul 1995.

[64] J. Jorgensen, O. Chmaissem, J. Wagner, W. Jensen, B. Dabrowski, D. Hinks, and J. Mitchell, "Effect of Re substitution on the defect structure and superconducting properties of $Hg_{1-x}Re_xBa_2Ca_{n-1}Cu_nO_{2n+2+\delta}$ (n = 2, 3, 4)," *Physica C: Superconductivity*, vol. 292, pp. 305–314, December 1997.

[65] W. W. Warren, R. E. Walstedt, G. F. Brennert, G. P. Espinosa, and J. P. Remeika, "Evidence for two pairing energies from nuclear spin-lattice relaxation in superconducting $Ba_2YCu_3O_{7-\delta}$," *Phys. Rev. Lett.*, vol. 59, pp. 1860–1863, Oct 1987.

[66] F. Mila and T. M. Rice, "Analysis of magnetic resonance experiments in $YBa_2Cu_3O_7$," *Physica C*, vol. 157, pp. 561–570, 1989.

[67] H. Alloul, P. Mendels, G. Collin, and P. Monod, "^{89}Y," *Phys. Rev. Lett.*, vol. 61, pp. 746–749, Aug 1988.

[68] B. S. Shastry, "$t - J$ model and nuclear magnetic relaxation in high-T_c materials," *Physical Review Letters*, vol. 63, pp. 1288–1291, September 1989.

[69] F. C. Zhang and T. M. Rice, "Effective hamiltonian for the superconducting cu oxides," *Phys. Rev. B*, vol. 37, pp. 3759–3761, Mar 1988.

[70] J. Haase, D. Rybicki, C. P. Slichter, M. Greven, Y. L. G. Yu, and X. Zhao, "Two-component uniform spin susceptibility of superconductor $HgBa_2CuO_{4+\delta}$ single crystals measured using ^{63}Cu and ^{199}Hg nuclear magnetic resonance," *Phys. Rev. B.*, vol. 85, no. 10, p. 104517, 2012.

[71] F. Mila and T. M. Rice, "Spin dynamics of $YBa_2Cu_3O_{6+x}$ as revealed by NMR," *Phys. Rev. B*, vol. 40, no. 16, pp. 11382–11385, 1989.

[72] A. Uldry and P. F. Meier, "Analysis of NMR spin-lattice relaxation rates in cuprates," *Phys. Rev. B*, vol. 72, p. 094508, Sep 2005.

[73] J. A. Martindale, S. E. Barrett, C. A. Klug, K. E. O'Hara, S. M. DeSoto, C. P. Slichter, T. A. Friedmann, and D. M. Ginsberg, "Anisotropy and magnetic field dependence of the planar copper NMR spin-lattice relaxation rate in the superconducting state of $YBa_2Cu_3O_7$," *Phys. Rev. Lett.*, vol. 68, pp. 702–705, 02 1992.

[74] J. A. Martindal, S. E. Barrett, C. A. Klug, K. E. O'Hara, S. M. DeSoto, C. P. Slichter, T. A. Friedmann, and D. M. Ginsbereg, "NMR in the superconducting state of $YBa_2Cu_3O_7$," *Physica C*, pp. 93–97, 1991.

[75] J. A. Martindale, S. E. Barrett, K. E. O'Hara, C. P. Slichter, W. C. Lee, and D. M. Ginsberg, "Magnetic-field dependence of planar copper and oxygen spin-lattice relaxation rates in the superconducting state of $YBa_2Cu_3O_7$," *Phys. Rev. B*, vol. 47, pp. 9155–9157, 03 1993.

[76] N. Bulut and D. J. Scalapino, "Weak-coupling model of spin fluctuations in the superconducting state of the layered cuprates," *Phys. Rev. B*, vol. 45, pp. 2371–2384, Feb 1992.

[77] D. Thelen, D. Pines, and J. P. Lu, "Evidence for $d_{x^2-y^2}$ pairing from nuclear-magnetic-resonance experiments in the superconducting state of $YBa_2Cu_3O_7$," *Phys. Rev. B*, vol. 47, pp. 9151–9154, Apr 1993.

[78] H. Bachman, A. Reyes, W. Halperin, J. Martindale, and P. Hammel, "Anomalous planar ^{17}O spin-spin relaxation in the superconducting state of $YBa_2Cu_3O_7$," *Bull Am. Phys. Soc.*, vol. 41, no. 467, 1996.

[79] C. Gros, R. Joynt, and T. Rice, "Superconducting instability in the large-u limit of the two-dimensional hubbard model," *Z. Phys. B*, vol. 68, pp. 425–432, 1987.

[80] L. Onsager, "Statistical hydrodynamics," *Nuovo Cim*, vol. 6, pp. 279–287, 1949.

[81] R. P. Feynman, "Chapter II Application of Quantum Mechanics to Liquid Helium," in *Progress in Low Temperature Physics* (C. J. Gorter, ed.), vol. 1, pp. 17 – 53, Elsevier, 1955.

[82] U. Essmann and H. Träuble, "The direct observation of individual flux lines in type II superconductors," *Phys. Lett.*, vol. 24A, no. 10, pp. 526–527, 1967.

[83] G. Karapetrov, J. Fedor, M. Iavarone, D. Rosenmann, and W. Kwok, "Direct observation of vortex lattice transitions in mesoscopic superconducting single crystals using STM," *Physica C: Superconductivity and its Applications*, vol. 437-438, pp. 127–131, 2006. Proceedings of the Fourth International Conference on Vortex Matter in Nanostructured Superconductors VORTEX IV.

[84] E. H. Brandt, "Precision Ginzburg-Landau Solution of Ideal Vortex Lattices for any Induction and Symmetry," *Phys. Rev. Lett.*, vol. 78, no. 11, pp. 2208–2211, 1997.

[85] D. Ihle, "Wigner-seitz approximation for the description of the mixed state of type II superconductors," *Phys. Stat. Sol. B*, vol. 47, pp. 423–429, 1971.

[86] J. R. Clem, "Simple model for the vortex core in a type II superconductor," *J. Low Temp. Phys.*, vol. 18, pp. 427–434, 1975.

[87] Z. Hao, J. R. Clem, M. W. McElfresh, L. Civale, A. P. Malozemoff, and F. Holtzberg, "Model for the reversible magnetization of high-κ type-II superconductors: Application to high-T_c superconductors," *Phys. Rev. B*, vol. 43, pp. 2844–2852, Feb 1991.

[88] E. H. Brandt, "Ginsburg-Landau Theory of the Vortex Lattice in Type-II Superconductors for all values of κ and B," *Phys. Sta. Sol. B*, vol. 51, pp. 345–358, 1972.

[89] G. E. Volovik, "Superconductivity with lines of gap nodes: density of states in the vortex," *Pis'ma Zh. Eksp. Teor. Fiz.*, vol. 58, pp. 457–461, September 1993.

[90] N. B. Kopnin and G. E. Volovik, "Singularity of the vortex density of states in d-wave superconductors," *Jetp Lett.*, vol. 64, pp. 690–694, 1996.

[91] S. H. Simon and P. A. Lee, "Scaling of the quasiparticle spectrum for d-wave superconductors," *Phys. Rev. Lett.*, vol. 78, pp. 1548–1551, Feb 1997.

[92] K. A. Moler, D. J. Baar, J. S. Urbach, R. Liang, W. N. Hardy, and A. Kapitulnik, "Magnetic field dependence of the density of states of $YBa_2Cu_3O_{6.95}$ as determined from the specific heat," *Phys. Rev. Lett.*, vol. 73, pp. 2744–2747, Nov 1994.

[93] K. A. Moler, D. L. Sisson, J. S. Urbach, M. R. Beasley, A. Kapitulnik, D. J. Baar, R. Liang, and W. N. Hardy, "Specific heat of $YBa_2Cu_3O_{7-\delta}$," *Phys. Rev. B*, vol. 55, pp. 3954–3965, Feb 1997.

[94] B. Revaz, J.-Y. Genoud, A. Junod, K. Neumaier, A. Erb, and E. Walker, "$d-$Wave scaling relations in the mixed-state specific heat of $YBa_2Cu_3O_7$," *Phys. Rev. Lett.*, vol. 80, pp. 3364–3367, Apr 1998.

[95] E. H. Brandt, "Magnetic flux density of perfect and imperfect flux line lattices in type II superconductors," *Journal of Low Temperature Physics*, vol. 73, p. 355, 1988.

[96] J. E. Hoffman, E. W. Hudson, K. M. Lang, V. Madhavan, H. Eisaki, S. Uchida, and J. C. Davis, "A four unit cell periodic pattern of quasi-particle states surrounding vortex cores in $Bi_2Sr_2CaCu_2O_{8+\delta}$," *Science*, vol. 295, pp. 466–469, 2002.

[97] T. Hanaguri, C. Lupien, Y. Kohsaka, D. H. Lee, M. Azuma, M. Takano, H. Takagi, and J. C. Davis, "a 'checkerboard' electronic crystal state in lightly hole-doped $Ca_{2-x}Na_xCuO_2Cl_2$," *Nature*, vol. 430, pp. 1001–1005, 2004.

[98] W. D. Wise, M. C. Boyer, K. Chatterjee, T. Kondo, T. Takeuchi, H. Ikuta, Y. Wang, and E. W. Hudson, "Charge-density-wave origin of cuprate checkerboard visualized by scanning tunnelling microscopy," *Nat. Phys.*, vol. 4, pp. 696–699, 2008.

[99] D. I. Khomskii and A. Freimuth, "Charged vortices in high temperature superconductors," *Phys. Rev. Lett.*, vol. 75, pp. 1384–1386, 1995.

[100] G. Blatter, M. Feigel'man, V. Geshkenbein, A. Larkin, and A. van Otterlo, "Electrostatics of vortices in type-II superconductors," *Phys. Rev. Lett.*, vol. 77, pp. 566–569, 1996.

[101] J. R. Clem, "Two-dimensional vortices in a stack of thin superconducting films: A model for high-temperature superconducting multilayers," *Phys. Rev. B*, vol. 43, pp. 7837–7846, Apr 1991.

[102] N. Barišić, Y. Li, X. Zhao, Y.-C. Cho, G. Chabot-Couture, G. Yu, and M. Greven, "Demonstrating the model nature of the high-temperature superconductor $HgBa_2CuO_{4+\delta}$," *Phys. Rev. B*, vol. 78, p. 054518, Aug 2008.

[103] Y. Li, N. Egetenmeyer, J. L. Gavilano, N. Barišić, and M. Greven, "Magnetic vortex lattice in $HgBa_2Cu_2O_{4+\delta}$ observed by small-angle neutron scattering," *Physical Review B*, vol. 83, p. 054507, 2011.

[104] S. P. Brown, D. Charalambous, E. C. Jones, E. M. Forgan, P. G. Kealey, A. Erb, and J. Kohlbrecher, "Triangular to square flux lattice phase transition in $YBa_2Cu_3O_7$," *Phys. Rev. Lett.*, vol. 92, p. 067004, Feb 2004.

[105] J. S. White, V. Hinkov, R. W. Heslop, R. J. Lycett, E. M. Forgan, C. Bowell, S. Strässle, A. B. Abrahamsen, M. Laver, C. D. Dewhurst, J. Kohlbrecher, J. L. Gavilano, J. Mesot, B. Keimer, and A. Erb, "Fermi surface and order parameter driven vortex lattice structure transitions in twin-free $YBa_2Cu_3O_7$," *Phys. Rev. Lett.*, vol. 102, p. 097001, Mar 2009.

[106] R. Cubitt, E. M. Forgan, G. Yang, S. L. Lee, D. M. Paul, H. A. Mook, M. Yethiraj, P. H. Kes, T. W. Li, A. A. Menovsky, Z. Tarnawski, and K. Mortensen, "Direct observation of magnetic flux lattice melting and decomposition in the high-T_c superconductor $Bi_{2.15}Sr_{1.95}CaCu_2O_{8+x}$," *Nature*, vol. 365, pp. 407–411, September 1993.

[107] G. Villard, A. Daignere, D. Pelloquin, and A. Maignan, "Effect of underdoping on the superconductivity of $(Hg,Cu)Ba_2CuO_{4+\delta}$ '1201' single crystals," *Physica C: Superconductivity*, vol. 314, no. 3, pp. 196–204, 1999.

[108] E. H. Brandt, "Thermal fluctuation and melting of the vortex lattice in oxide superconductors," *Phys. Rev. Lett.*, vol. 63, pp. 1106–1109, Sep 1989.

[109] V. Vinokur, B. Khaykovich, E. Zeldov, M. Konczykowski, R. Doyle, and P. Kes, "Lindemann criterion and vortex-matter phase transitions in high-temperature superconductors," *Physica C: Superconductivity*, vol. 295, no. 3, pp. 209–217, 1998.

[110] D. I. Khomskii and F. V. Kusmartsev, "Charge redistribution and properties of high-temperature superconductors," *Phys. Rev. B*, vol. 46, pp. 14245–14248, Dec 1992.

[111] S. J. Hagen, A. W. Smith, M. Rajeswari, J. L. Peng, Z. Y. Li, R. L. Greene, S. N. Mao, X. X. Xi, S. Bhattacharya, Q. Li, and C. J. Lobb, "Anomalous flux-flow hall effect: $Nd_{1.85}Ce_{0.15}CuO_{4-y}$ and evidence for vortex dynamics," *Phys. Rev. B*, vol. 47, pp. 1064–1068, Jan 1993.

[112] A. van Otterlo, M. Feigel'man, V. Geshkenbein, and G. Blatter, "Vortex dynamics and the hall anomaly: A microscopic analysis," *Phys. Rev. Lett.*, vol. 75, pp. 3736–3739, Nov 1995.

[113] Y. Chen, Z. D. Wang, J.-X. Zhu, and C. S. Ting, "Vortex charges in high-temperature superconductors," *Phys. Rev. Lett.*, vol. 89, p. 217001, Nov 2002.

[114] D. Knapp, C. Kallin, A. Ghosal, and S. Mansour, "Antiferromagnetism and charged vortices in high-T_c superconductors," *Phys. Rev. B*, vol. 71, p. 064504, 2005.

[115] H.-W. Zhao, G.-Q. Zha, S.-P. Zhou, and F. M. Peeters, "Long-range Coulomb repulsion effect on a charged vortex in high-temperature superconductors with competing d-wave and antiferromagnetic orders," *Phys. Rev. B.*, vol. 78, p. 064505, 2008.

[116] K.-i. Kumagai, K. Nozaki, and Y. Matsuda, "Charged vortices in high-temperature superconductors probed by NMR," *Phys. Rev. B*, vol. 63, p. 144502, Mar 2001.

[117] A. G. Redfield, "On the theory of relaxation processes," *IBM Journal of Research and Development*, vol. 1, no. 1, pp. 19–31, 1957.

[118] R. K. Wangsness and F. Bloch, "The dynamical theory of nuclear induction," *Phys. Rev.*, vol. 89, pp. 728–739, Feb 1953.

[119] F. Bloch, "Dynamical theory of nuclear induction. II," *Phys. Rev.*, vol. 102, pp. 104–135, Apr 1956.

[120] N. Bloembergen, E. M. Purcell, and R. V. Pound, "Relaxation effects in nuclear magnetic resonance absorption," *Phys. Rev.*, vol. 73, pp. 679–712, Apr 1948.